ATMOSPHERIC DYNAMICS
IN A
MODEL RR LYRAE STAR

Thesis by

John Irvin Castor

In Partial Fulfillment of the Requirements

For the Degree of

Doctor of Philosophy

California Institute of Technology

Pasadena, California

1967

(Submitted August 12, 1966)

What a man knows not, that he doth require,
And what he knoweth, that he cannot use.

--Goethe, "Faust"

Preface

I can only mention some of the people to whom I am indebted. Professor Robert F. Christy, besides doing the research which inspired my work, has been of constant help and encouragement for the past two and one half years. I am especially grateful for being allowed free use of his computational results. My advisor, Professor J. Beverly Oke, introduced me to Professor Christy's work, and in the last several years has made the observations of RR Lyrae stars which make these models astronomically relevant. He has provided me the indispensable service of an advisor: administrative sustenance and protection. I would like to thank Professor Jesse L. Greenstein for allowing me liberal use of computing time.

I have had helpful conversations at times with Drs. Robert F. Kraft and Allan R. Sandage, not to mention one or two delightful dinners. Dr. Dimitri Mihalas taught me much about stellar atmospheres and I would like to thank him for permission to use his program. Dr. Barry M. Lasker gave some very helpful advice regarding ionization fronts.

Many persons in the astronomy department at Caltech have been helpful to me, through many conversations on and off astronomy. I think of Neil Divine, Subhash Chandra, Fritz Bartlett, and Chris Anderson among these. I am grateful to

Maggie Hayden for her rapid and expert typing.

A person from whom I learned much regarding astronomy, World War II, and cars, who explained the peculiarities of Caltech to me when I first arrived, and who performed the extremely valuable and somewhat immense task of translating into Fortran IV and documenting the Mihalas program, was Butch Lungershausen.

I want to express my thanks to The University of Chicago Press for permission to reproduce Figure 19. During my graduate work I was the recipient of a National Science Foundation Graduate Fellowship and of a Caltech Graduate Research Assistantship, for which I am very thankful.

Abstract

A dynamical model of an RR Lyrae star has been constructed which is similar to those of Christy (1) in its treatment of the envelope interior to the hydrogen ionization zone but which describes the hydrogen ionization zone and the outer atmosphere in some detail. In the optically thin region heat transfer is described with the gray equation of radiation transfer which yields an integral expression for the heating rate, assuming small deviations from sphericity.

The model which has been constructed has the parameters:

$$M_{bol} = .76, \quad T_e = 6500°K, \mathcal{M} = .58\mathcal{M}_\odot, \quad Y = .30.$$

The model results of Christy for the same parameters have been used as initial conditions.

The results have indicated a close connection between the complex hydrogen ionization zone dynamics and the observable phenomena in the star, such as rising branch shocks and the shape of the velocity curve during the decreasing light phase.

The work done by the hydrogen ionization zone to maintain pulsation has been found in this calculation to be in excellent agreement with the figure obtained by

Christy for this star.

Deviations from radiative equilibrium in the optically thin layers have been found to be confined to tau less than 0.1 and to high gravity, low temperature phases, when they may exceed 500° K.

Model atmospheres have been constructed with the dynamical pressure and temperature distributions using Mihalas' program (2). The emergent continuum fluxes obtained show considerable similarity to observed monochromatic light variation, although the amplitudes are greater and the rise time is less than is observed. The errors in temperature determinations based on fitting equilibrium models to the continuum have been found to be of the same order as fluctuations which appear in observational determinations of the radius variation.

It has been concluded that the differences between the model and the observed stars may be due in part to the omission of convection from the model, since it may become quite important during high gravity phases.

---

(1) Christy, R. F. 1966, Ap. J. 144, 108.

(2) Mihalas, D. M. 1963, Thesis, California Institute of Technology.

Table of Contents

Table of Contents, Continued

Introduction

The study of pulsating stars is, along with the explanation of the Hertzsprung-Russell diagram, one of the major problems of theoretical astrophysics. In fact, the development of these two subjects has been quite parallel. Perhaps initially pulsation theory evolved more rapidly; in Eddington's classic Internal Constitution (1930) the chapter on variable stars contains more that is accurate in the light of present knowledge than the chapters on other aspects of stellar structure. The linear-adiabatic theory which had been developed by that time would have been adequate to yield considerable information about the periods and distributions of amplitude in the stars if realistic interior models had been available.

The following twenty years saw considerable improvement in stellar models as accurate knowledge of nuclear energy sources and radiative opacity was applied. In pulsation theory there were investigations of stability by the quasi-adiabatic method, outlined by Eddington (1930, Sec. 134), as reviewed by Rosseland (1949, Sec. 5.2, 5.6-5.8), and some discussion of non-linear pulsation (Rosseland 1949, Chapt. 7). These were not notable successes; the stability calculations were unable to find instability for

appropriate models and the non-linear studies had very limited success in explaining the observed light and velocity variations.

In the 1950's the theory of stellar evolution developed enormously, due largely to the wholesale use of numerical methods in solving the equations of stellar structure, leading finally to the approach of Henyey (Henyey et al 1959). The first use of a realistic giant model to represent a pulsating star was by Epstein (1950) and indicated the irrelevance of the core and the consequent importance of the outer envelope in stellar pulsation. Cox (1955) used the quasi-adiabatic analysis on Epstein's model and found a very short damping time in contrast with previous work, due to the great surface concentration of the amplitude in the giant star. However, the most significant result in the decade was the discovery by Zhevakin (1953), following Eddington's suggestion (1930, sec. 137), that a variable heat leak, caused in this case by the HeII ionization zone, could cause pulsational instability.

Subsequent research in this subject has reflected the application of detailed numerical methods employing high-speed computers. Much recent effort has been directed with these means toward predicting the instability region in the HR diagram (Baker and Kippenhahn 1962, also Cox 1963,

later Baker and Kippenhahn 1965) using a linear non-adiabatic treatment, and with considerable success. In the last-mentioned study various models were chosen from an evolutionary track which had been computed from the main-sequence into the Cepheid region and for each of these the linearized structure equations were solved to determine all the pulsation properties including the period and the growth rate of the pulsation.

That work probably represents the ultimate of what can be done in Cepheid pulsation with a linear theory. It has become clear that any realistic treatment of the hydrogen ionization zone and the region above, the only observable part of the star, must be non-linear. This means that the only feasible way to approach the problem is with direct numerical integration in time. Recently results deriving from this approach have been published by Cox et al (1966) and by King, Cox, and Eilers (1966) for various models of Cepheid variables. These models confirm the results of Baker and Kippenhahn (1965), except in the hydrogen ionization zone and above where the former are probably superior. Unfortunately the large radius used for the inner boundary in the computation (at 80 percent) and the lack of detail in the atmosphere prevented obtaining correct periods and realistic surface variations of luminosity and velocity.

These defects are less in the work of Christy (1964, 1966a; see also 1966b) on RR Lyrae stars. These RR Lyrae models are notably successful both in explaining the dependence of instability on stellar parameters and in predicting the observable properties of pulsation.

It was my objective in the project I will report below to improve as much as I could the realization of this second point. A survey to study instability necessarily represents a compromise between volume of calculation and the accuracy of the atmospheric description. In Christy's models the coarseness of the mass division had two effects: It imposed the same coarse structure on the luminosity and (sometimes) velocity variations. It also considerably altered some phenomena associated with the hydrogen ionization zone which are of an essentially small-scale nature.

Therefore my procedure differed from Christy's in these respects: The division of the stellar mass into shells for the computation was done in such a way that the temperature, density, and velocity distributions were everywhere accurately represented, and therefore the surface luminosity and velocity curves were relatively accurate. This necessitated having several mass shells concentrated in the hydrogen ionization region. The other principal difference was the use of a radiative energy

transfer formula obtained directly from the equation of transfer rather than the photon-diffusion formula. The reason for this was the desire to properly represent all the non-equilibrium effects on the pulsating atmosphere. The use of the diffusion equation accelerates the relaxation to equilibrium of an optically thin layer of thickness $\Delta\tau$ by a factor $(1/\Delta\tau)^2$, and so is unacceptable for a proper dynamical description of the small optical depth region.

My specific goal was to construct a relaxed model with this kind of atmospheric detail for a typical RR Lyrae star. The atmospheric structure given by the model could then be used to infer observable atmospheric properties; the most useful of these is the spectral energy distribution. The comparison between the calculated observable quantities and the observations of RR Lyrae stars hopefully would reveal certain features in common. With the dynamical model in hand, these features could be traced to the physical processes responsible for them: something very difficult to do with the observations alone. The systematic behavior of these processes might later be used as a measuring stick for the stars.

I would like to digress briefly at this point on the subject of the method of analysis employed in

this study as well as in those of Cox et al and Christy. The general concept can be called "numerical experimentation" and is an outgrowth of the application of computers to theoretical problems. An excellent reference on this subject is the Slaught Memorial Paper "Computers and Computing" (Heller et al 1965), especially the article on numerical fluid dynamics by Harlow (p. 84).

The basis of the method is the establishment within the computer of an arithmetic analogy to the physical object it is desired to study, using the mathematical description of the object supplied by physical analysis to replace physical quantities with digitally coded numbers and to replace the physical interactions with arithmetic processing. Beginning with values of the stored quantities which might represent the initial conditions of an experiment on the object the computer is used to follow the history of the object by finding successive states of the numerical analogue. Periodically the values of some of the quantities are transmitted to the output device ("measurements"). By analyzing these numbers the theoretician can learn whatever he might learn if it were possible for him to do the corresponding real experiment. And that, of course, is either something or nothing, depending on his interpretive skill and the appropriateness of the experiment.

One example of the usefulness of this method is

the analysis of the formation of lunar craters: What is the effect of a one kilometer sphere of rock striking a plain at fifty kilometers per second? The relation between the diameter of the resulting crater, the mass of the meteorite, and the physical properties of the rock is probably unobtainable in any other way. As another example I might cite the calculation of the light-amplitude to velocity-amplitude ratio of a variable star and its dependence on stellar properties.

The use of numerical experimentation becomes necessary when to begin with the observational data are so indirectly related to the information it is desired to obtain that first a complete model must be constructed and then matched against the observations. This necessity is familiar from, for example, stellar atmospheres, where it is desired to infer the effective temperature and the gravity of a star from the observed spectral continuum properties. When dynamical rather than equilibrium phenomena are studied and non-linearity prevents Fourier analysis with respect to time, an initial value problem must be solved, and that requires a numerical experiment.

This brings me to the subject of a final remark about the model constructed in this work. The non-linear vibrations of an unstable star tend toward periodicity as the amplitude increases (limit-cycle behavior) and the

initial conditions are no longer relevant; the calculations do the same if they are performed for a sufficient length of time, leading to the relaxed model I spoke of before. Unfortunately I found myself severely limited in the number of cycles I could calculate by the large number of integration steps required. Thus it was impossible to let my own calculation relax. Instead I relied heavily for initial conditions on the excellently periodic results of Christy's calculation for the same star, which he was kind enough to supply, augmented by several more periods of his type of calculation to relax some discrepancies of mass division and state functions.

The text which follows is divided into four parts: Part I summarizes the computational procedure used in the construction of the final model. Part II contains the results which are of an essentially physical nature; Part III is devoted to the observationally-directed results, and is mostly concerned with the model atmosphere description. Part IV discusses the model deficiencies and convection, which seems to be a missing ingredient of considerable importance for understanding several problems. Finally there is a review of what I feel are the principal conclusions which can be drawn from this work.

Part I. Calculation Procedure

A numerical experiment requires starting with a mathematical formulation of the problem, a system of equations which suffices to determine completely the physical situation to the extent that one is interested in knowing it, subject to the initial and boundary conditions which are the major premise in the physical question that is asked. These equations are presumably capable of describing the phenomena which are being looked for in performing the "experiment".

In the present instance what is desired from the model is a simulation of a pulsating RR Lyrae star envelope and atmosphere. What is not required is any description involving rotation, magnetic fields, turbulence (as it modifies the hydrodynamics), viscosity, non-LTE, or other such complications which may play a role, but not a dominant one in the envelope and atmosphere. In addition, since the interiors of these stars are inert in the pulsation, it is unnecessary to describe any of the region where the temperature exceeds 10^6 degrees. We will describe, then, a spherically symmetrical envelope in which the only forces on the material are due to gravity, gas pressure and radiation pressure, and the energy balance in the material is established by the energy flux which derives

from radiation transfer, and, conceivably, convection. The lagrangian coordinate system is used, so that the spatial variable is M_r. The equation of motion and energy equation then are (Christy 1964):

$$\frac{\partial u}{\partial t} = -\frac{GM_r}{r^2} - 4\pi r^2 \frac{\partial p}{\partial M_r}$$

$$\frac{\partial r}{\partial t} = u$$

$$T\frac{\partial \mathcal{S}}{\partial t} = \frac{\partial E}{\partial t} + p\frac{\partial V}{\partial t} = -\frac{\partial L_r}{\partial M_r}$$

All the symbols are defined in Appendix A. The thermodynamic functions p and $\mathcal{S}$ are known in terms of T and V. L_r is found from the structure by means of whatever theory of radiative transfer is invoked, and conceivably convective transfer.

The construction of the model is an initial value problem. The state of the star is specified at time $t = 0$ and the foregoing equations are used to find numerically the evolution of the star with time. The assumption of this procedure is that sufficient calculation can be done to yield a solution which is essentially periodic in time. In practice how well this is realized with a given amount of computation depends on the care with which the initial conditions are chosen. How this was done for the present model will be discussed later.

The boundary conditions which are required to complete this system of equations must prescribe the motion

of, and energy transfer across, the inner and outer boundary. At the inner boundary the assumption is

$$r = \text{constant}$$

$$L_r = L_o = \text{constant} .$$

At the outer boundary the energy flux follows from the theory of radiative transfer being used while the motion of the outer boundary depends on an assumption regarding what type of wave motion can exist.

The division of the stellar mass into finite units is done as follows. The star is partitioned by approximately 50 concentric "spheres" into that many spherical "shells". The material within each shell is considered thermodynamically homogeneous. The shells and spheres are indexed as shown in Figure 1. The "intrinsic" variables T, V, p, χ, δ, $\frac{\partial L}{\partial M}$ etc. are defined in the "shells", while the "extrinsic" variables R, U, MO, Ml, TAU 1 are defined on the "spheres". Notice that sphere N is the <u>inside</u> boundary of shell N. Concerning the mass coordinates, MO is the usual M_r of stellar interiors, Ml is ln(MT-MO), and both are defined on the spheres. However, M is the natural logarithm of MT minus MO at the midpoint (in mass) of each shell, so

$$M(I) = \ln\left(\tfrac{1}{2}\left(e^{M1(I)} + e^{M1(I+1)}\right)\right).$$

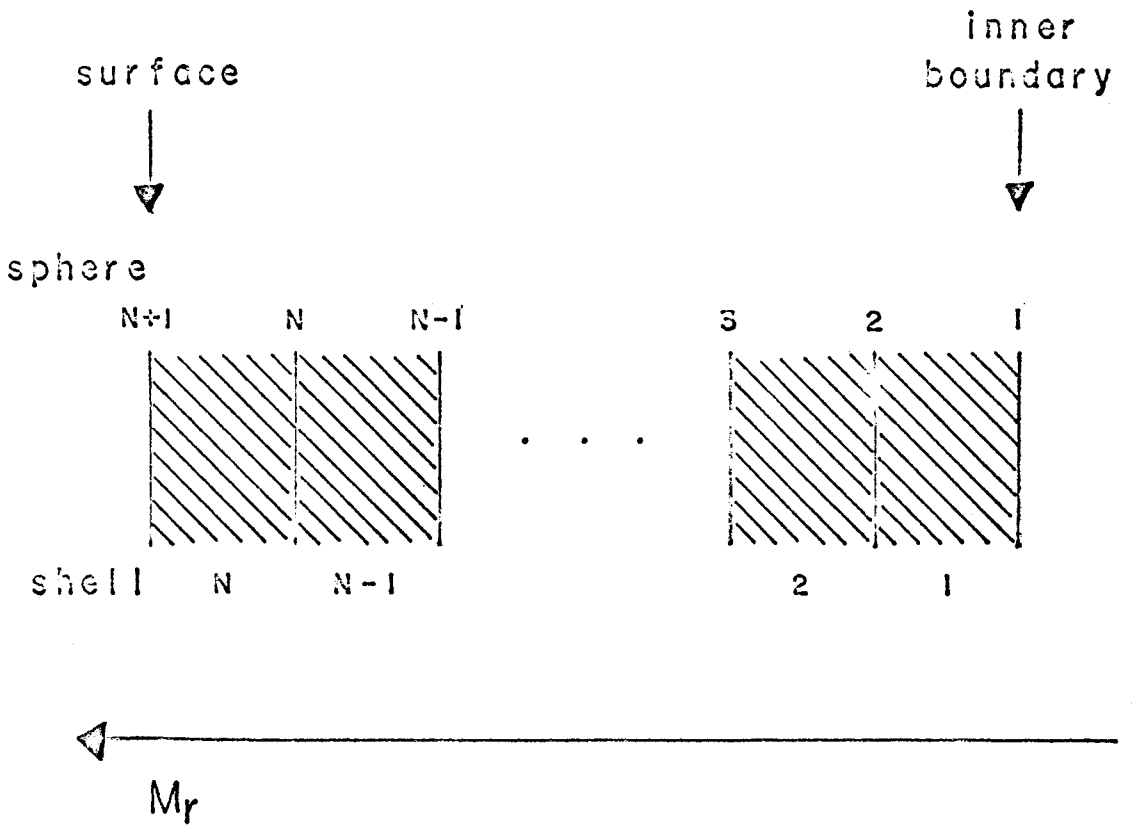

Figure 1. Division of the star into spherical shells and the indexing system

M1 is significant since the spheres are evenly spaced with respect to it, except in the H zone and the deep envelope. The mass elements DM1, the mass of each shell, and DM2, the inertia of each sphere, are given by

$$DM1(I) = e^{M1(I)} - e^{M1(I+1)}, \quad DM2(I) = e^{M(I-1)} - e^{M(I)}.$$

The value of M1 on the surface sphere #N+1 is derived by the following argument: pressure is proportional to the outside mass, and if it is desired that the pressure by in a geometric progression (which keeps the sound travel time across the shells fairly constant), that may be assured if M1(N+1) follows from DM1(N) as it would in an infinite progression: if DLGDM1 is the constant increment in M1 then

$$e^{M1(N+1)} = DM1(N)/(e^{DLGDM1} - 1).$$

In order to minimize the second order truncation errors due to the finite time step the location of the various variables in time is staggered according to their function in the equations. The intrinsic variables p_i, V_i etc. are located at times t_n, and by inference so are the extrinsic variables R_i and L_i since these depend only on the intrinsic variables and not on time derivatives. But time derivatives of these quantities are located at the midpoints of the time intervals,

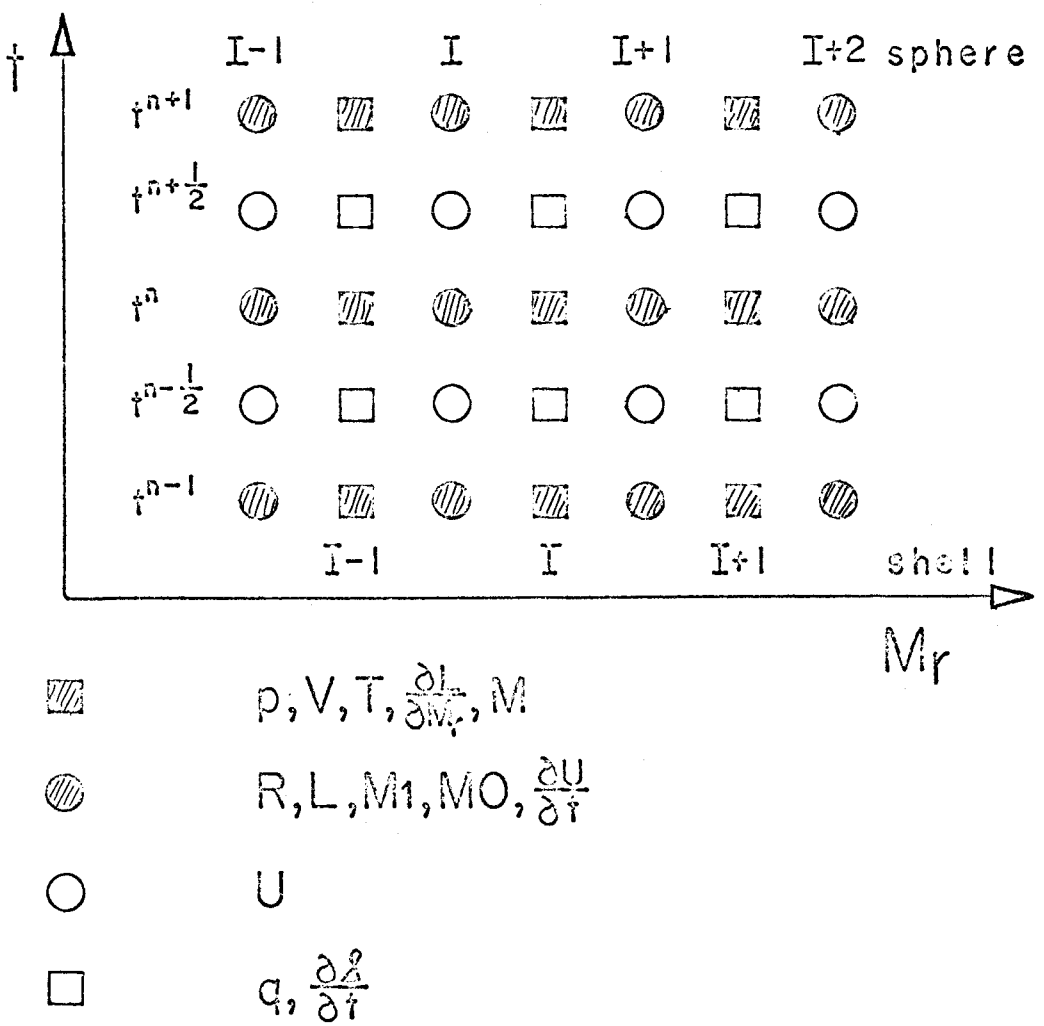

Figure 2. Location of the variable in mass and time

at $t_{n+1/2} = 1/2(t_n+t_{n+1})$; variables of this type are $U_i = \partial R_i/\partial t$ and $\partial \mathcal{L} i/\partial t$. The latter variable must therefore be given as a mean of its values at t_n and t_{n+1}. Finally $\partial U_i/\partial t$ is again located at t_n. This is diagrammed in Figure 2.

Because of the ability of the hydrodynamical equations to yield shocks they require some modification in forming finite-difference analogues. If no modification is made it is found that when a shock would have occurred in the continuous fluid the mass shells may cross over each other in the finite-difference representation and computation becomes impossible. To prevent this, an extra repulsive force between rapidly approaching spheres is added to the normal pressure force. This is supplied by a pseudo-viscous pressure q_i^n:

$$q_i^n = \frac{C_Q}{V_i^n}\left(\max\left(0, u_i^{n-\frac{1}{2}} - u_{i+1}^{n-\frac{1}{2}}\right)\right)^2$$

added to p_i^n. The fact that q_i^n is not properly centered in time is probably not significant since q is much less than p under virtually all circumstances.

The actual difference equations for the dynamics, equivalent to those used by Christy (1964 etc.), are :

$$\left.\begin{aligned} U_i^{n+\frac{1}{2}} - U_i^{n-\frac{1}{2}} &= Dt_n \left(-\frac{GMO_i}{(R_i^n)^2} - \frac{4\pi (R_i^n)^2}{DM2_i} \left(p_i^n + q_i^n - p_{i-1}^n - q_{i-1}^n \right) \right) \\ R_i^{n+1} - R_i^n &= Dt_{n+\frac{1}{2}} U_i^{n+\frac{1}{2}} \end{aligned} \right\} i = 2, N+1$$

$$V_i^n = \frac{3}{4\pi} \frac{(R_{i+1}^n)^3 - (R_i^n)^3}{DM1_i} \qquad i = 1, N$$

where

$$Dt_n = t_{n+\frac{1}{2}} - t_{n-\frac{1}{2}} = \frac{1}{2}(t_{n+1} - t_{n-1})$$

$$Dt_{n+\frac{1}{2}} = t_{n+1} - t_n \ .$$

The interior boundary conditions are

$$U_1^{n+\frac{1}{2}} \equiv 0$$

$$R_1^n \equiv \text{constant} \ .$$

The dynamical surface boundary condition requires some thought. It is illusory to imagine that there is no mass exterior to the last sphere: in reality that condition is only realized at infinite radius, an infinite sound travel time from the body of the star. What is required is an expression for the mechanical effect of

the mass exterior to the last sphere on the interior. Two limiting cases are standing-wave conditions and running-wave conditions. In the latter the pressure is just in phase with the velocity and this condition can be used to determine the motion of the surface sphere. However as Unno (1965) has discussed, due to the small value of the scale height with respect to the radius the standing wave condition should prevail in Cepheids (and RR Lyrae stars), which can be expressed as

$$\frac{p(M_r,t)}{p_o(M_r)} \longrightarrow \text{constant} \quad \text{as} \quad p_o(M_n) \longrightarrow 0.$$

This leads to the expression for $\partial p/\partial M_r$

$$\left(\frac{\partial p}{\partial M_r}\right)^n_{N+1} = \frac{p^n_{N+1} + q^n_{N+1} - p^n_N - q^n_N}{DM2^*_{N+1}}$$

where, using the step DLGDM1 in $\ln(MT-M_r)$,

$$p^n_{N+1} + q^n_{N+1} \equiv e^{-DLGDM1}\left(p^n_N + q^n_N\right)$$

$$DM2^*_{N+1} \equiv \frac{1}{2}\left(DM1_N + e^{-DLGDM1} DM1_N\right).$$

This can also be written

$$\left(\frac{\partial p}{\partial M_r}\right)^n_{N+1} = \frac{p^n_{N+1} + q^n_{N+1} - p^n_N - q^n_N}{DM2_{N+1}}$$

with

$$p^n_{N+1} + q^n_{N+1} \equiv 0$$

$$DM2_{N+1} \equiv DM1_N \cdot \frac{1}{2} \frac{1+e^{-DLGDM1}}{1-e^{-DLGDM1}} .$$

The latter form will be used, since it is more convenient to have p+q vanish at the surface.

This type of difference treatment has disadvantages, as will be seen shortly, but it has a great advantage: the existence of a conserved energy-sum. Replacing the temporal difference quotients by derivatives again in the $\partial U_i/\partial T$ expression, multiplying by $U_i DM2_i$, substituting $\partial R_i/\partial t$, and summing gives

$$\frac{\partial}{\partial t}\sum DM2_i \frac{u_i^2}{2} = \frac{\partial}{\partial t}\sum \frac{G \cdot MO_i}{R_i} DM2_i - \sum 4\pi R_i^2 u_i (p_i + q_i)$$

$$+ \sum 4\pi R_i^2 u_i (p_{i-1} + q_{i-1})$$

or

$$\frac{\partial}{\partial t}\sum DM2_i \left(\frac{u_i^2}{2} - \frac{G \cdot MO_i}{R_i} \right) = \sum (p_i + q_i) \frac{\partial}{\partial t} \frac{4\pi}{3} \left(R_{i+1}^3 - R_i^3 \right)$$

$$= \sum DM1_i (p_i + q_i) \frac{\partial V_i}{\partial t} ,$$

where use has been made of the identities $p_{N+1}+q_{N+1} = 0$ and $U_1 = 0$ and of the equation for V_i. This equation expresses conservation of mechanical energy for the discrete system. When finite time differences are used errors of order $(\Delta t)^2$ may be expected in the energy balance, but no errors related to the mass division. This expression also yields the proper definition of kinetic energy:

$$KE = \sum DM2_i \frac{u_i^2}{2} .$$

If, in the pseudo-viscosity expression, C_Q is approximately 1 then $p_i^n+q_i^n$ deviates from p_i^n only when

$$u_i^{n-\frac{1}{2}} - u_{i+1}^{n-\frac{1}{2}} \geq (C_s)_i$$

where C_s is the sound speed. This is the condition for a shock to exist. If this is the case, it is found that the shock thickness as represented in the results is about $2\sqrt{C_Q}$ mass spheres.

The condition for stability of this difference system (ignoring for the time being the heat equation) is:

$$\frac{4\pi R_i^2 \rho_i CS_i \cdot Dt}{DM1_i} < \mathcal{E} , \qquad i = 1, N$$

where CS_i is the sound speed in shell i. $\mathcal{E}$ is 1 if shocks can be neglected, but is less if shocks are important; and in that case depends on C_Q: if C_Q is increased $\mathcal{E}$ must be decreased to retain stability. The values used in the present calculations were $C_Q = 1/2$ and $\mathcal{E} = 1/2$. Because of the thinness of the shells in the hydrogen ionization zone this condition on Dt is quite severe. It necessitated using much smaller time steps for the dynamics than for the heat equation, so that the heat equation was integrated only every 10 dynamic integration steps typically. Therefore, T_i^n was not always defined; generally the last T_i defined was, say, $T_i^n 1$. What was done in that case was to use the following expression for p_i^n :

$$\log p_i^n = \log p(T_i^{n'}, V_i^{n'}) + \left(\left(\frac{\partial \log p}{\partial \log V}\right)_S\right)_i^{n'} \left(\log V_i^n - \log V_i^{n'}\right),$$

in other words, the pressure was assumed to vary adiabatically between heat equation steps. This is an excellent approximation in the deep interior, but less so in the outer envelope; in any case the effect of this approximation on the energy integral is estimated not to be more serious than the $0(\Delta t^2)$ terms.

The differential equation of energy conservation is

$$T_i \frac{\partial s_i}{\partial t} = \frac{\partial E_i}{\partial t} + p_i \frac{\partial V_i}{\partial t} = -\left(\frac{\partial L}{\partial M}\right)_i .$$

When p_i is replaced by $p(T_i^n, V_i^n) + q_i^n$, then this equation must be modified to give

$$T_i \frac{\partial s_i}{\partial t} = \frac{\partial E_i}{\partial t} + p_i \frac{\partial V_i}{\partial t} = -\left(\frac{\partial L}{\partial M}\right)_i - q_i \frac{\partial V_i}{\partial t} .$$

accounting for the work done by the pseudo-viscous pressure. The difference equation using the mean of the advanced and the retarded time derivatives is then

$$\left(T_i^{n_1} + T_i^{n_2}\right)\left(s_i^{n_2} - s_i^{n_1}\right) = -\left(t_{n_2} - t_{n_1}\right)\left(\left(\frac{\partial L}{\partial M}\right)_i^{n_1} + \left(\frac{\partial L}{\partial M}\right)_i^{n_2}\right) - 2\int_{t_{n_1}}^{t_{n_2}} q_i \, dV_i .$$

The integral appearing in this expression is evaluated as

$$\int_{t_{n_1}}^{t_{n_2}} q_i \, dV_i = \sum_{n=n_1}^{n_2-1} q_i^n \left(V_i^{n+1} - V_i^n\right) .$$

The quantities $\left(\frac{\partial L}{\partial M}\right)_i^n$ are calculated using the pressures, temperatures, and so on at t_n. These equations are a non-linear system for T_i^{n+1}, since T_i^n and V_i^n, V_i^{n+1} are presumed to be known.

The boundary conditions are implicit in $\left(\frac{\partial L}{\partial M}\right)_i$. For example,

$$\left(\frac{\partial L}{\partial M}\right)_1 = \frac{L_2 - L_1}{DM1_1} .$$

In the present case L_1 was assumed to be always the equilibrium luminosity of the star, L_o. At the surface L_{N+1} is presumed to be expressed in terms of temperatures inside sphere N+1 only, for example as it might be with the Eddington approximation:

$$L_{N+1} = 4\pi (R_{N+1})^2 \, 2\sigma (T_N)^4 .$$

In this study L is given by radiative transfer only. The very optically thick expression for L as applied in stellar interiors is

$$L_i = \frac{16\pi^2}{3} (R_i)^2 \, \frac{S_{i-1} - S_i}{DTAU_i} ,$$

where $DTAU_i$ (analogous to $DM2_i$) is

$$\frac{1}{2} \left(DTAU1_i + DTAU1_{i-1} \right)$$

and where

$$DTAU1_i = \frac{\kappa_i \, DM1_i}{2\pi \left((R_{i+1})^2 + (R_i)^2 \right)}$$

(analogous to $DM1_i$). In addition

$$S_i = \frac{\sigma}{\pi} (T_i)^4$$

(the gray body source function in stellar atmospheres.) Then using these values for L_i ,

$$\left(\frac{\partial L}{\partial M} \right)_i = \frac{L_{i+1} - L_i}{DM1_i} .$$

These expressions were used in the present model for $\partial L / \partial M$ for all shells i, with $i < i_o$ where $DTAUl_j < 8$ for $j > i_o+1$. The following development was used for the shells with $i \geq i_o$.

Assume that r is constant, temporarily.

Then $$\frac{\partial L}{\partial M} = -\varkappa \frac{\partial F}{\partial \tau}$$

where $F(\tau)$ is the flux density and is related to the specific intensity $I(\mu)$ by

$$F = 2\pi \int_{-1}^{1} I(\mu)\mu \, d\mu .$$

The equation of transfer in the approximation considered here is

$$\mu \frac{\partial I}{\partial \tau} = I - S ,$$

where the frequency dependence is incorporated in the use of the Rosseland mean opacity $\varkappa$ in computing τ. From this it follows that

$$\frac{\partial F}{\partial \tau} = 4\pi \left\{ \frac{1}{2} \int_0^\infty E_1(|t-\tau|) S(t)\, dt - S(\tau) \right\}$$

$$= 4\pi \left\{ -\frac{1}{2} E_2(\tau) S(0) + \frac{1}{2} E_3(\tau) \frac{dS}{d\tau}\Big|_0 + \frac{1}{2} \int_0^\infty E_3(|t-\tau|) \frac{d^2 S}{dt^2}\, dt \right\}.$$

But it is known that the exact solution of the Milne problem, $h(\tau) = \tau + q(\tau)$, satisfies

$$0 = 4\pi \left\{ \frac{1}{2} \int_0^\infty E_1(|t-\tau|) h(t)\, dt - h(\tau) \right\}$$

$$= 4\pi \left\{ -\frac{1}{2} E_2(\tau) h(0) + \frac{1}{2} E_3(\tau) \frac{dh}{d\tau}\Big|_0 + \frac{1}{2} \int_0^\infty E_3(|t-\tau|) \frac{d^2 h}{dt^2}\, dt \right\}.$$

Therefore we can represent $-\partial L/\partial M$ as

$$\chi\frac{\partial F}{\partial \tau} = 4\pi\chi\left\{\frac{1}{2}E_3(\tau)\left[\frac{dS}{d\tau}\Big|_0 - \frac{S(0)}{h(0)}\frac{dh}{d\tau}\Big|_0\right] + \frac{1}{2}\int_0^\infty E_3(|t-\tau|)\frac{d^2}{dt^2}\left(S - \frac{S(0)}{h(0)}h\right)dt\right\}.$$

When we approximate this expression using a finite grid of τ it is adequately accurate and most convenient to discard the term in surface derivatives. Now if we reintroduce the variation of r with optical depth in a convenient manner we find

$$-\frac{\partial L}{\partial M} = \frac{2\pi\chi}{r^2}\int_0^\infty E_3(|t-\tau|)\frac{d}{dt}\left(r^2\frac{dS}{dt} - \frac{R^2 S(0)}{h(0)}\frac{dh}{dt}\right)dt.$$

It should be noted that if the optical depths are large the second term in parenthesis is a constant and the outer derivative can be treated as a constant across the interval in which $E_3(|t-\tau|)$ is appreciable, giving

$$-\frac{\partial L}{\partial M} \longrightarrow \frac{2\pi\chi}{r^2}\frac{d}{d\tau}\left(r^2\frac{dS}{d\tau}\right)\int_{-\infty}^{\infty} E_3(|t-\tau|)\,dt$$

$$= -\frac{16\pi^2}{3}\frac{\partial}{\partial M}\left(r^2\frac{dS}{d\tau}\right)$$

which is equivalent to the diffusion formula used in the optically thick region. The surface boundary condition is implicit in the use of an integral here.

When the finite set of shells is used we derive

$$-\left(\frac{\partial L}{\partial M}\right)_j = A_j\sum_{i=2}^{N+1}(C_i - C_{i+1})f_{ij}$$

where

$$C_i = \frac{R_i^2(S_{i-1} - S_i) - RR(h_{i-1} - h_i)}{DTAU_i}, \quad C_{N+1} = 0$$

$$RR = \frac{(R_{N+1})^2 S_N}{h_N}$$

$$h_i = TAU_i + q(TAU_i)$$

$$f_{ij} = \begin{cases} E_3(|TAU_i - TAU_j|) & TAU_i \le 1 \\ \dfrac{\chi(TAU1_i - TAU_j) - \chi(TAU1_{i+1} - TAU_j)}{DTAU1_i}, & \end{cases}$$

$$\chi(\tau) = \int_{-\infty}^{\tau} E_3(|t|)\,dt \qquad TAU_i > 1$$

and as before

$$DTAU1_i = \frac{\chi_i \, DM1_i}{2\pi(R_i^2 + R_{i+1}^2)}$$

$$DTAU_i = \frac{1}{2}(DTAU1_i + DTAU1_{i-1}),$$

$$DTAU_{N+1} = \frac{1}{2} DTAU1_N$$

and

$$TAU1_i = \sum_{j \ge i} DTAU1_j$$

$$TAU_i = \sum_{j \ge i} DTAU_j$$

$$A_j = \frac{4\pi\chi_j}{R_j^2 + R_{j+1}^2} = 8\pi^2 \frac{DTAU1_j}{DM1_j}.$$

The exponential integrals E_3 and E_4 and the gray body source function $h(\tau)$ which are required here and their derivatives are obtained by the rational approximations given in Appendix B. All the thermodynamic functions and opacities are obtained from tables stored in the computer and the preparation of these tables is described in

Appendix C.

In order to calculate the luminosity itself, for example to find the emergent luminosity, the following expression is used which is compatible with the $\partial L/\partial M$ formula:

$$L_j = \frac{16\pi^2}{3} RR + 8\pi^2 \sum_{i \le N} C_i \left(\chi(TAU_{i-1} - TAU1_j) - \chi(TAU_i - TAU1_j)\right).$$

When the expressions for $-\partial L/\partial M$ are substituted into the difference heat equation a complicated non-linear system results for the new temperatures, as we have seen. This is solved with Newton's method of differential corrections, which yields a linear system to be solved for each correction. The coefficients involve the derivatives of $(\partial L/\partial M)_j^{n+1}$ with respect to each T_i^{n+1} ; in the transfer case these are too complex to reproduce. In terms of them, however, the equations for correcting the T^{n+1} become

$$(T_i^{n+1})_{new} = (T_i^{n+1})_{old} + \Delta T_i$$

$$\sum_i \Delta T_i \left\{ \left[(\delta_j^{n+1} - \delta_j^n) + Cv_j (T_j^{n+1} + T_j^n)/T_j^{n+1} \right] \delta_j^i + Dt_{n+\frac{1}{2}} \frac{\partial}{\partial T_i^{n+1}} \left(\frac{\partial L}{\partial M} \right)_j^{n+1} \right\}$$

$$= -\left\{ (T_j^{n+1} + T_j^n)(\delta_j^{n+1} - \delta_j^n) + Dt_{n+\frac{1}{2}} \left(\left(\frac{\partial L}{\partial M} \right)_j^{n+1} + \left(\frac{\partial L}{\partial M} \right)_j^n \right) + 2 \int q_j \, dV_j \right\}$$

where δ_j^i is the Kronecker symbol. The manner in which the matrix of this system is filled is indicated in Figure 3, that is, the matrix is tri-diagonal (the diffusion region) except for the block in the lower right hand corner where the shells are optically thin (the transfer region) and which is more-or-less completely filled. Because the limiting form for large optical depth of the transfer formulation is just the diffusion formulation the matrix actually becomes smoothly more diagonally concentrated as one proceeds up the diagonal. It becomes essentially tri-diagonal at TAU1 = 10 to 20.

The iteration was continued until all the temperature corrections were less than 10^{-4} relatively. Normally this would require 3 or 4 iterations. If too many iterations were required for convergence or if the temperature change in any shell exceeded 10 percent in the time step, it was reduced and the whole procedure was repeated, from the last heat equation step. If the temperature changes when the iteration was finished were all less than 5 percent the time step was increased for the next step. Each iteration required about 0.5 seconds on a 7094 and the mean time per time step was about 2.4 seconds.

The details of the choice of the mass shells require some elaboration at this point. The possible

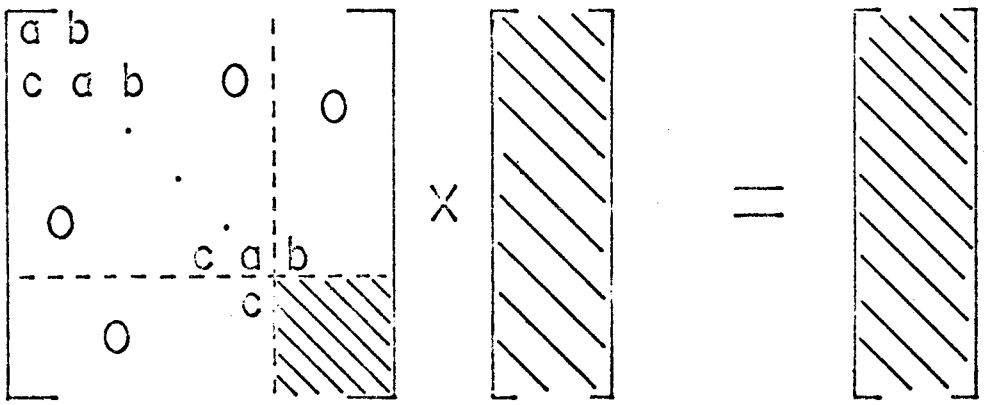

Figure 3. Configuration of the linear system for the temperature corrections

divisions are restricted greatly by the necessity of providing a suitable scale of τ in the critical region $.1 \leq \tau \leq 10$. A permissable variable of τ in this range is 30 percent per shell. If the shells are chosen to accord with this condition, it is found that about 10 are needed within 0.1 in $\ln(p)$ of the center of the H zone. Furthermore this is true at all times in the calculation, which means that either an enormous number of shells must be used or the shells must be shifted as the H zone moves back and forth.

In order to limit the number of shells, then, it was necessary to interpolate new ones and discard old ones every few time steps in the calculation. This interpolation was done either linearly or quadratically, in Ml or M, as determined by how sensitive the calculation was to interpolation noise in the particular quantity in question: T, R or $\frac{\partial L}{\partial M}$. All shells below a certain optical depth (1000) were left unchanged, as was the surface sphere.

It was found that for any reasonable accuracy of the results for T and to avoid excessive errors due to the assumption about the variation of p between heat equation steps T must not change by more than 10 percent in a single heat equation step in any shell. If that is so, then interpolation takes place every 4 steps approxi-

mately. This condition on the permissable rate of change of T poses serious problems in computation time; this will be discussed again later.

The precise manner in which the shells were chosen was as follows: M1(N+1) was derived from DM1(N) as was discussed above. Then, proceeding inward a constant increment DLGDM1 in M1 was used until the increment in $N(\tau 1) = 5.78\ln(1+5.78\ln(1+\tau 1/2))$ would have exceeded 1. At that point and after, M1 was adjusted to make the increment in $N(\tau 1)$ just 1, until the increment in M1 exceeded DLGDM1 again, whereafter the constant increment DLGDM1 was used again until $(R_{i+1}-R_i)/c_{s_i}$, the sound travel time across the shell, reached a minimum, then for the remainder the shells were chosen so as to make the sound travel time constant. The innermost shell was found when another could not be inserted inside in this manner.

This was the procedure for choosing the mass division in the equilibrium model. In the dynamic calculations the shells were adjusted in this manner: if the change in $N(\tau 1)$ across any one exceeded 1.7 then a whole new mesh was interpolated for all the region controlled by $N(\tau 1)$, in order to make the increments in $N(\tau 1)$ equal to 1 again, or to restore the DLGDM1 spacing, as appropriate. $N(\tau 1)$ as given above

provides for $\tau \leq 10$ a grid of τ suited to performing the quadratures. For $\tau > 10$ the spacing of the shells increases enormously, so that the region of DLGDM1 spacing is reached at about $\tau 1 = 100$.

The equilibrium model was constructed using the same (spatial) difference expressions given above for the dynamical calculation, but requiring the time variation to vanish. The resultant equations

$$P_{i-1} = P_i + \frac{G \cdot MO_i}{4\pi R_i^4} DM2_i$$

$$\begin{cases} C_i = 0 & \text{with} \quad RR = \frac{3}{16\pi^2} L_o \\ \text{or} \\ L_i = L_o \end{cases}$$

$$R_{i-1}^3 = R_i^3 - \frac{3}{4\pi} V_{i-1} DM1_{i-1}$$

were solved in turn, beginning at the surface. While P_{i-1} is obtained explicitly, the equation for heat balance had to be solved iteratively for T_{i-1}, then R_{i-1} was obtained explicitly. When the mass increment was adjusted, as in the H zone and near the core, a further iteration on that quantity was performed.

Part II. Results of the Dynamical Calculations

A. Summary of the Calculations

The model which was chosen for the study is the one which Christy denotes by 5g (Christy 1966a). The parameters are:[1]

$$M = 1.15 \times 10^{9} = .58 M_{\odot}$$
$$L = 1.5 \times 10^{4}, \quad M_{bol} = .76$$
$$T_e = .65, \quad \theta_e = .775$$
$$Y = .30$$
$$Z = .002.$$

The radius is 3434 = 4.9 $R_{\odot}$, the surface gravity is 6.58 (log g = 2.82 cgs), the fraction of (potential) convective flux is .11 according to Christy, and the period is 46.35 or 0.536 days, which implies a Q of .0373.

This model was chosen from Christy's grid since the T_e and M_{bol} fit most closely the values obtained by Oke et al (Oke 1966a, Oke and Bonsack 1960, and Oke, Giver and Searle 1962) for SU Dra, RR Lyr, and X Ari while the mass estimates of these stars lie between .58 $M_{\odot}$ (5g) and .38 $M_{\odot}$ (4e). Model 5g has a somewhat larger amplitude than 4e, and since it was desired to study the larger amplitude, Bailey a-type characteristics,

[1] The units here and elsewhere are cgs as modified by various powers of 10 to make them more convenient. A tabulation is given in Appendix D.

the larger mass was chosen. The characteristics of the equilibrium model and the runs of the variables are given in Table I.

In view of the prohibitive amount of computation time which several pulsation periods of dynamical calculation using the fine set of mass shells and the transfer formulation would have required, it was decided that a relaxed large amplitude periodic solution to the full transfer problem could not be obtained. Instead the objective was as follows: the effect of the fine grid and the transfer approach would not be substantial on the nature of the pulsation in the layers deeper than the H zone, unless, that is, Christy's approximate treatment of the H zone were seriously in error. With this in mind, the final model was obtained by performing one and one-half periods of transfer calculation with the methods discussed in the preceding part (which will be called the transfer model), using as initial conditions the relaxed solution of the same equations, except for the omission of the finely zoned region and the substitution of diffusion (using Christy's expression for the flux [Christy 1964]) for transfer in and above the H zone (this will be called the diffusion model). This relaxed solution of the diffusion problem was obtained by doing eight periods of this type of calculation using Christy's final constant amplitude results for this star as initial conditions.

I	Ml	R	TAUl	M	T	logp	logv	ρ	$\varkappa$	C_S	C_V
1	15.6735	875.48	7.751E 07	15.3624	85.0702	1.0382	3.0244	2261.	1.807	137.94	221.
2	14.9086	1153.93	3.053E 07	14.6314	62.1439	0.4009	3.5267	2354.	2.302	117.93	224.
3	14.2466	1391.79	1.434E 07	13.9919	48.4675	-0.1114	3.9324	2431.	2.806	104.18	230.
4	13.6493	1601.83	7.476E 06	13.4097	39.3032	-0.5470	4.2786	2498.	3.332	93.86	234.
5	13.0940	1791.12	4.162E 06	12.8648	32.6774	-0.9316	4.5847	2557.	3.893	85.63	247.
6	12.5636	1963.77	2.413E 06	12.3440	27.6120	-1.2806	4.8620	2611.	4.500	78.75	245.
7	12.0569	2122.68	1.432E 06	11.8379	23.5623	-1.6044	5.1182	2660.	5.164	72.77	255.
8	11.5569	2269.47	8.549E 05	11.3379	20.1769	-1.9108	5.3585	2704.	5.894	67.37	268.
9	11.0569	2406.10	5.024E 05	10.8379	17.2497	-2.2050	5.5859	2745.	6.561	62.33	260.
10	10.5569	2531.56	2.889E 05	10.3379	14.7203	-2.4885	5.8010	2780.	6.909	57.60	270.
11	10.0569	2645.15	1.648E 05	9.8379	12.5975	-2.7631	6.0070	2811.	6.858	53.24	275.
12	9.5569	2747.21	9.600E 04	9.3379	10.8710	-3.0304	6.2116	2846.	6.765	49.49	263.
13	9.0569	2839.58	5.762E 04	8.8379	9.4699	-3.2917	6.4140	2882.	6.839	46.20	270.
14	8.5569	2923.49	3.551E 04	8.3379	8.3103	-3.5479	6.6137	2918.	7.168	43.25	272.
15	8.0569	2999.80	2.220E 04	7.8379	7.3231	-3.7994	6.8124	2956.	7.708	40.55	291.
16	7.5569	3069.45	1.393E 04	7.3379	6.4612	-4.0466	7.0067	2992.	8.430	37.89	307.
17	7.0569	3132.73	8.675E 03	6.8379	5.6863	-4.2897	7.1935	3021.	9.389	34.89	352.
18	6.5569	3189.53	5.260E 03	6.3379	4.9603	-4.5290	7.3715	3036.	10.574	31.13	521.
19	6.0569	3239.71	3.005E 03	5.8379	4.2636	-4.7646	7.5306	3011.	11.129	27.66	641.
20	5.5569	3282.38	1.606E 03	5.3379	3.6402	-4.9971	7.6865	2992.	9.593	26.72	412.
21	5.0569	3318.55	8.915E 02	4.8379	3.1513	-5.2271	7.8516	3005.	8.123	25.84	267.
22	4.5569	3350.00	5.321E 02	4.3379	2.7661	-5.4547	8.0225	3030.	7.970	24.33	271.
23	4.0569	3377.77	3.220E 02	3.8379	2.4149	-5.6795	8.1879	3051.	9.171	22.60	276.
24	3.5569	3402.05	1.775E 02	3.4113	2.0637	-5.8685	8.3036	3044.	13.545	19.97	370.
25	3.2408	3415.14	89.3638	3.1922	1.7520	-5.9646	8.3129	2961.	24.567	16.80	688.
26	3.1411	3418.54	48.7534	3.1252	1.5165	-5.9939	8.2635	2858.	41.284	15.83	485.
27	3.1090	3419.45	28.1702	3.1026	1.3340	-6.0038	8.1996	2757.	55.606	13.98	846.
28	3.0961	3419.75	17.3324	3.0924	1.1924	-6.0063	8.1069	2543.	55.261	12.10	2283.
29	3.0887	3419.90	11.2057	3.0855	1.0794	-6.0113	7.9866	2239.	38.820	10.44	7365.
30	3.0823	3420.00	7.4958	3.0785	0.9859	-6.0143	7.8873	2006.	21.559	9.25	1613.
31	3.0747	3420.08	5.0921	3.0704	0.9102	-6.0179	7.8191	1874.	11.066	8.56	903.
32	3.0660	3420.17	3.6693	3.0595	0.8483	-6.0227	7.7757	1807.	5.649	8.20	646.
33	3.0529	3420.28	2.5981	3.0450	0.7955	-6.0290	7.7448	1768.	2.926	8.00	466.
34	3.0370	3420.41	1.9343	3.0249	0.7516	-6.0378	7.7246	1745.	1.578	7.93	257.
35	3.0128	3420.59	1.3973	2.9963	0.7117	-6.0502	7.7111	1730.	0.849	7.90	198.
36	2.9796	3420.82	1.0147	2.9572	0.6777	-6.0674	7.7057	1720.	0.474	7.89	159.
37	2.9342	3421.13	0.7329	2.9032	0.6482	-6.0909	7.7093	1714.	0.272	7.88	135.
38	2.8712	3421.53	0.5204	2.8274	0.6220	-6.1240	7.7241	1711.	0.159	7.83	119.
39	2.7817	3422.07	0.3570	2.7174	0.5984	-6.1721	7.7552	1711.	0.093	7.77	110.
40	2.6488	3422.85	0.2299	2.5466	0.5767	-6.2467	7.8137	1716.	0.054	7.69	111.
41	2.4328	3424.06	0.1299	2.2137	0.5555	-6.3921	7.9428	1731.	0.028	7.58	106.
42	1.9328	3426.73	0.0442	1.7137	0.5393	-6.6103	8.1482	1758.	0.015	7.48	103.
43	1.4328	3429.32	0.0164	1.2137	0.5321	-6.8282	8.3606	1789.	0.010	7.43	105.
44	0.9328	3431.68	0.0051	0.7137	0.5285	-7.0459	8.5757	1820.	0.007	7.39	109.
45	0.4328	3434.42	0.								

Table I

I is the sphere number for Ml, R, and TAUl, and the shell number for the others; all quantities are in the units of Appendix D except $\varkappa$ which is in cm^2/gm.

The methods used here for the diffusion calculation are formally equivalent to Christy's, but use entropy rather than internal energy in the heat equation, and the choice of mass shells and the equation of state table were somewhat different. To relax these differences was the purpose of doing additional diffusion calculation prior to introducing the more complicated atmospheric treatment.

Calculations of model 5g pulsating in the fundamental were obtained from Christy which cover approximately three periods of pulsation after the model had been driven to slightly more than full amplitude (as evidenced by a very slight decline in the kinetic energy amplitude). These calculations include the effects of radiation pressure which were neglected in the earlier version of this model (Christy 1966a).

For comparison with the later models Figure 4 shows the variation of U, L, T_e, g_e, and R with time, these quantities having been obtained from the model details in the same manner as for the later calculations; which is that U, g_e, and R refer to the depth $\tau = 2/3$, L is the emergent luminosity and T_e is inferred from L and R. The choice of $\tau = 2/3$ rather than the surface for the reference location of U and g_e was motivated by the desire to avoid complicating the velocity and gravity

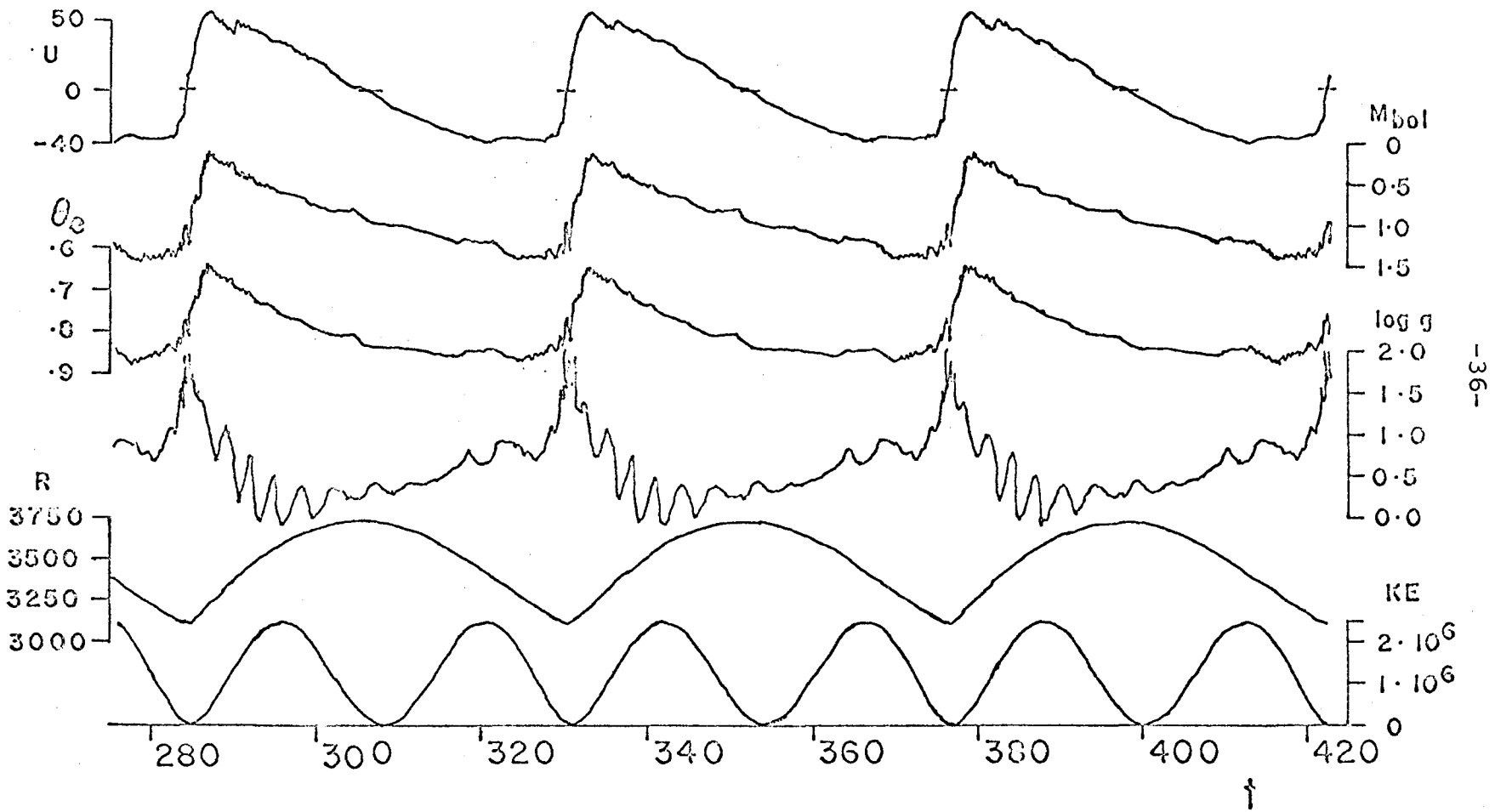

Figure 4. Exterior variables and kinetic energy versus time for Christy's model

curves with the effects of the mechanical disturbances which are apt to occur at very small optical depths, but to show the velocity and gravity which observations would probably indicate.

The influence of the coarse mass division is apparent in the luminosity and temperature curves, both on the ascending and the descending branch. It is also marked, for a rather different reason, in the gravity and velocity curves on the descending branch. This is due to the low pressure region which should exist just outside the H zone at this time, about which there will be much to say later, but which appears and disappears in this calculation as the H zone crosses the mass shells.

At the phase, just prior to minimum luminosity, when the luminosity L was constant across the H zone, that is, the H zone was approximately at maximum depth, the values of $\ln(p/p_o)$, T/T_o, and U were found as a function of exterior mass from Christy's model, where p_o and T_o are the equilibrium pressure and temperature of the same mass shell. These quantities were interpolated to the mass coordinates of the shells in the diffusion calculation, which were also, except in the H zone, the same as the shells in the transfer model. The interpolated quantitites were then combined with the equilibrium values for the diffusion model and the results used to

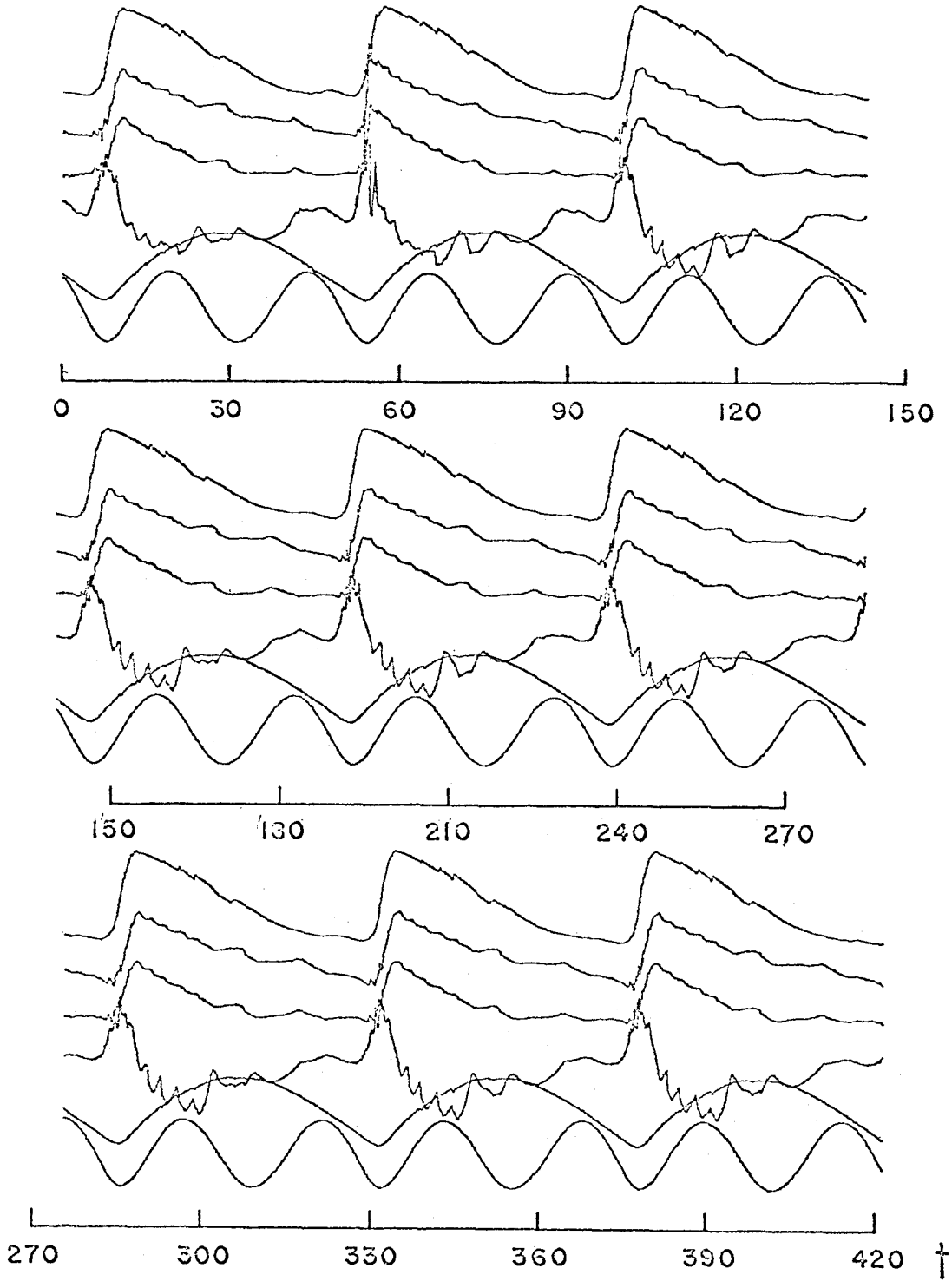

Figure 5. The same quantities as Figure 4 for the diffusion model.

initiate the eight periods of diffusion calculation.

The results from this are indicated in Figure 5 showing the same quantities as in the previous figure. There is much similarity to Christy's results, as should be expected, but also a reaction, most visible in the second luminosity maximum, to the discrepancies which exist between the two calculations in detail. The most serious of these was the change in the radius of the fixed central sphere from 575 in Christy's model to 890 in the other. This reaction decayed in the course of the calculation so that the last two or three periods show much better repetition than the first few. It should be noticed also that the first period, before the discrepancies could reach the surface, agrees fairly well with the last few, while the second period is much different.

If the diffusion model is compared to Christy's the only really noticeable difference is the disappearance of the bump in the velocity curve at minimum light. In Christy's model the bump is due to a shock which occurs at that time and indeed there is a shock about then in the diffusion model, but it occurs somewhat earlier and doesn't seem to be detectable in the photospheric velocity. The difference is most likely due to the extra mass attached to the surface in the diffusion calculation. This has the effect of changing the response time of the outer layers

to a mechanical disturbance because of the reduction in sound travel time. However the transfer model will show that the H zone behavior is also related to these pre-compression shocks and the difference might well be due to the different choice of mass shells near the H zone.

Finally the diffusion results after eight periods were summarized with the same quantities at the same phase as was done with Christy's model. These were imposed on the transfer model as follows. In the quasi-abiabatic region $T > 30,000$ degrees, the values of $\ln(p/p_o)$, T/T_o, and U were used directly, just as before. However, for the cooler region it was not possible to use T/T_o directly, since approximate flux constancy had to be obtained. Instead $\ln(p/p_o)$ was used directly and an atmosphere in thermal equilibrium was attached which gave the correct temperature in the outermost shell of the inner region. For this reason the transfer model could only be initiated when the flux was essentially constant in the cooler region.

Using these initial conditions 3600 (heat equation) integration steps were calculated, representing approximately one and one-half periods of pulsation. A single period required 2000 steps, 1500 steps on the ascending branch and 500 on the descending branch.

The following is helpful in understanding the number of steps required. The time increment in a single

step was adjusted to make the maximum temperature change about 10 percent. Since this maximum almost always occurred in the H zone as that region swept back and forth in the atmosphere, and since the profile of the zone did not alter greatly as it moved, the time step can be given by

$$\Delta t = 0.1 \frac{\left(\frac{d\log p}{d\log T}\right)_{min}}{\left(\frac{d\log p}{dt}\right)_{zone}} \quad , \quad \text{or} \quad (\Delta \log p)_{zone} = \frac{0.1}{\nabla_{max}}$$

where ∇_{max} is the maximum of dlog T/dlog p in the H zone. If n_H is the number of scale heights the H zone must traverse each way in a period, the number of steps required (one way) is given by

$$n_S = 10 n_H \nabla_{max} .$$

Now, ∇_{max} is given by

$$\nabla_{max} = \frac{3}{16}\left[\frac{T_e^4}{T^4}\frac{\kappa p}{4g}\right]_{max}$$

where g is the effective gravity. The value of ∇_{max} for the equilibrium model is 20, and it varies roughly as

$$T_e^{-8} g^{-.1} .$$

If ∇_{max} were always 20, then for $n_H = 3$ (as for this model) we would have $n_s = 600$. Unfortunately the actual outward motion of the H zone occurs mostly when T_e is less than the equilibrium value, so that ∇_{max} is closer to 50 than to 20, hence n_s is 1500 rather than 600

for the outward swing of the H zone. The inward swing occurs when T_e is hotter on the average, so the number is 500 instead of 1500. Notice: if ∇_{max} never exceeded the abiabatic value of 0.4, n_s would be less than 24! Consequently the H zone would not be the determining factor in the time step.

B. Physical Description of the Dynamical Model

The remainder of this part will be devoted to a discussion of the details of the transfer model calculations themselves. The relationship of the model to real type a RR Lyrae stars will be reserved for the next part.

1. Exterior Quantities

Figure 6 shows the variation with time of U, M_{bol}, θ_e, log g_e, R and KE. U, g_e, and R refer as before to tau = 2/3. U here refers to dr/dt; the observed radial velocity from weak lines is $-\langle\mu\rangle U$, where μ is the direction cosine of the surface normal with respect to the line of sight. A discussion of the evaluation of $\langle\mu\rangle$ is given in Appendix E, the result being that reasonable values cluster near .75 if moderate dispersions are used.

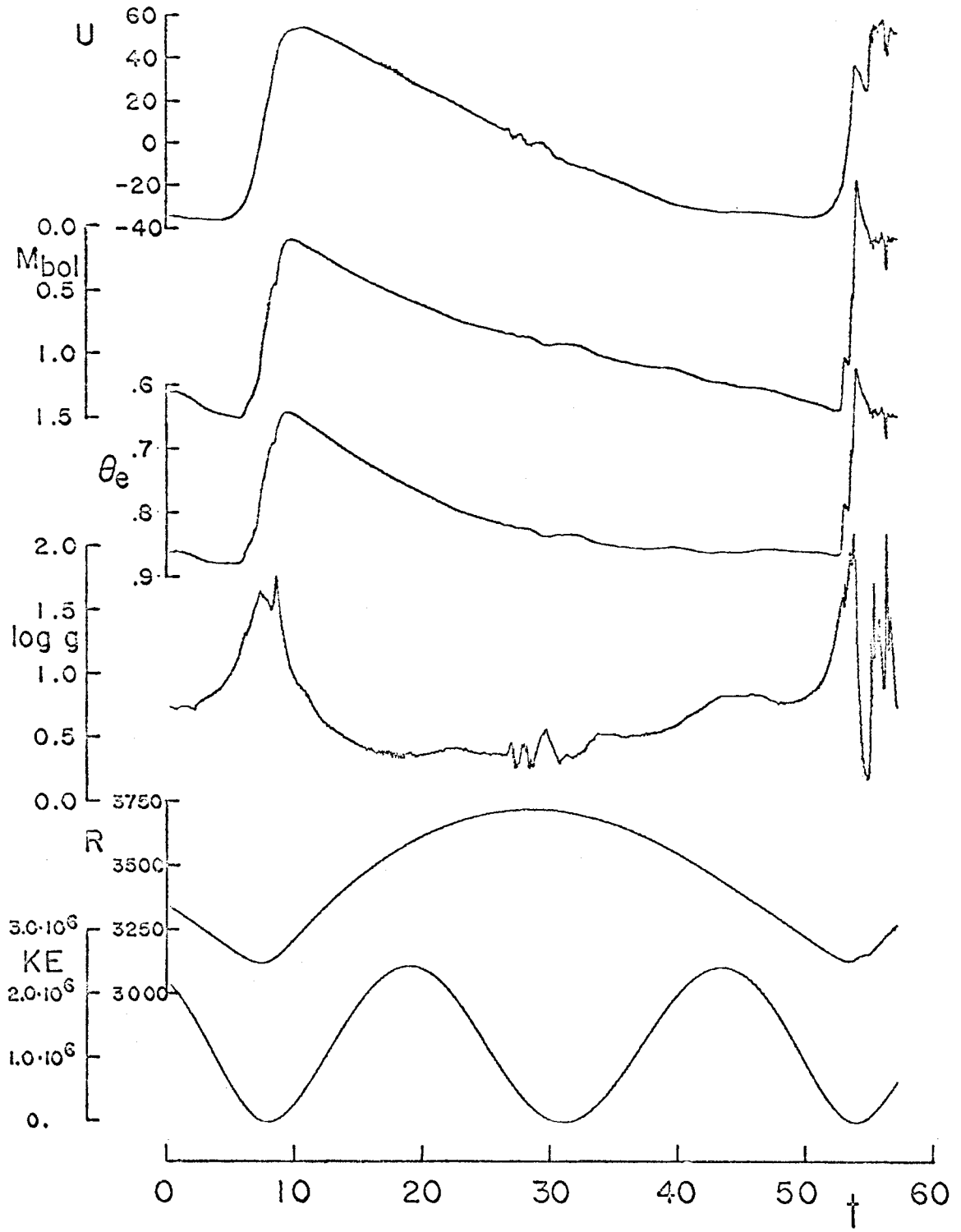

Figure 6. The same quantities as Figure 4 for the transfer model.

There is a useful relation between the velocity and gravity curves, which is

$$\frac{dU}{dt} + g_e = \frac{GM}{R^2}$$

which is valid as long as the atmosphere can be considered to be in quasi-hydrostatic equilibrium. Thus near the velocity minimum, when U is fairly constant, the gravity oscillates around the equilibrium value, log g = .82. This can be used to provide a check on the photometrically obtained gravities.

The irregularities in the velocity and gravity curves near t = 18 are numerical. They are the equivalent in this model of the large oscillations at the same phase in the previous models. They arise here because of interpolation errors near tau = 1.

The oscillations from t = 27 to t = 30 are real, however. They indicate the disturbance in the atmosphere caused by the shock just referred to interacting with the ionization front as the latter slowed its inward motion.

Table II contains a summary of the extrema, amplitudes and phases for these curves. The phases are based on the time, 9.70, of luminosity maximum and the period, 46.35. We notice that the median of M_{bol}, .78, agrees very well, in this case, with the luminosity mean

Table II

quantity	max	min	med	ampl.	ϕ_{max}	ϕ_{min}	ϕ_{med}
M_{bol}	.08	1.48	.78	1.40	0	.913	.956 .334
U	55.2	-35.7	9.7	90.9	.026	.875	.956 .341
$\log g_e$ (cgs)	3.65 3.75	2.40	-	1.35	.950 .976	.201	-
θ_e	.637	.875	.756	.238	.995	.898	.953 .209
R	3727	3126	3426	601	.406	.950	.096 .743
KE	$2.45.10^6$	10^4:	-	$2.45.10^6$	.201 .729	.005 .463	-

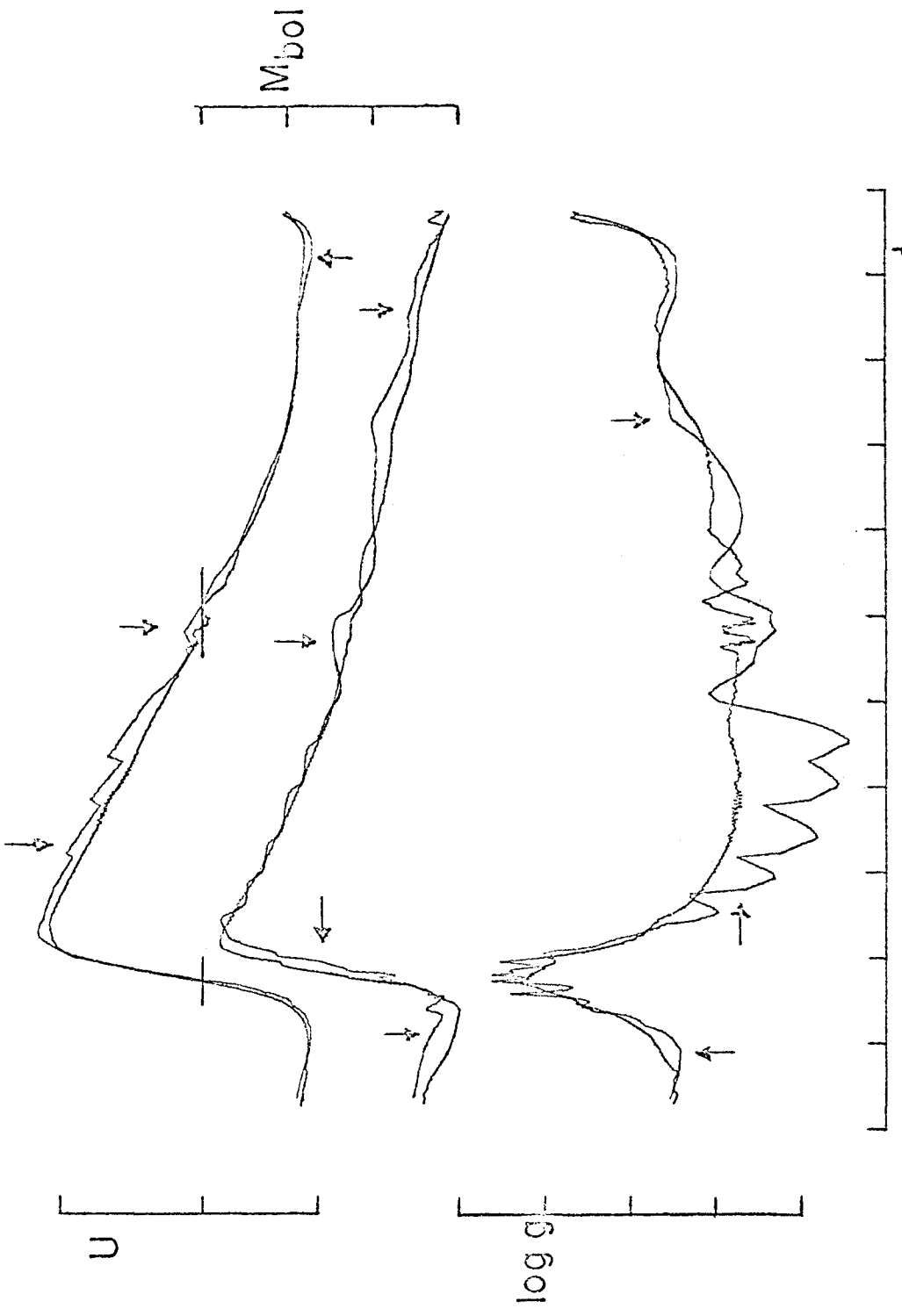

Figure 7. Comparison of the transfer model with diffusion cycle 8. Ordinate scales are as in Figure 4. The time division is 5 units. The arrows indicate the diffusion model.

M_{bol} = .76. The median velocity, 9.7 km/sec greater than the mean, occurs at the same phases as the median M_{bol}, indicative of the classical similarity of these curves. The Θ_e curve, which generally mimics the luminosity curve, has a median which is .02 hotter than the equilibrium value. The radius amplitude is, like the M_{bol} variation, symmetrical around the mean. The gravity variation, although rather more complicated than that of the other quantities, does have some general properties. The positive excursion is .93 while in the negative direction it is only -.42, that is, the gravity ranges from 40 percent to 8 times the equilibrium value. Although the range is large, the descending branch value is high enough to make the velocity curve slope only about half of GM/R^2 and to preserve the validity of the plane-parallel approximation.

Figure 7 is a comparison of the first period of transfer calculation with the diffusion model in the quantities U, M_{bol}, and g_e. The time zero point was adjusted to make the phases of minimum kinetic energy coincide. It would seem that the two methods do produce similar results overall; the transfer luminosity curve falls along the smoothed diffusion version, and the velocity curve is essentially the same, down to the behavior at minimum light. The gravity curves are similar

bearing in mind the differences near the minimum caused by the coarse mass division in the diffusion model.

Gross differences appear in the second period. The luminosity and velocity rise much too quickly and the luminosity reaches a very high, brief maximum, followed by a plateau at the level of its first maximum. The velocity reaches a maximum and declines until a strong shock lifts it to another maximum. All this can be understood in terms of the behavior of the ionization zone, and for the present it suffices to say that the first period is much more representative of what could be expected from a relaxed model than the unpleasantness which follows.

Some interesting details which should be noticed are the depressions in the luminosity curve, especially the one which occurs at $t = 8.5$, and the correlation of these with peaks in the gravity curve. This is seen very strikingly also in the M_{bol} and log g variations during the second rise. This effect is also responsible for the major depression in M_{bol} at the onset of the first compression phase.

2. Internal Dynamics I. The Linear Interior

The figures 8a - 8hh show the variation with depth ($\ln(MT-M_r)$) of the velocity and PNO = $\ln(p/p_o)$ at several phases of the pulsation. The most interesting

Caption to Figure 8

The succeeding nine pages show 34 "snapshots" of the distributions of pressure and velocity in the model star, Figures 8a through 8hh. The variables plotted are the pressure variation PNO, defined in the text, and the outward velocity of the mass, U. The abscissa is the variable M or M1, which both refer to $\log_e(M-M_r)$. The scales are:

in U: -40 km/sec to 40 km/sec in steps of 10 km/sec

in PNO: -2.5 to 2.5 in steps of 0.5

in M or M1: 0 to 16 in steps of 1.0, with longer ticks at 5, 10, 15.

The number given on each plot is the time, t.

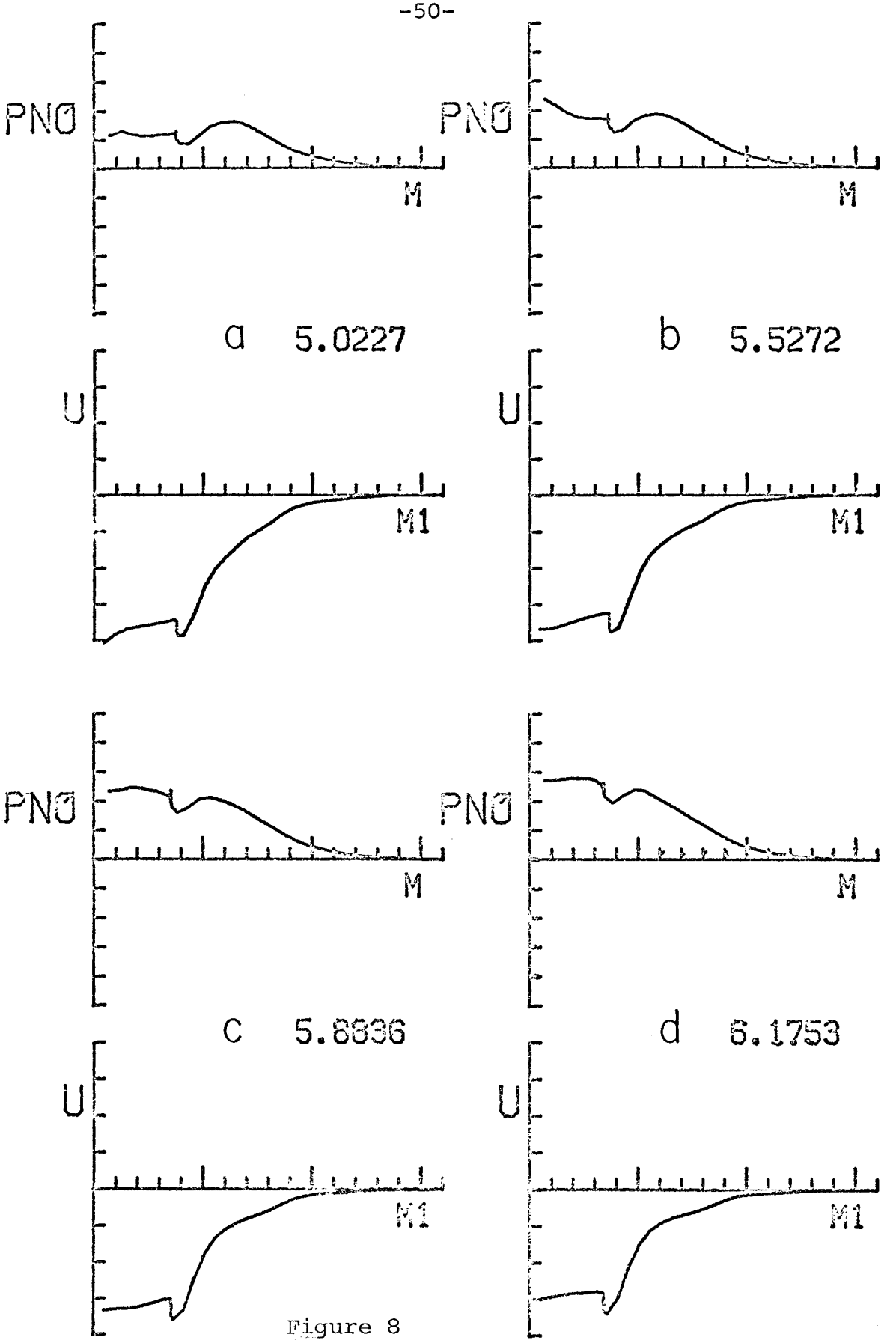
PNØ
M
a 5.0227
U
M1
PNØ
M
b 5.5272
U
M1
PNØ
M
c 5.8836
U
M1
PNØ
M
d 6.1753
U
M1

Figure 8

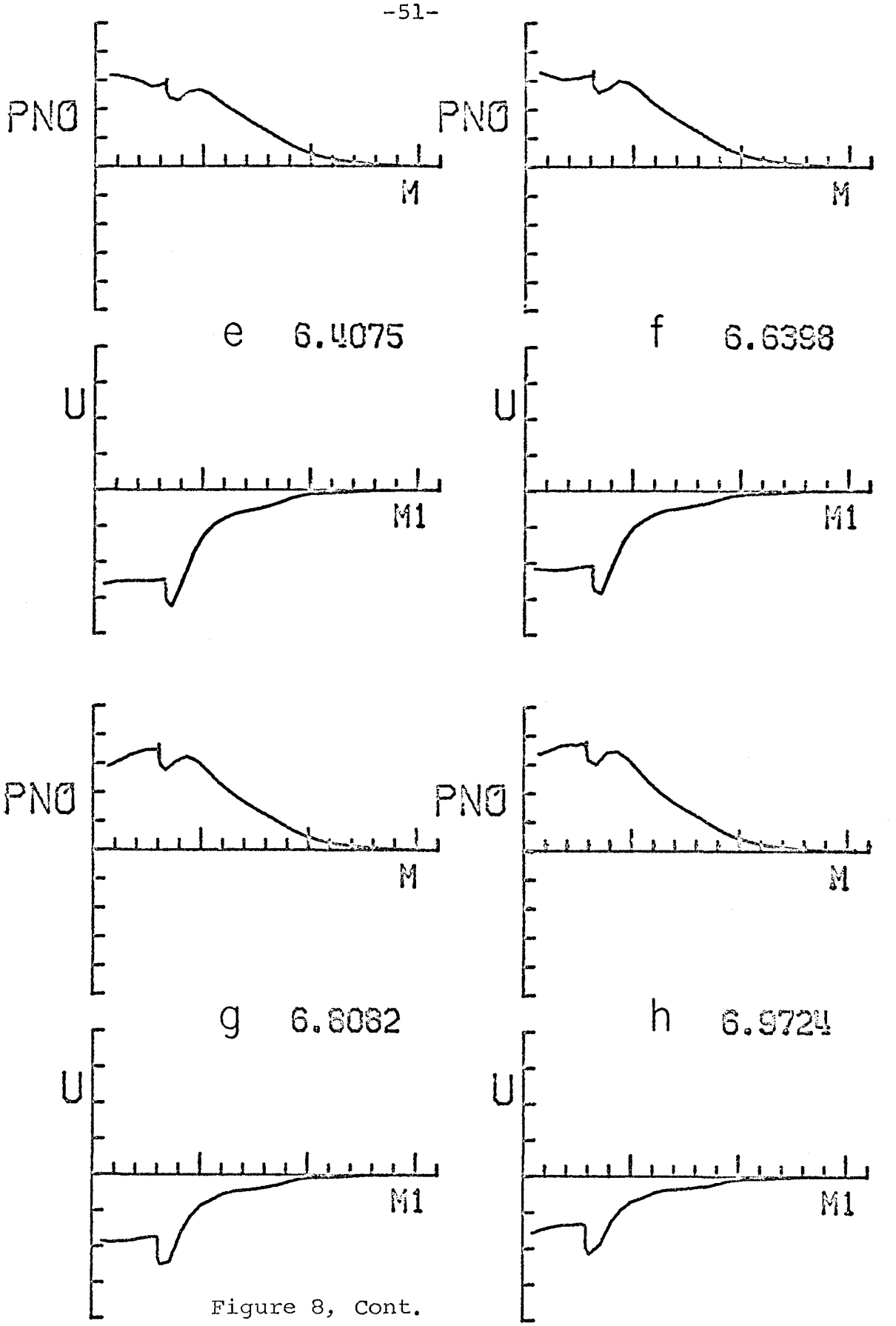

Figure 8, Cont.

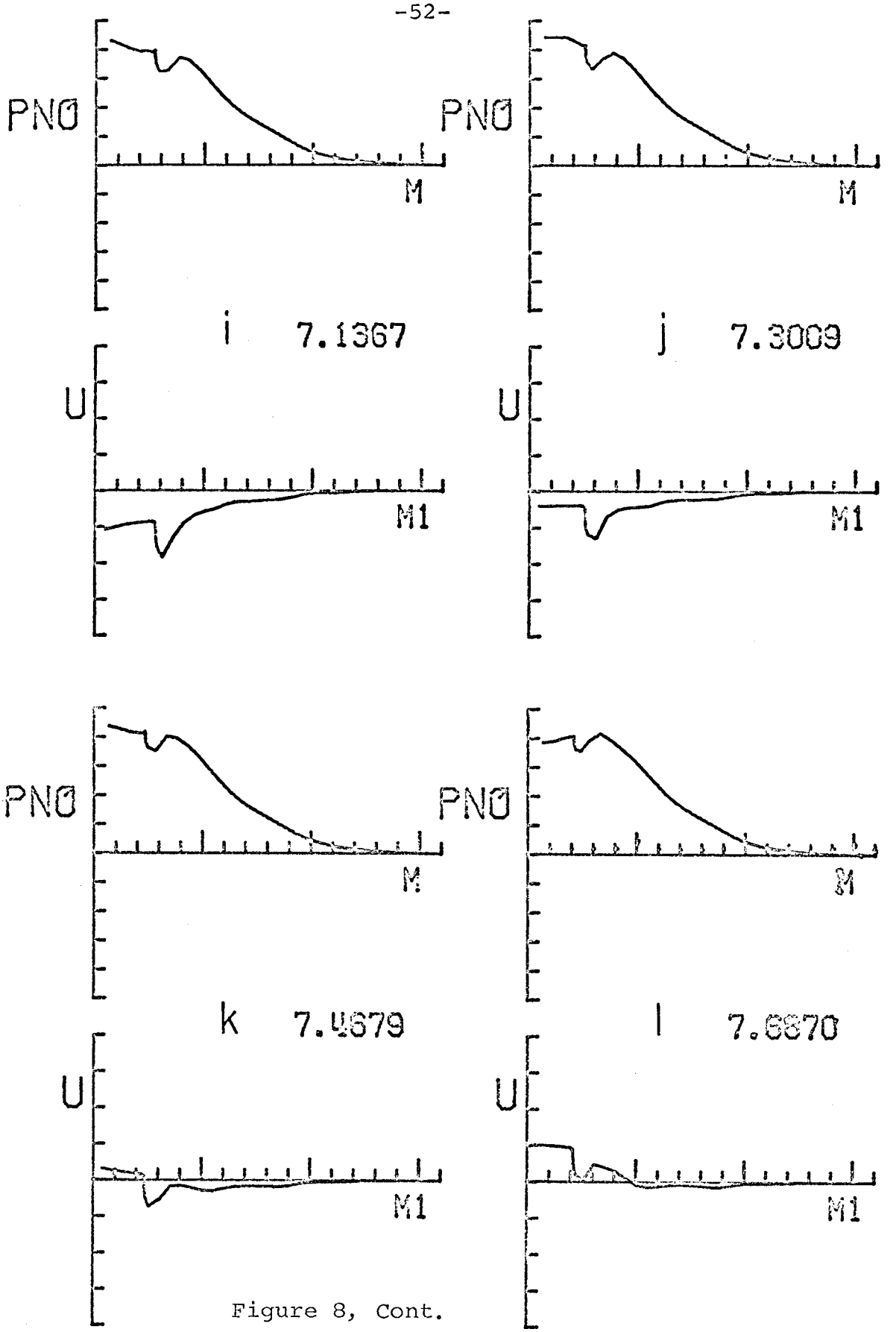

Figure 8, Cont.

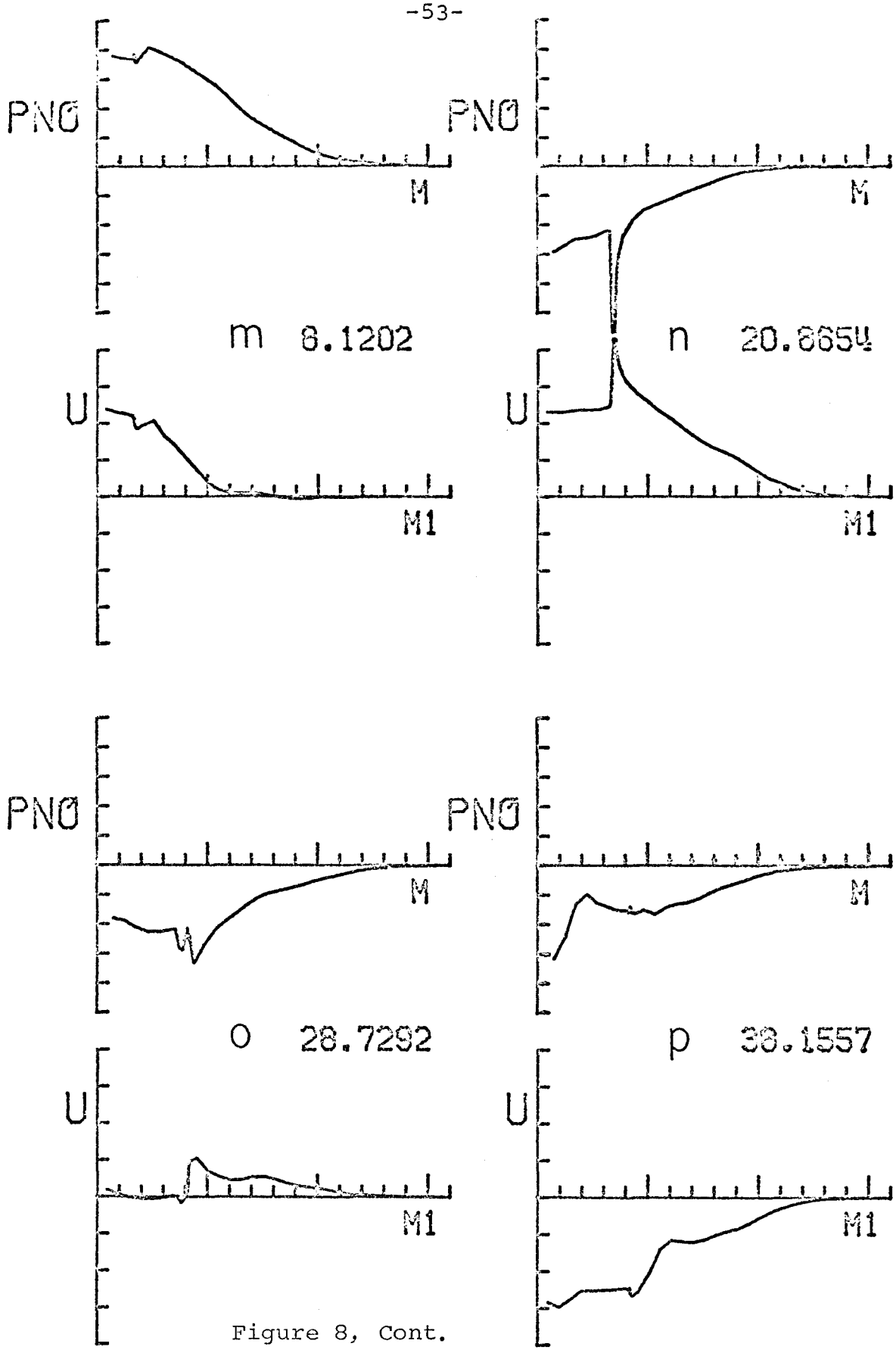

Figure 8, Cont.

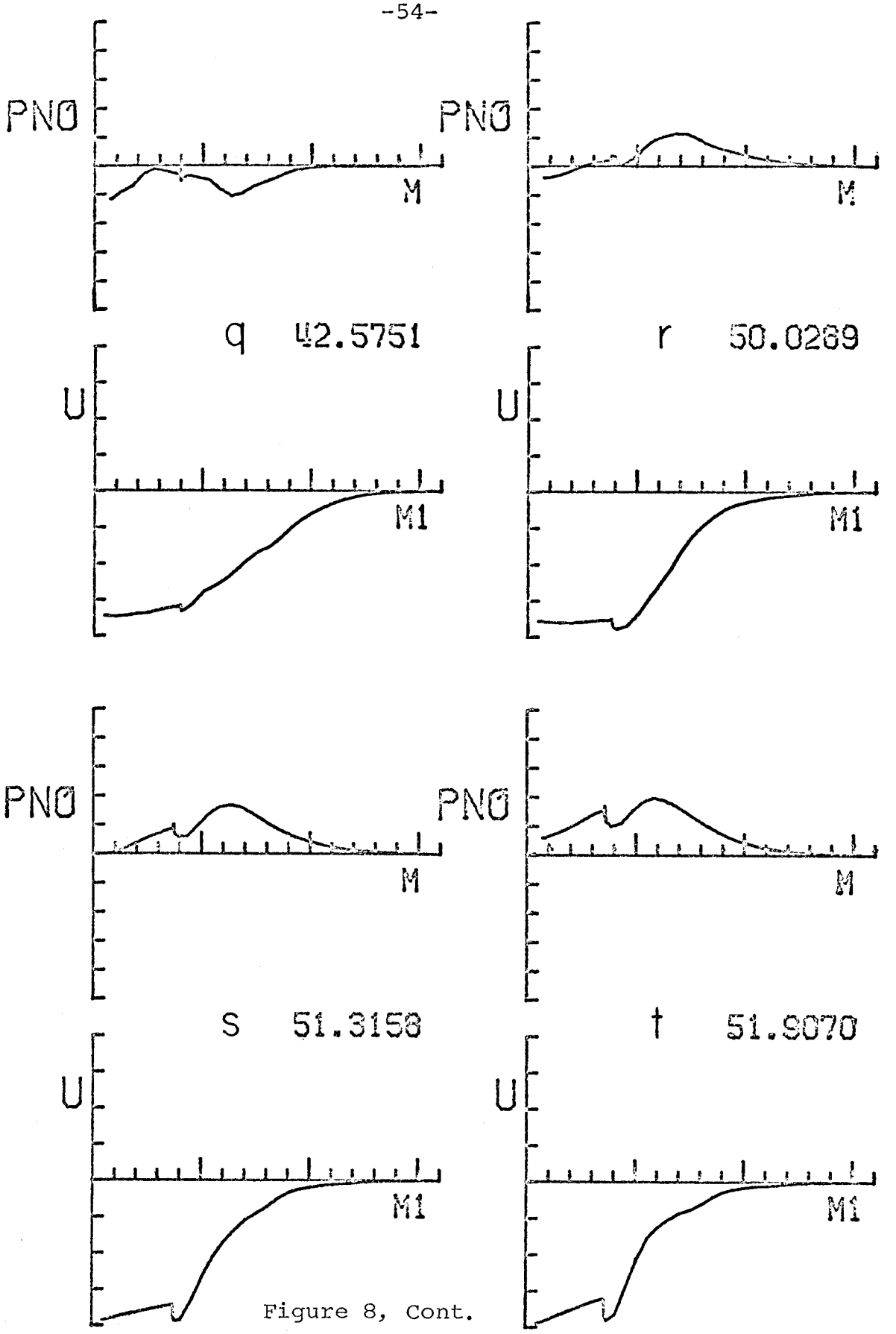

Figure 8, Cont.

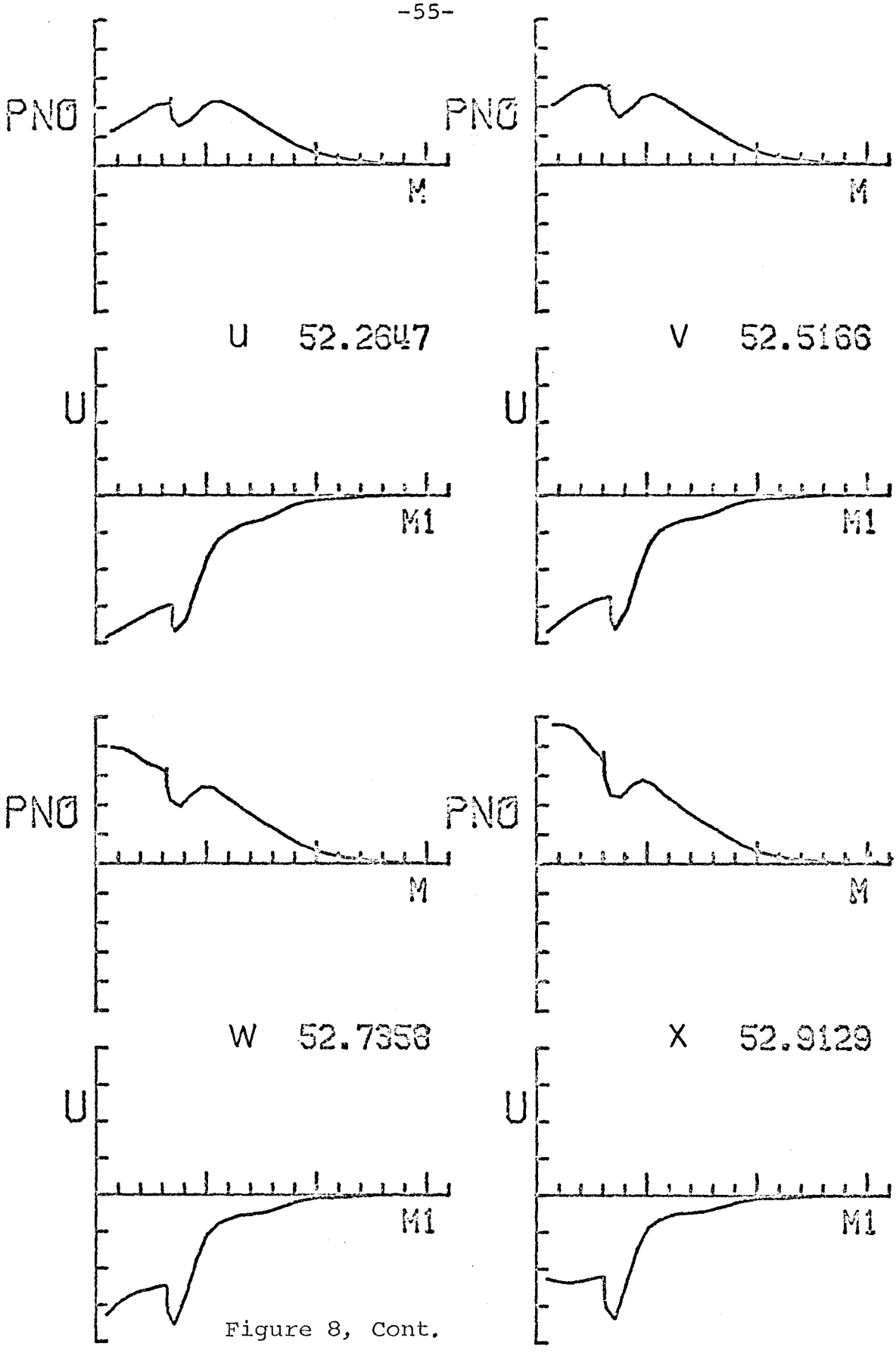

Figure 8, Cont.

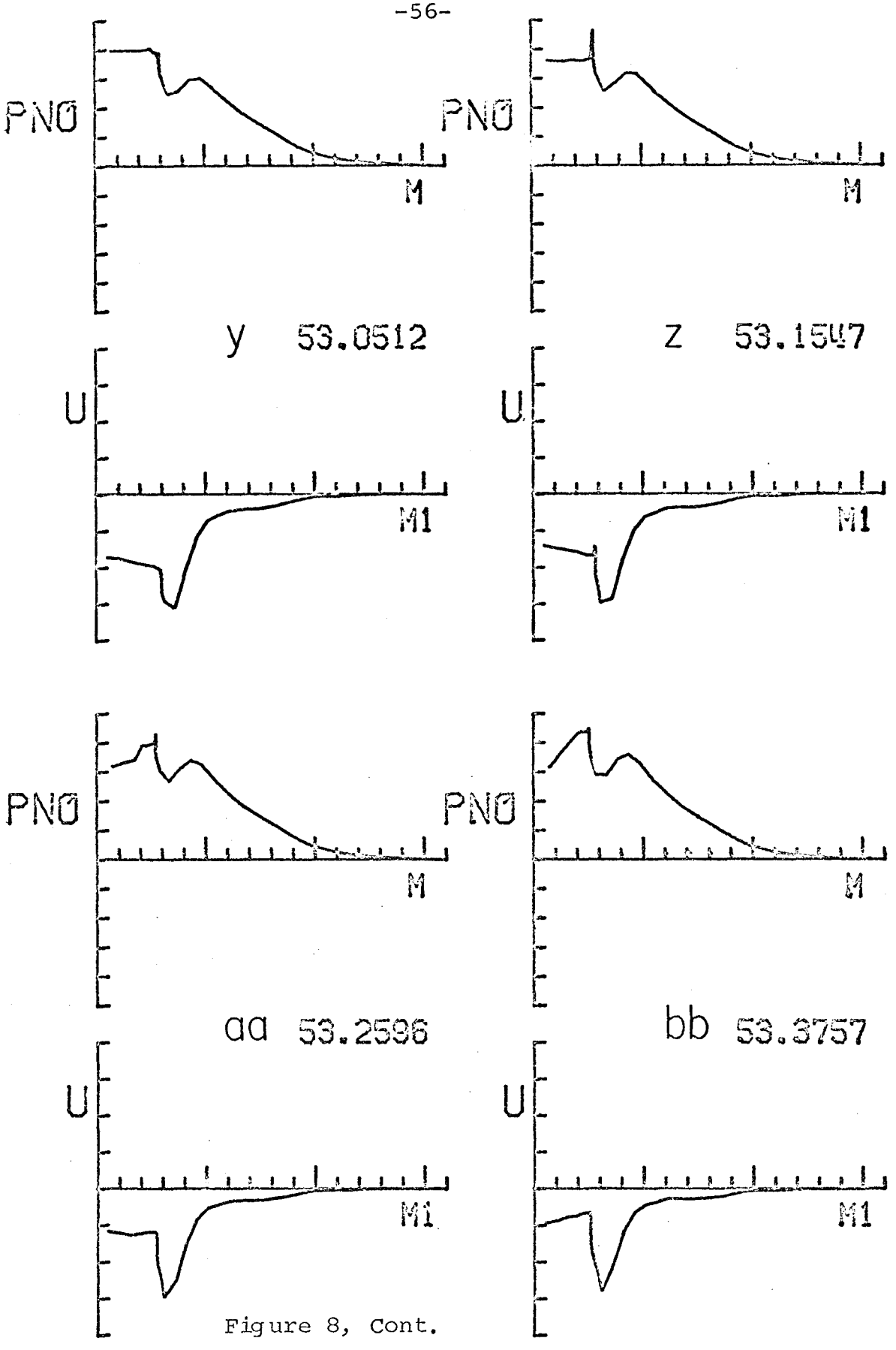

Figure 8, Cont.

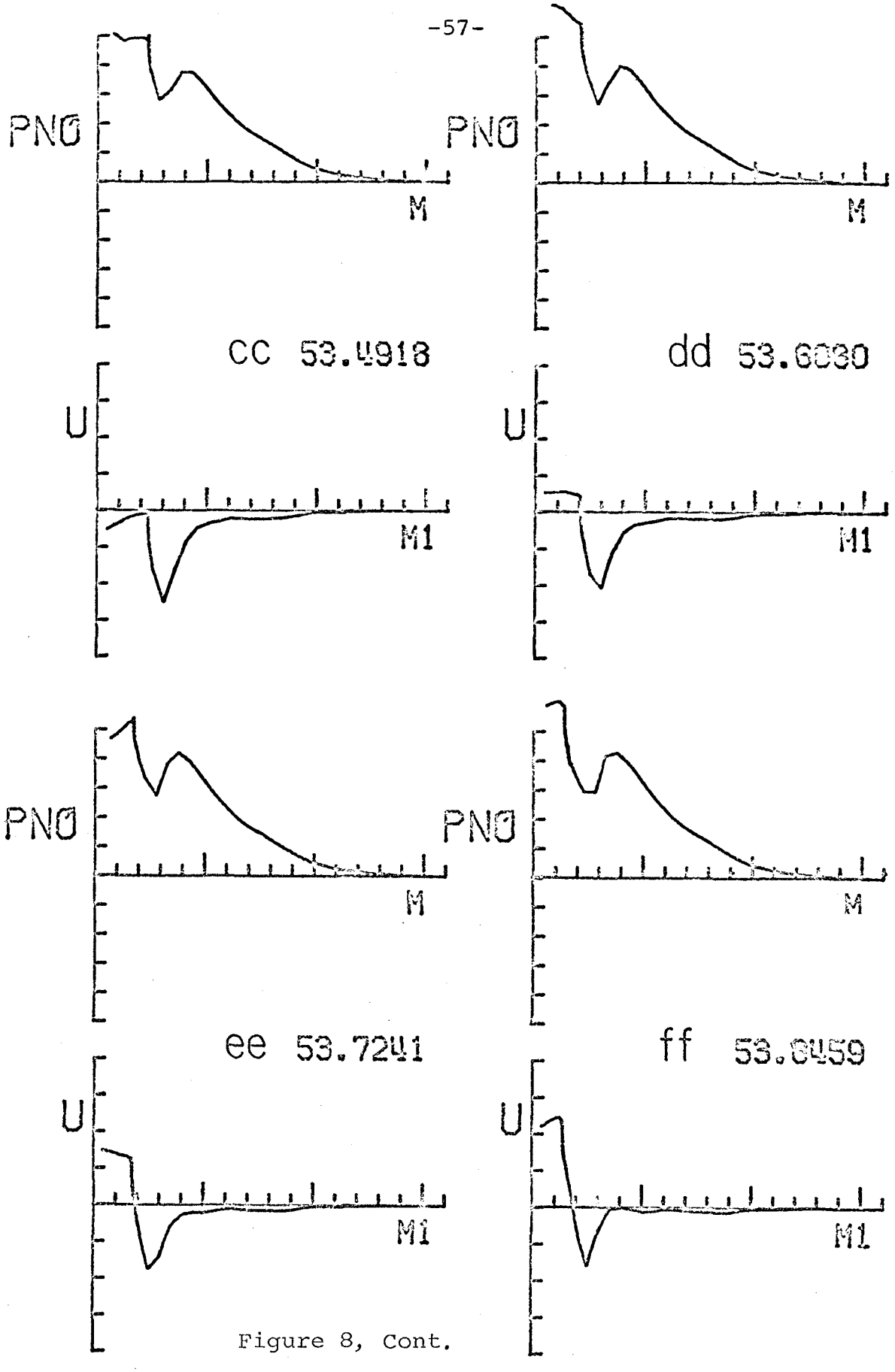

Figure 8, Cont.

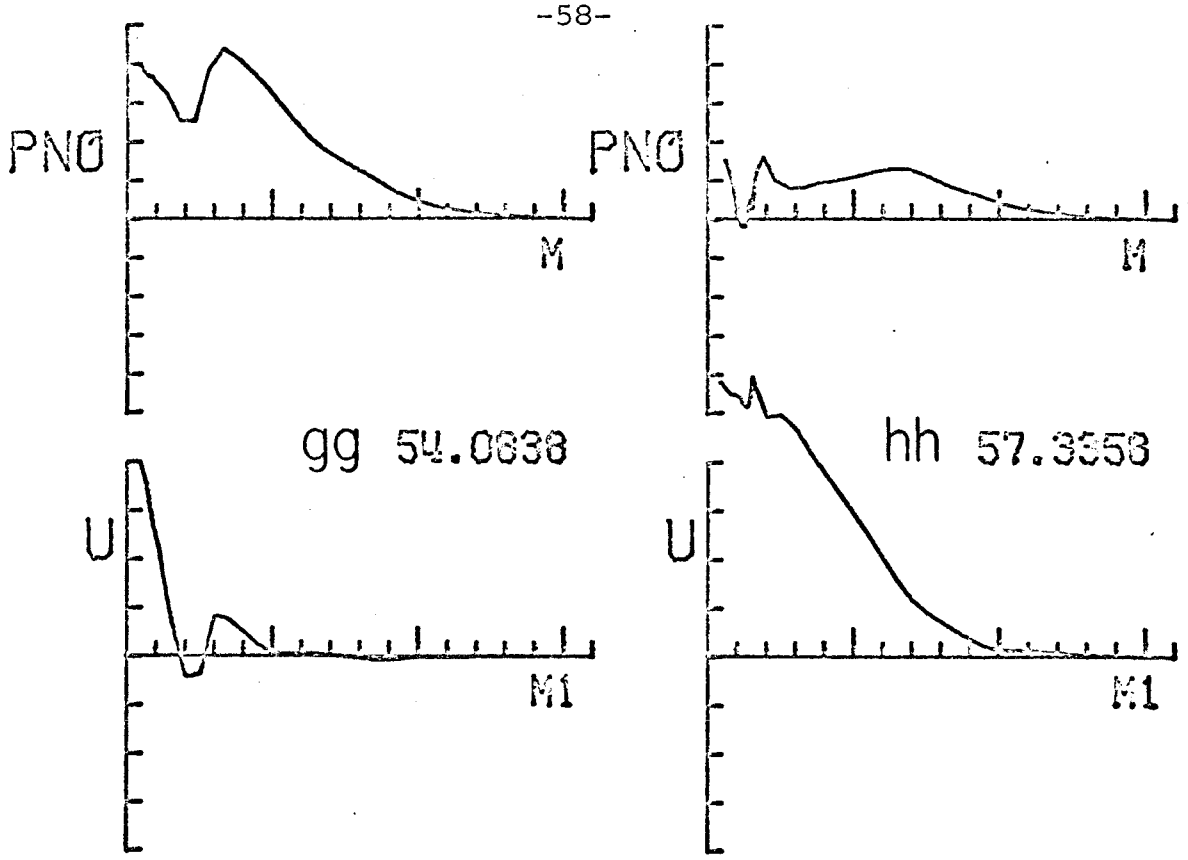

Figure 8, Continued

phenomena evident in the curves are the ionization zone effects, the H zone appearing as a discontinuity (ionization front) on the scale of these plots. A discussion of ionization fronts will follow this section, so for the present attention should be directed to the deeper region. In the curves for $t = 5.02$ we see the maximum of PNO at M1 = 6, which is in the He zone. It is also apparent that the bulk of the kinetic energy lies in or near the He zone. These are obviously the conditions which are favorable for making the He zone drive the pulsation.

The region below the He zone is quasi-adiabatic and as can be seen the amplitude drops rapidly through this region. This is where the linear adiabatic theory is applicable for determining the period and the amplitude distribution. To actually make this comparison the spatial difference equations in continuous time which were used before to derive the discrete energy law were linearized (adiabatically) to give a set of linear homogeneous equations for the pulsation amplitudes on each discrete sphere, with the square of the frequency appearing as the eigenvalue. The same boundary conditions which were used in the dynamical calculation were applied, suitably linearized, in this case. The result was the following system:

$$(A - \omega^2 I)\frac{\delta R}{R} = 0$$

in matrix notation, where $A = (A(I,J), I,J=2,N+1)$ is a tri-diagonal matrix, the elements of which are

$$A(I,I-1) = \frac{-4\pi R(I)}{DM2(I)} \left(\rho C_S(I-1)\right)^2 \frac{4\pi R^3(I-1)}{DM1(I-1)} \qquad I > 2$$

$$A(I,I) = \frac{4\pi R(I)}{DM2(I)} \left[\left(\rho C_S(I)\right)^2 \frac{4\pi R^3(I)}{DM1(I)} + \left(\rho C_S(I-1)\right)^2 \frac{4\pi R^3(I)}{DM1(I-1)} \right] - \frac{4G \cdot MO(I)}{R^3(I)}$$

$$A(I,I+1) = -\frac{4\pi R(I)}{DM2(I)} \left(\rho C_S(I)\right)^2 \frac{4\pi R^3(I+1)}{DM1(I)} \qquad I < N+1.$$

The first term in the bracket for A(I,I) is omitted for I=N+1. The off-diagonal elements of A are roughly $-(1/\Delta t)^2$ where Δt is the sound travel time across a shell. The diagonal elements are of the same order, but in addition have a gravity term which is about $0.4\omega^2$, and is one to two orders of magnitude less than the other terms. In the H zone Δt becomes very small and the elements become very large, making solving for the eigenvalues quite difficult. For this reason the approximation $\frac{\delta r}{r}$ = constant in the H zone had to be used.

The results for the periods of the fundamental and first harmonic are

$$P_o = 45.96, \quad P_1 = 33.75, \quad P_1/P_o = .734$$

which compare well with the period of the dynamical model

Table III

I	R	δR	U_{max}	$U_{max}/\delta r$
1	875.5	0	0	-
2	1153.9	3.42	.0412	$1.20.10^{-2}$
3	1391.8	10.79	.1191	1.10
4	1601.8	24.35	.3118	1.28
5	1791.1	46.93	.5816	1.24
6	1963.8	81.3	.9689	1.19
7	2122.7	131.2	1.400	1.07
8	2269.7	199.3	2.392	1.20
9	2406.1	289	3.556	1.23
10	2531.6	403	4.993	1.24
11	2645.1	537	6.733	1.25
12	2747.2	692	8.675	1.25
13	2839.6	866	10.61	1.23
14	2923.5	1061	12.35	1.16
15	2999.8	1278	14.67	1.15
16	3069.4	1510	17.56	1.16
17	3132.7	1757	20.65	1.18
18	3189.5	2022	24.02	1.19
19	3239.7	2313	27.70	1.20
20	3282.4	2600	31.01	1.19
21	3318.6	2821	33.79	1.20

I : mass sphere index
R : equilibrium radius, 10^3 km
δr : linear pulsation amplitude in radius (or velocity)
U_{max} : maximum velocity of the sphere in the transfer
$U_{max}/\delta r$: the ratio. It is constant in principle. model

(46.35) and the period ratio expected for this model according to the correlation observed by Christy (.75, Christy 1966a). Table III shows a comparison of the velocity amplitude δr derived by finding the eigenvectors of the linear system and the actual maximum velocities observed in the dynamical model at the same points. The ratio of the two is seen to be constant within a few percent for all the points interior to the He zone. The differences which do exist are probably due to the harmonic mixture which actually represents the non-linear pulsation in the linear region. The conclusion would seem to be that the period and the amplitude in the interior can be reliably found from this simple type of calculation.

3. Internal Dynamics II . The Hydrogen Zone and the Exterior

The events which occur above the hydrogen zone as seen in the first period of the calculation are summarized in Figure 9, which is a space time diagram. The ordinate is time, with P indicating the end of one period; the abscissa is the usual space variable $\ln(M-M_r)$.

The motion of the hydrogen and helium ionization zones and of the layer where τ is 10^{-2} is indicated, as are the equilibrium positions of the H and He zones. It is apparent that the motion of the hydrogen zone largely mimics the effective temperature variation (see Section d),

compression wave

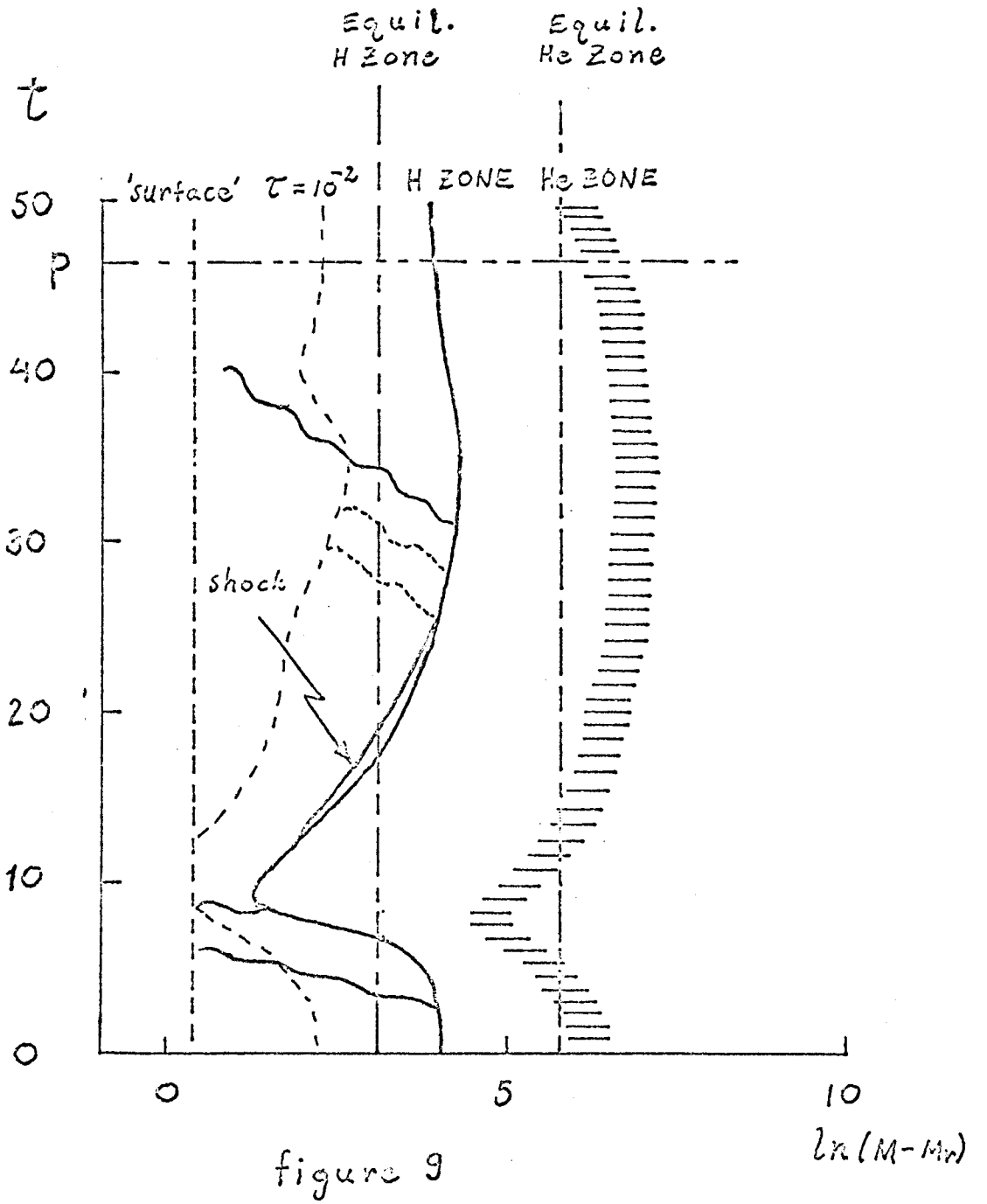

figure 9

while the helium zone follows more nearly the gravity, that is, pressure, variation.

The wavy lines indicate roughly the paths of the outgoing compression waves which occur above the H zone. Of course, the actual velocity field is very complex, and there must be inward and outward compression and rarefaction components in the motion, but the outward compression waves are the easiest to identify in the numerical calculations so only these are shown. The wave which lasts from $t = 3$ to 6 is the one associated with the pre-rise velocity bump, when it occurs. The wave near $t = 8$ is generated when the rarefaction behind the then almost stationary ionization front is filled in by outward motion from the higher pressure helium region (see Figure 8). The double line shown for the H zone from $t = 13$ to 25 represents the I-front, on the right, and the following shock (see Section c). After $t = 25$ the H zone region oscillates and generates several waves of which the strongest is shown from $t = 31$ to 40. This is the closest analogue in this cycle of the wave from 3 to 6 a period before.

The optical depth variation also follows the temperature variation; $\tau = 1$, if it were shown, would be almost coincident with the H zone. The $\tau = 10^{-2}$ curve shows in addition to the temperature dependence some effects of the waves on the outer layers. At $t = 40$ the optical

depths are increased due to the elevation of temperatures in the very thin layers produced by the wave shown at that time.

a. Ionization Fronts.

During most of the period the temperature gradient dlogT/dlogp has a maximum with depth exceeding 10, typically 20 or more, and this occurs in the H zone. This means that the transition from neutral (8000 degrees) to ionized (15000 degrees) takes place in only .10 of a scale height or less. Therefore the whole zone can be treated as a discontinuity, an ionization front or I-front.

Treating it as a discontinuity, then, the conservation laws yield the jump conditions (Courant and Friedrichs 1948, p.124; modified to account for the jump in flux):

$$\rho_0 v_0 = \rho_1 v_1 = \dot{m}$$

$$p_0 + \rho_0 v_0^2 = p_1 + \rho_1 v_1^2$$

$$4\pi r^2 \dot{m} \left[(e_1 + p_1/\rho_1 + v_1^2/2) - (e_0 + p_0/\rho_0 + v_0^2/2) \right] = L_1 - L_0$$

where $_0$ refers to the neutral side and $_1$ refers to the ionized side, and v is the material velocity with respect to the front. These jump conditions are valid as long as the front width is less than other lengths, such as a scale

height or the distance the front travels before its structure changes noticeably. Idealizing the equation of state we can put

$$e_1 = \frac{3}{2}\frac{p_1}{\rho_1} + \chi\,, \quad e_0 = \frac{3}{2}\frac{p_0}{\rho_0}$$

giving

$$\rho_1 v_1 = \rho_0 v_0$$

$$p_1 + \rho_1 v_1^2 = p_0 + \rho_0 v_0^2$$

$$p_1/\rho_1 = p_0/\rho_0 + \Delta$$

$$\Delta = \frac{2}{5}\left(\frac{L_1 - L_0}{4\pi r^2 \dot{m}} + \frac{v_0^2 - v_1^2}{2} - \chi\right).$$

If we choose the states o and 1 as having definite temperatures and molecular weights then

$$\frac{p_1}{\rho_1} = c_1^2\,, \quad \frac{p_0}{\rho_0} = c_0^2$$

and

$$L_1 - L_0 = 4\pi r^2 \dot{m}\left(\chi + \frac{5}{2}(c_1^2 - c_0^2) + \frac{1}{2}(v_1^2 - v_0^2)\right)$$

and

$$\rho_1 v_1 = \rho_0 v_0$$

$$\rho_1(v_1^2 + c_1^2) = \rho_0(v_0^2 + c_0^2)$$

so

$$\frac{1}{v_1}(v_1^2 + c_1^2) = \frac{1}{v_0}(v_0^2 + c_0^2)\,.$$

This equation or one similar to it has been extensively studied by Kahn (1954), who classifies the solutions as weak or strong and of R type or D type as follows:

R if $v_o \gtrsim v_r > c_o$

D if $v_o \lesssim v_d < c_o$

weak if $v_1 > c_1$ or $< c_1$ as $v_o > c_o$ or $< c_o$

strong if $v_1 < c_1$ or $> c_1$ as $v_o > c_o$ or $< c_o$.

If $v_d < v_o < v_r$ the conditions are referred to as M type, but cannot exist at a real I-front. For the present case

$$U_r = c_1 + \sqrt{c_1^2 - c_o^2} = 24 \text{ km/sec}$$

$$U_d = c_1 - \sqrt{c_1^2 - c_o^2} = 2 \text{ km/sec}$$

where $c_o = 7$ km/sec and $c_1 = 13$ km/sec.

The actual relations which obtain in each case are:

weak R or strong D

$$U_1 = \frac{U_o^2 + c_o^2}{2U_o} + \sqrt{\left(\frac{U_o^2 + c_o^2}{2U_o}\right)^2 - c_1^2}$$

$$\frac{\rho_1}{\rho_o} = \frac{U_o}{U_1} \quad , \quad \frac{p_1}{p_o} = \frac{U_o}{U_1}\frac{c_1^2}{c_o^2}$$

strong R or weak D

$$U_1 = \frac{U_o^2 + c_o^2}{2U_o} - \sqrt{\left(\frac{U_o^2 + c_o^2}{2U_o}\right)^2 - c_1^2}, \; p_1 \text{ and } \rho_1 \text{ as before.}$$

Two important limiting cases are a weak R front with $v_o \gg v_r$ and a weak D front with $v_o \ll v_d$. For the D front

$$U_o \ll U_d \text{ implies } \quad U_1 \doteq \frac{c_o^2}{2U_o}\left(\frac{1}{2}\frac{c_1^2}{(c_o^2/2U_o)^2}\right) = \frac{c_1^2}{c_o^2}U_o \,,$$

$$\text{and} \qquad \frac{\rho_1}{\rho_0} = \frac{C_0^2}{C_1^2} \quad , \quad \frac{P_0}{P_1} = 1 \ .$$

In other words, when the front propagates much more slowly than the sound speed the pressure is almost continuous across the front, and the equilibrium density ratio exists. For the R front

$$U_0 \gg U_r \longrightarrow \begin{aligned} U_1 &\doteq U_0 \\ \rho_1 &\doteq \rho_0 \\ \frac{P_1}{P_0} &\doteq \frac{C_1^2}{C_0^2} \ . \end{aligned}$$

In this case the front sweeps over the material too rapidly for the pressure to adjust, so the density is almost continuous, while there is a large pressure ratio.

For completeness the other two limiting cases are a very strong R front

$$U_0 \gg U_r \ , \qquad \begin{aligned} U_1 &\doteq \frac{U_0}{2}\left(\frac{1}{2}\,\frac{C_1^2}{(U_0/2)^2}\right) = \frac{C_1^2}{U_0} \\ \frac{\rho_1}{\rho_0} &= \left(\frac{U_0}{C_1}\right)^2 \\ \frac{P_1}{P_0} &= \left(\frac{U_0}{C_0}\right)^2 \ , \end{aligned}$$

and a very strong D front

$$U_0 \ll U_d \ , \qquad \begin{aligned} U_1 &\doteq \frac{C_0^2}{U_0} \\ \frac{\rho_1}{\rho_0} &\doteq \left(\frac{U_0}{C_0}\right)^2 \\ \frac{P_1}{P_0} &= \frac{C_1^2}{C_0^2}\left(\frac{U_0}{C_0}\right)^2 . \end{aligned}$$

In Kahn's very complete analysis he shows that D-fronts other than the critical one are likely to be unstable, in the sense that they cause rarefactions to proceed them into the neutral material (he considers only the case of a front propagating into the neutral gas, backed by a vacuum) with the result that v_o increases to make the front critical. If the conditions in the neutral gas are such that $v_o > v_d$ (M-type) a compression wave or shock will travel ahead, lowering v_o to the critical value. His analysis is probably no longer valid if the ionized region is not bounded by a vacuum. In the more general case it seems to be possible to have D-fronts traveling at less than the critical speed.

Figure 10 shows all the possible solutions, plotting the neutral Mach number v_o/c_o versus the compression ratio ρ_1/ρ_o on log-log scales. The two brandhes are the D and R type fronts, and the maximum and minimum of these, respectively, give the critical cases. The dashed vertical line represents $p_1 = p_o$. For the case mentioned above, $c_o = 7$, $c_1 = 13$, the critical conditions are:

R critical $\quad v_o/c_o = 3.4\,, \quad \rho_1/\rho_o = 1.83$

D critical $\quad v_o/c_o = .29\,, \quad \rho_1/\rho_o = 1/6.6\,.$

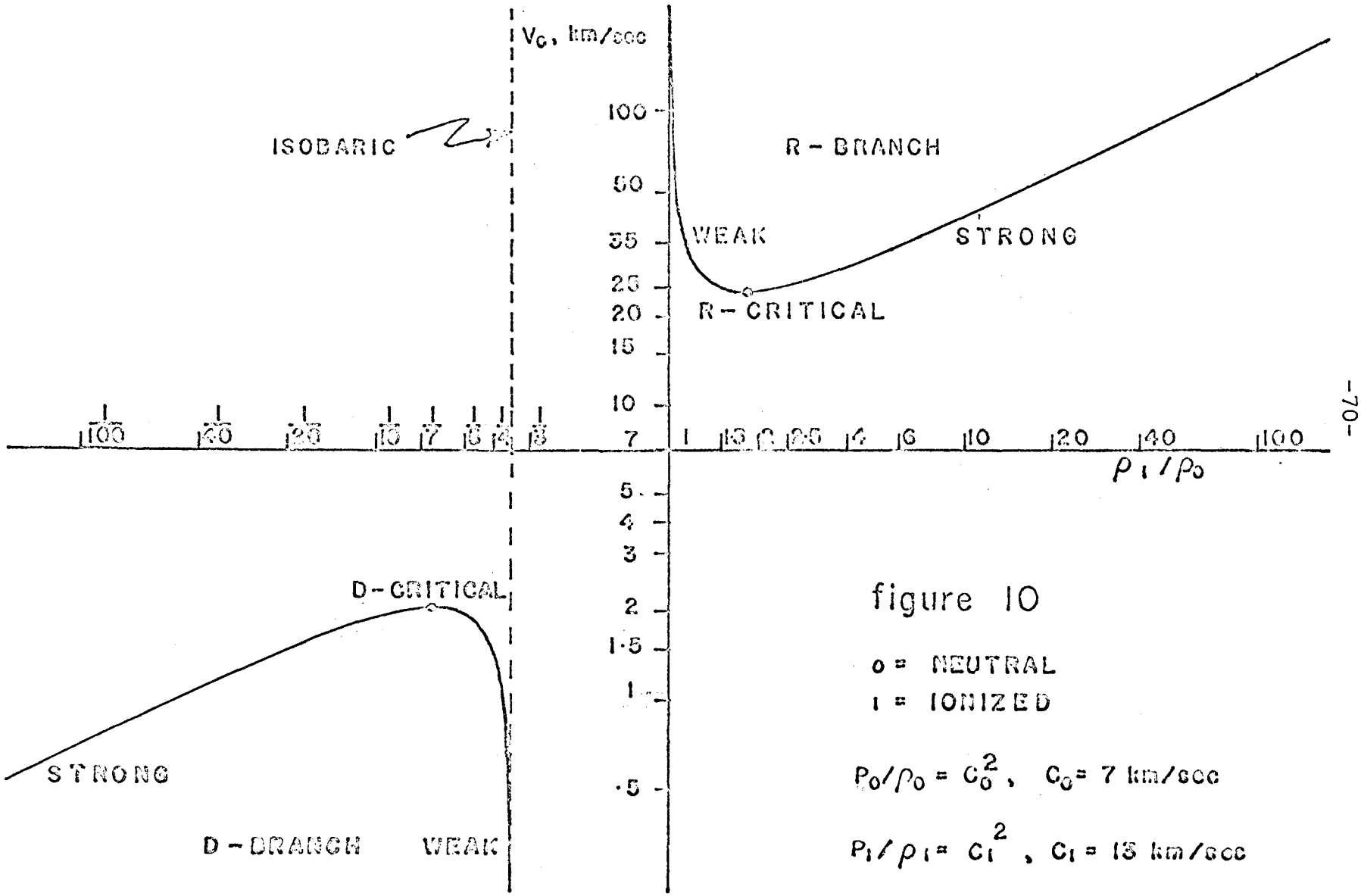

figure 10

o = NEUTRAL

1 = IONIZED

$P_0/\rho_0 = C_0^2$, C_0 = 7 km/sec

$P_1/\rho_1 = C_1^2$, C_1 = 13 km/sec

For comparison the isobaric density ratio is

$$\text{for } p_1 = p_0 \ , \quad \rho_1/\rho_0 = c_0^2/c_1^2 = 1/3.6 \ .$$

There is an analogous discussion in Courant and Friedrichs for chemical reactions in gasses. In their notation an R-front is a detonation and a D-front is a deflagration, weak or strong as defined here. The critical cases are called Chapman-Jouguet processes, and a theorem is proved forbidding weak detonations and strong deflagrations. The analysis is similar to that used to forbid rarefaction shocks, which these fronts in fact resemble. This is not valid for the case in which energy transfer exists, however. In fact, weak R-fronts and strong D-fronts are of definite interest in the application to pulsating stars.

b. The Rising Branch.

The compression phase of pulsation is also the phase when the hydrogen zone moves outward through the atmosphere. At the end of the expansion phase, when the luminosity curve and the velocity curve are near their minima, the pressures in the atmosphere are depressed from the static values and the effective temperature is also low with the consequence that the hydrogen zone is very deep in the envelope, since the overlying mass per unit area varies approximately as

$$\frac{M - M_r}{4\pi r^2} \sim g_e^{-1/3} T_e^{-8} .$$

At this point compression begins to raise the pressures. A basic fact of RR Lyrae stellar models is that the helium zone contains several times as much mass as the layers above it, so that from the hydrogen zone's viewpoint it is a piston pushing the layers above it up and then letting them fall. At this time it begins accelerating them upward. When the material between the H and He zones is compressed it allows the luminosity to increase, causing the H zone to absorb more energy than it emits. This differential increases as compression continues, so that for example in the model at $t = 7.47$, when the radius is near minimum, the luminosity differential is

$$\Delta L = 2.0 \cdot 10^4 \text{ units},$$

30 percent greater than the mean luminosity. As the energy equation written above shows, the H zone moves outward as the energy is absorbed in ionizing the material. The rate at which it moves is given by

$$\frac{dM_r}{dt} = 4\pi r^2 \rho_0 v_0 = \frac{\Delta L}{\chi + \frac{5}{2}(c_1^2 - c_0^2) + \frac{1}{2}(v_1^2 - v_0^2)}$$

$$\doteq \frac{\Delta L}{\chi}$$

where $\chi \doteq 1/2 \ (50 \text{ km/sec})^2$ dominates the other terms. This value of $\rho_0 v_0$ is rather independent of conditions in the H zone itself, being fixed mostly by the

layers below.

As the outer layers and the H zone fall and are compressed both ρ_o and ΔL, hence $\rho_o U_o$, tend to increase. There are then two possibilities. The first is that ρ_o increases rapidly enough to prevent U_o from exceeding U_d, so the I-front is always D-type and in fact weak D type is what is expected, since as the compression proceeds in the regular way there is no reason for a large ρ_o/ρ_1 to develop. After maximum compression the ΔL across the front diminishes as the pressures fall in the layers below the front at the same time as the emergent luminosity rises due to the thinness of the layer above the front. Consequently the front ceases its outward course and as the contained energy escapes it begins to progress inward again.

What has just been described is the sequence of events during the first compression phase in the transfer model. Examining the U, PNO profiles in Figure 8 of any of the models from 5.02 to 7.47 reveals the same features: a relative PNO maximum in the He zone, a PNO minimum in the intermediate region, a velocity and PNO discontinuity at the H zone and quasi-equilibrium conditions in the atmosphere above. Examining $t = 7.47$ in more detail, we find that the I-front velocity is

$$U_{\text{front}} = 2.6 \text{ km/sec.}$$

so that

$$v_o = 1.6 \text{ km/sec} \quad , \quad v_1 = 6.6 \text{ km/sec}$$

$$\rho_o/\rho_1 = 4.1 \quad , \quad p_o/p_1 = 1.2 \quad .$$

The I-front is followed closely by a rarefaction wave which lowers U and PNO to the values seen in the plot on the ionized edge of the H zone. We see that indeed that $U_o < 2.0 = U_d$. The conditions that are observed here do actually refer to a weak D-front.

At $t = 8.12$ we see that the emergent luminosity has risen and the front has slowed. At this time the pressure minimum between the H and He zones is disappearing as a compression wave makes its way outward from the He zone. After $T = 8.54$ until just before maximum light the H zone is fairly static. The compression wave just referred to appears as a maximum in the gravity curve at $t = 8.6$ and simultaneously as a notch in the M_{bol} curve.

The other possibility is caused by ΔL increasing more rapidly than p_o , causing v_o to exceed v_d . This type of M-front condition is not possible and the result is a shock in the layers above the front, deriving its energy from the flux excess. The pressure in the outer layer then exceeds the value necessary to

reverse the downward velocity in the length of time the He zone requires. The effect is that the material above the front accelerates outward faster than the material below it. The rarefaction produced below the front causes the luminosity there to be even larger, aggravating the situation. Because the density in the neutral region has been increased the front now propagates at or below the critical speed v_d. These conditions last as long as the front moves outward until the compression is relieved and the low pressure region radiates in a brief flash the energy which has been contained there. Now the very strong rarefaction which has followed the front sweeps through the visible atmosphere and the velocity of the photosphere drops. But following the rarefaction is a strong shock running from the He zone into the low pressure region. When this reaches the photosphere the velocity curve attains its maximum and the expansion phase begins.

As it happens, these are the events which take place on the second rise. The pressure at $t = 51$ in the layer above the H zone is too low to prevent the conditions at the front from being M-type. The shock in the outer region is visible in the gravity and luminosity curves near $t = 53$ and very nicely as it is just forming in the U and PNO profiles at $t = 53.1547$.

Following this time the U, PNO profiles show the very strong rarefaction accompanying the I-front[1]. The luminosity flash happens near $t = 54.0$ and soon after that the rarefaction reaches the surface. At $t = 54.53$ the major shock is traveling into the low pressure region and reaches the photosphere at 55.2. After this time the atmosphere is in such a disturbed state that computation was discontinued at 57.34.

Needless to say, the shock and the luminosity flash are very wasteful of pulsation energy. Whenever strong shocks have occurred during the process of relaxing a model they have represented only transitory reactions to changes of the conditions, and have not persisted in the relaxed state, at least in this type of model. This is what would be expected also in this case were it possible to continue the calculation at some length. The model would adjust itself in order to make the pressure at the beginning of compression high enough to prevent a strong D-front from forming.

c. The Descending Branch.

At maximum light T_e is, naturally, rather large; therefore since ∇_{max} is small at that time it is not correct to speak of an ionization front until

[1] A weak D-front blended with a rarefaction shock is in fact just a strong D-front. Except for some spatial separation of these components, that appears to be what existed on the second rise.

T_e has decreased somewhat. By that time, say one third of the way down the descending branch, the front is already quite a bit deeper than it was just before maximum light. And at that time the emergent flux may exceed the flux into the front from below by the whole mean luminosity of the star. The front must be traveling in through the atmospheric material at a rate comparable to that at which it went outward before. An important difference, however, is that the pressure is very much less than what it was at that time. It is so much less, in fact, that v_o exceeds the critical speed of an R-front, v_r = 24 km/sec. Under these conditions a weak R-front is expected, with $\rho_1 = \rho_o$, $v_1 = v_o$ but $p_1/p_o = c_1^2/c_o^2 = 3.6$. Thus a low pressure region is created in the neutral region adjoining the front. A region of such low pressure cannot extend all the way to the surface so a shock runs into it from the higher pressure surface region. Since the weak R-front moves supersonically relative to the neutral material (as well as relative to the ionized material) the shock is not able to overtake the front until the pressure in the atmosphere increases or the luminosity differential decreases, slowing the front and allowing the shock to catch up.

In the model the weak R-front becomes evident at $t = 13$. At $t = 17$ to 19 the shock which follows it is

actually located in the visible part of the atmosphere, hence the fluctuations in the velocity and gravity curves; it is always located not far from optical depth unity. A possible explanation for this is the balance between the work done in compressing the material passing through the shock and the radiation losses: if the optical depth were greater the temperature would be greater and the losses larger, but if the optical depth were less the loss would be much less due to the finite optical thickness.

The best illustration of the behavior of the atmosphere during this period is in the U, PNO curves for 20.87. The low pressure region is bounded below by the I-front, which trails inward, and above by the very sharp shock discontinuity. The velocity jump across the shock is 18 km/sec and the pressure ratio is 6.7:1. The velocity jump across the I-front is about 9 km/sec. More exactly,

$$v_o = -24 \text{ km/sec}, \quad v_1 = -15 \text{ km/sec}, \rho_1/\rho_o = 1.6.$$

We see that this front is in fact roughly R-critical. These figures are quite approximate since the high T boundary of the front is not too well defined.

Not long after, at $t = 25$, the shock begins to overtake the front which its slowing its inward progress. By 26.5 the shock has begun to reflect from the higher

pressure material below the front. At 29.5 this reflection is very apparent. During this period a series of waves are generated in the vicinity of the H zone which cause the oscillations seen in the velocity and gravity curves. The reflected shock requires until t = 40 to reach the surface. It can be seen in a well developed state at 38.16. The profiles at 42.58, 50.05, and 51.32 show the result of the reflected shock on the atmosphere just before the next compression begins: a rarefaction has been produced at the surface. This is the explanation of why the pressures are depressed compared to the same phase one period earlier.

To elaborate somewhat this point, let's compare what occurred here with what occurred in the diffusion model with its lack of H zone resultion. In that model the low pressure region adjacent to the H zone was visible at times, as a single mass shell with a low pressure, but at other times it was not apparent, due to the location of the H zone with respect to the mass shells. This variation is obvious as the peaks in the gravity curve. When the H zone slowed its inward progress not very much happened, since no shell had a very low pressure at that time, and since the zones were thick enough to prevent a rapid response. As a result there was no reflected compression wave, only a small bump in the velocity curve. The pressure in the atmosphere remained low for quite a bit longer than

in the transfer model before a compression wave raised it just in time for the rising branch to begin. Obviously this was the accomodation of the relaxed diffusion model to the strong D-front problem. But the greater resolution in the H zone in the transfer model caused these phenomena to occur in a different way, requiring further relaxation.

The implication of all this is that bumps on the descending branch in a relaxed model or a real star may be intimately related to the motion of the ionization front, both inward and outward.

d. Luminosity Modulation by Gravity.

An effect of some interest which only became obvious when the fine mesh was used in the H zone is the modulation of the emergent luminosity by variations in the surface gravity. This effect has obvious consequences for the interpretation of small fluctuations in the light variation of real variables. The nature of the effect is that if the material overlying the H zone is compressed, the emergent luminosity drops, and remains low as long as the compression continues or until the contained flux can work its way through the H zone. Alternatively the gravity may decrease, and the luminosity rises and remains high until the gravity increases or the available energy is exhausted.

The explanation of this effect is found in the processes determining the temperature distribution in the

neutral layer. We can find an approximate solution in the neutral layer as follows:

put

$$\frac{dp}{d\tau} = \frac{g}{\chi}$$

with

$$\chi = \chi_0 p^{1/2} T^n,$$

which is appropriate for H^- dominated opacity with the electrons supplied by ionization of hydrogen,

and $$T^4 = \frac{1}{2} T_e^4 \left(1 + \frac{3}{2}\tau\right)$$

so $$p^{1/2} dp = \frac{g}{\chi_0} \frac{1}{\left(\frac{1}{2} T_e^4\right)^{n/4}} \frac{d\tau}{\left(1+\frac{3}{2}\tau\right)^{n/4}}$$

so $$\frac{2}{3} p^{3/2} = \frac{g}{\chi_0 \left(\frac{1}{2} T_e^4\right)^{n/4}} \cdot \frac{2}{3} \frac{4}{n-4} \left[1 - \frac{1}{\left(1+\frac{3}{2}\tau\right)^{\frac{n}{4}-1}}\right].$$

We see that as $\tau \to \infty$ p approaches a limit, which represents the pressure in the H zone. That is

$$p_H = \left[\frac{4}{n-4} \frac{g}{\chi_0 \left(\frac{1}{2} T_e^4\right)^{n/4}}\right]^{2/3}.$$

Taking n to be a constant, typically 12, we have

$$p_H \sim g^{2/3} T_e^{-8}$$

so the overlying mass per unit area is

$$m_H \sim g^{-1/3} T_e^{-8}.$$

Now suppose this region is compressed. Due to its very large heat capacity the H zone itself remains at the same mass level. The neutral region very quickly reaches radiative equilibrium, however (neglecting the very optically thin part). Therefore, since m_H is the same and g is greater, T_e must decrease, as given by

$$T_e \sim g^{-0.04}.$$

The most obvious example of this is the compression phase as a whole. As the gravity rises when compression begins, the luminosity drops, as we expect. It remains down for a while (producing the depression from t = 2 to 7) and then slowly rises as the flux from below reaches a maximum and the zone moves rapidly out through the atmosphere. When the gravity drops after minimum radius the luminosity shoots up to the maximum (the same effect in the opposite direction). The luminosity drops again only when the energy excess in the interior is depleted.

Superimposed on this is another example, the notch in the luminosity at 3/4 maximum caused by the gravity peak associated with the compression wave rising from the He zone. There are many other, less significant, examples to be found and also the violent ones which occurred on the second rise.

4. Internal Dynamics III. Driving Energy

The energy integral of the equations governing the star is

$$\frac{\partial}{\partial t}\int_0^M \left(\frac{u^2}{2} - \frac{GM_r}{r}\right) dM_r = \int_0^M p\frac{\partial V}{\partial t} dM_r ,$$

which implies that when the motion is periodic

$$\oint \frac{\partial}{\partial t}\int_0^M \left(\frac{u^2}{2} - \frac{GM_r}{r}\right) dM_r \, dt = 0 = \int_0^M dM_r \oint p dV = \int_0^M dM_r \oint T d\mathcal{S} .$$

The amount of energy any shell adds to the pulsation is

$$DM1 \oint p dV = DM1 \oint T d\mathcal{S} .$$

For the model investigated here, 5gF, Christy shows the run of this quantity with shell number (1966a, Figure 21). There are slight modifications to the numbers due to the inclusion of radiation pressure and a somewhat larger amplitude in the more recent model which was used in this calculation, but the curve is essentially the same. The minimum (maximum damping) is in the shell near 75,000 degrees, and the two maxima are at 50,000 degrees, in the He zone, and at a shell near 10,000 degrees, in the H zone.

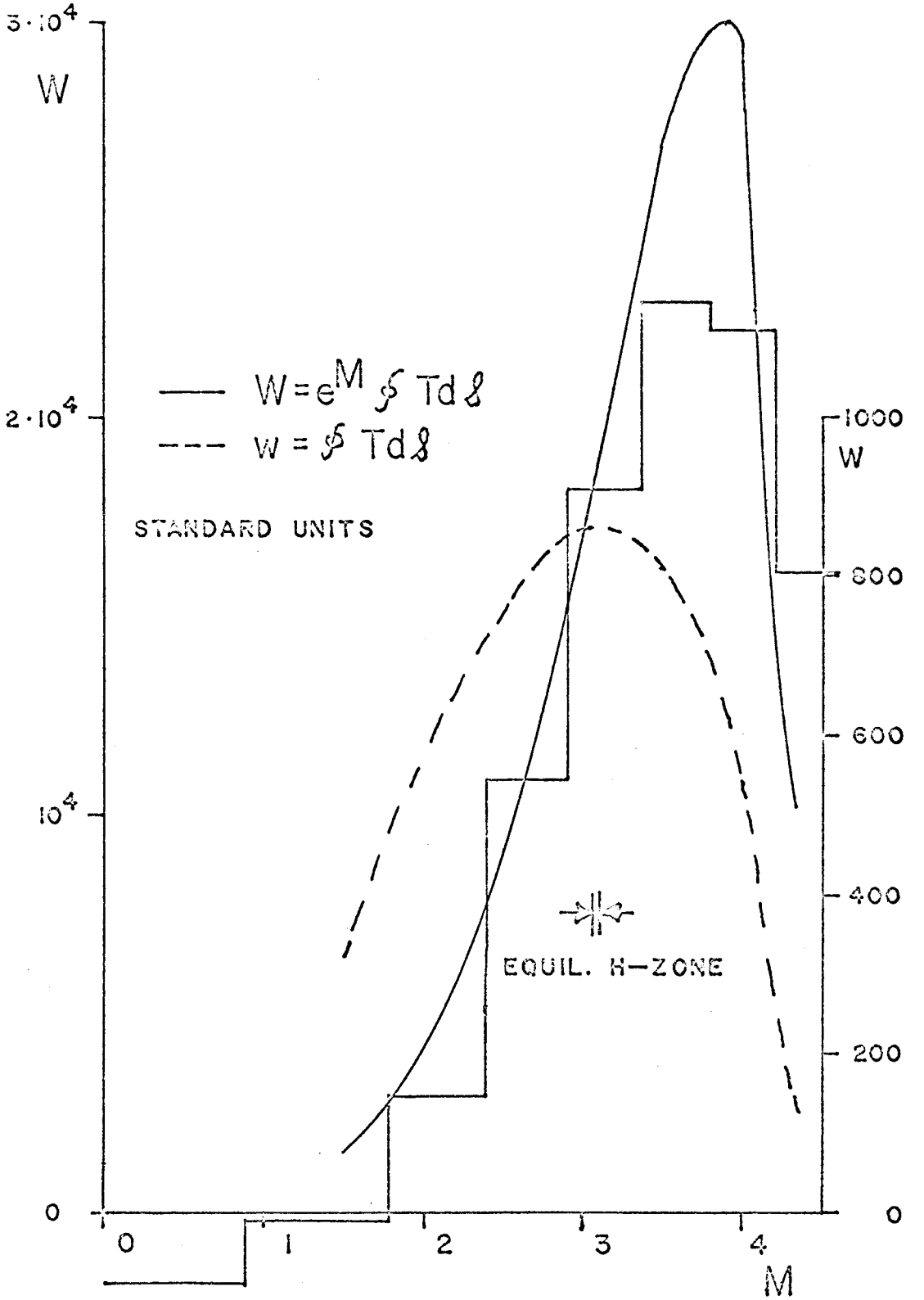

Figure 11. The distribution of hydrogen zone work production

a. The Damping Region and the Helium Zone.

It was not the purpose of this calculation to investigate the region beneath the H zone, and in fact the resolution used here for that region is about 30 percent poorer than that which Christy employed. As a consequence his figures for the damping and the excitation in that region are to be preferred.

To see the degree to which the results differ examine Figure 12, showing a temperature-entropy diagram for one cycle of each calculation for the same mass layer, M = 6.33, located at the He maximum. The entropy plotted for Christy's model is calculated from his temperature and pressure with the equation of state used for the present models. The curves are quite similar, although the enclosed area is slightly different. The area for the present calculation is

$$\oint T\,d\mathcal{S} = 61.1 \text{ (km/sec)}^2$$

while for Christy's it is

$$\oint T\,d\mathcal{S} = 66.5 \text{ (km/sec)}^2$$

or

$$\oint p\,dV = 60.5 \text{ (km/sec)}^2 \quad .$$

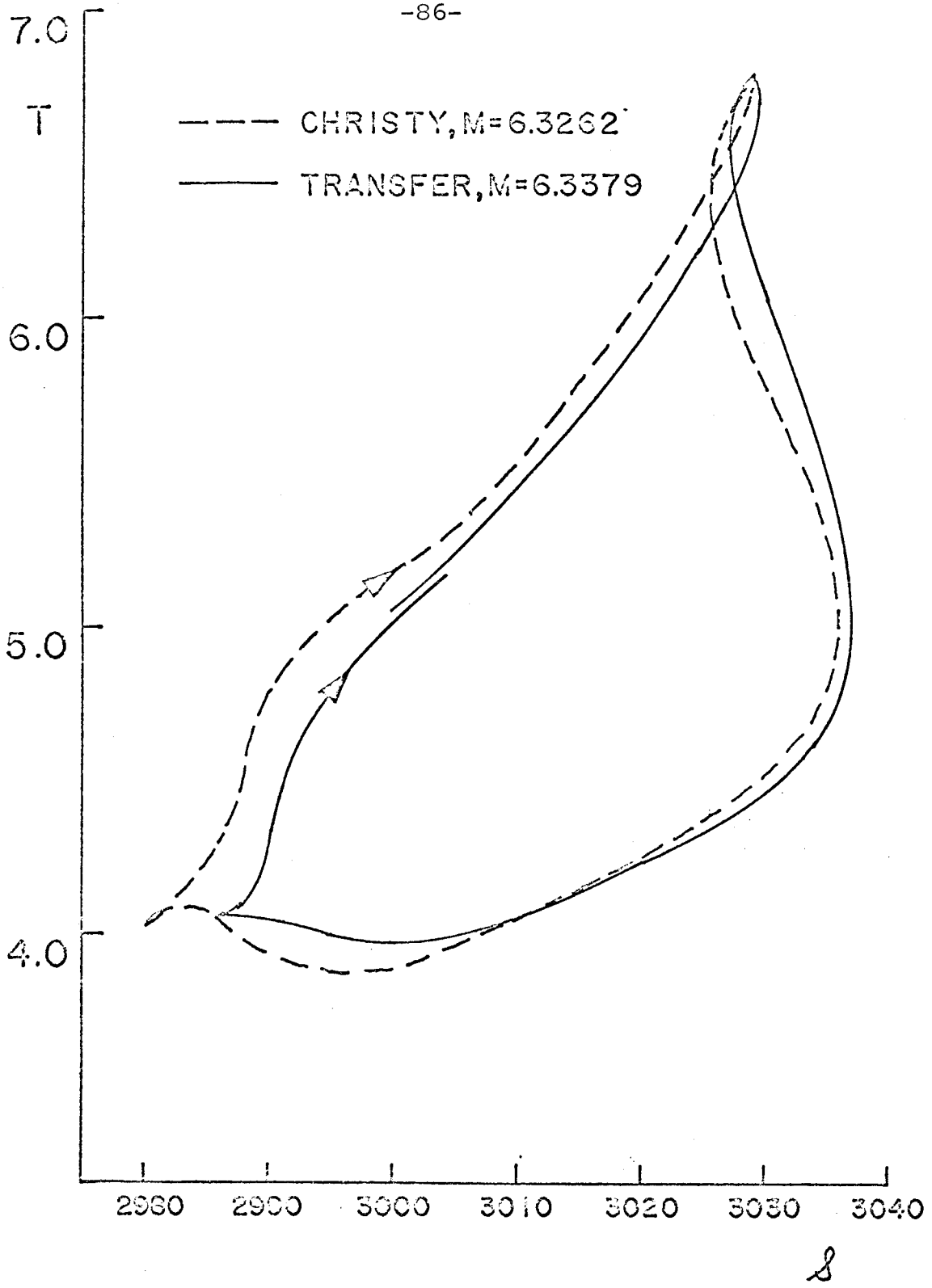

Figure 12. Temperature-entropy loops for corresponding mass elements (in the helium zone) in Christy's model and the transfer model

The discrepancy between $\oint T dS$ and $\oint p dV$ for Christy's model is indicative of the equation of state differences which exist between the two calculations.

The following figure, Figure 13, is a similar plot for a shell located at the damping maximum. In comparison with the previous figure some differences are obvious. The entropy amplitude is 8 instead of 50 (as for the He zone) due to the tendency toward adiabacy with depth, and the curve is more elliptical as non-linearities diminish. Most apparent of all, the loop is counter-clockwise rather than clockwise, indicating damping. In this case the agreement between the two calculations is poorer, although at least some of the disagreement might be due to the different thermodynamic functions. The figures for the areas are

$$\oint T dS = -13.5 \ (\text{km/sec})^2 \quad \text{present}$$
$$\oint T dS = -15.6 \ (\text{km/sec})^2 \quad \text{Christy}$$
$$\oint p dV = -17.2 \ (\text{km/sec})^2 \quad \text{Christy.}$$

Another explanation for the difference may be the coarser mass division and the difference of the inner boundary radius, which cause the distribution of amplitude to be somewhat different. A difference of a few percent in the energy production itself represents only of the order of a tenth of a percent of the kinetic energy per

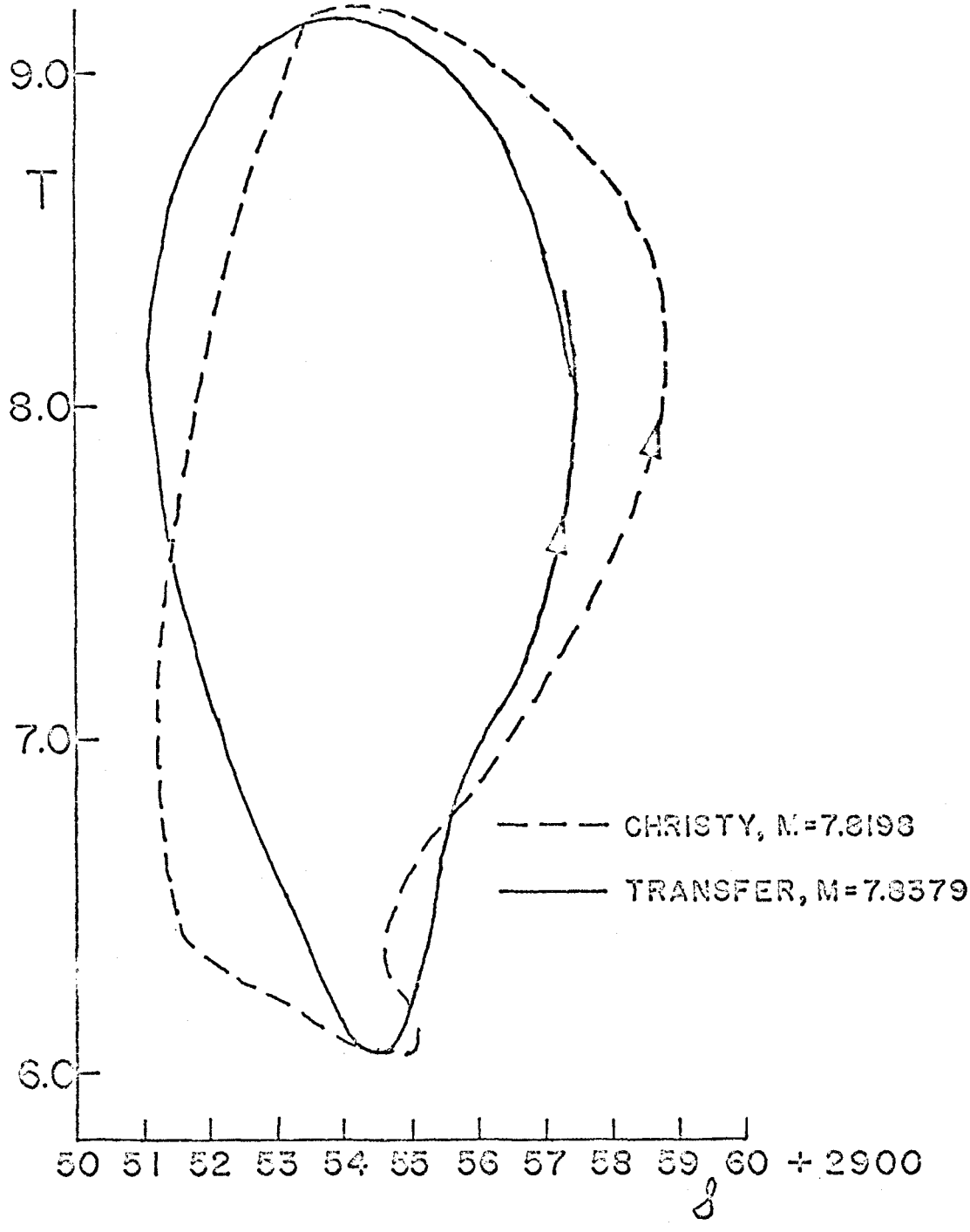

Figure 13. Temperature-entropy loop comparison for a mass element in the damping region

period. Such an error is not likely to affect the pulsation in the exterior region during the one period or so calculated here.

b. Work Production in the Hydrogen Zone.

The hydrogen zone is of more interest in the present calculations since the method used to treat it was more detailed and presumably more accurate than in the earlier work. Figure 14 shows as in the other two cases a comparison of the T-$\mathcal{S}$ loops of this calculation with Christy's model for a shell at the same mass layer. The agreement is similar to that obtained for the helium zone. The values for the work integral obtained variously are

$$\oint T d\mathcal{S} = 862 \text{ (km/sec)}^2 \text{ present}$$
$$\oint T d\mathcal{S} = 830 \text{ (km/sec)}^2 \text{ Christy}$$
$$\oint p dV = 784 \text{ (km/sec)}^2 \text{ Christy.}$$

Here also the agreement is very satisfactory. We can conclude from this that it is quite unlikely that Christy's calculations of work production in the hydrogen zone are very much in error, at least due to lack of resolution in mass. The error expected from this source is likely to be less than the contribution to work production from the shells at the edges of the region covered by the H zone and which therefore do not pass through the whole ionization loop.

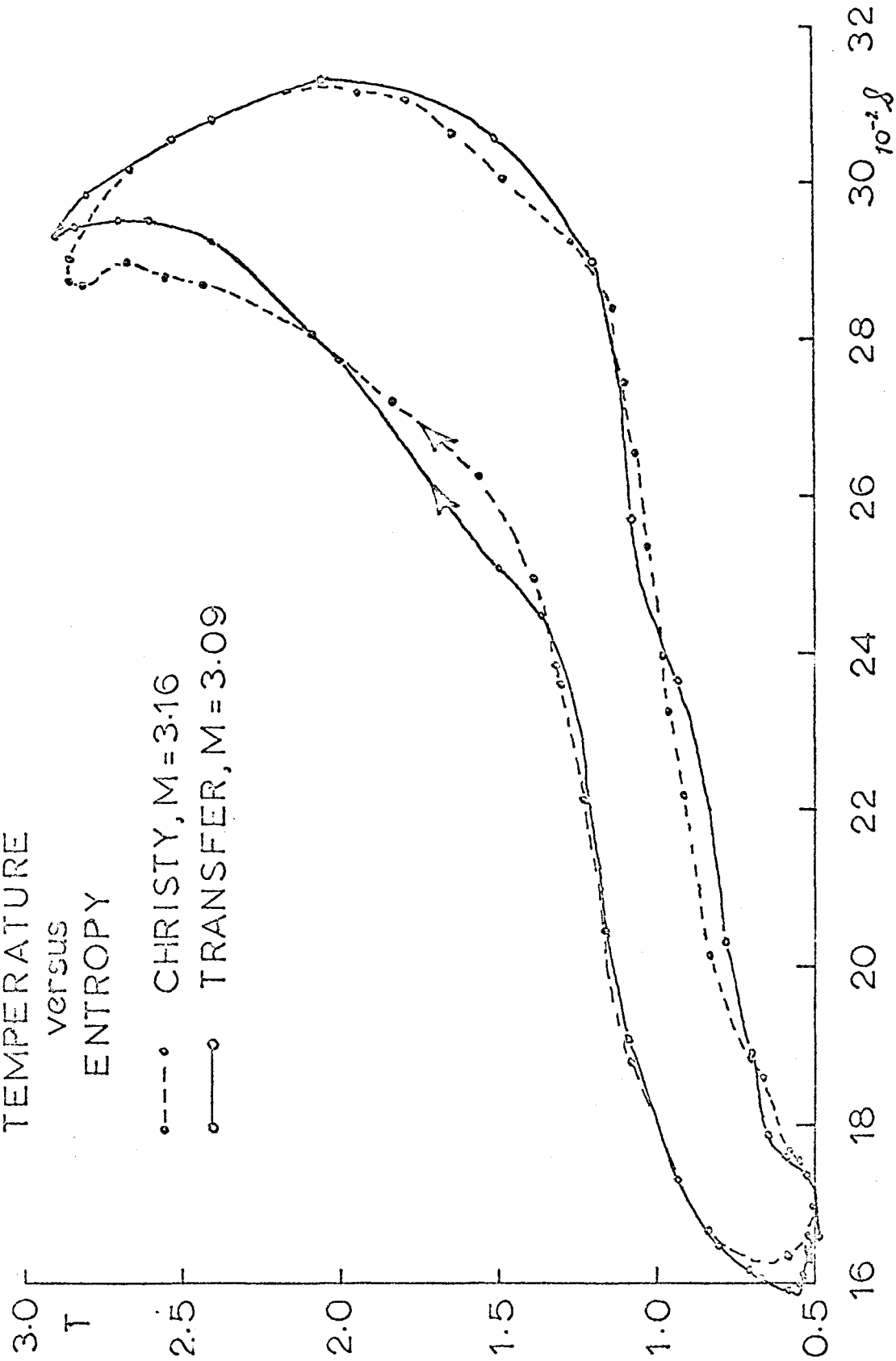
figure 14
TEMPERATURE
versus
ENTROPY
CHRISTY, M=3.16
TRANSFER, M=3.09
T
3.0
2.5
2.0
1.5
1.0
0.5
16
18
20
22
24
26
28
30
32
$10^{-4}\,s$

In order to determine the total work production in the H zone as well as the distribution of it with depth it is necessary to examine the T, $\mathcal{S}$ curves for each mass layer. Figure 15 shows the T, $\mathcal{S}$ curves for masses $M = \ln(M\ T-M_r)$ of 1.5, 2.0, 2.5, 3.09, 3.5, 4.0, 4.1, and 4.34. The first of these refers to the farthest outward progress of the zone and the last refers to a layer just inside the farthest inward progress, as indicated by the lack of any extension of the curve below $T = 10^4$ degrees. Planimetry of these curves gives the work integral $\oint T d\mathcal{S}$ at each layer. These are plotted as the dashed curve in Figure 11, showing the depth dependence of work production. When the work integrals are multiplied by e^M they become the solid curve, and the area under this curve is just the work produced. Identifying the interval from $M = 1.5$ to 4.1 as the H zone work producing region, we find the total to be

$$\int_{H\text{-Region}} dM_r \oint T d\mathcal{S} = 38,300 \text{ units.}$$

Since the pulsation energy is 2.45×10^6 units, the work production by the H zone is 1.56 percent of the pulsation energy per period.

The figure shows that although the maximum of the work integral per unit mass occurs near the equilibrium H zone (shown by the arrows), in fact two-thirds of the total work is produced below that depth. Furthermore, the

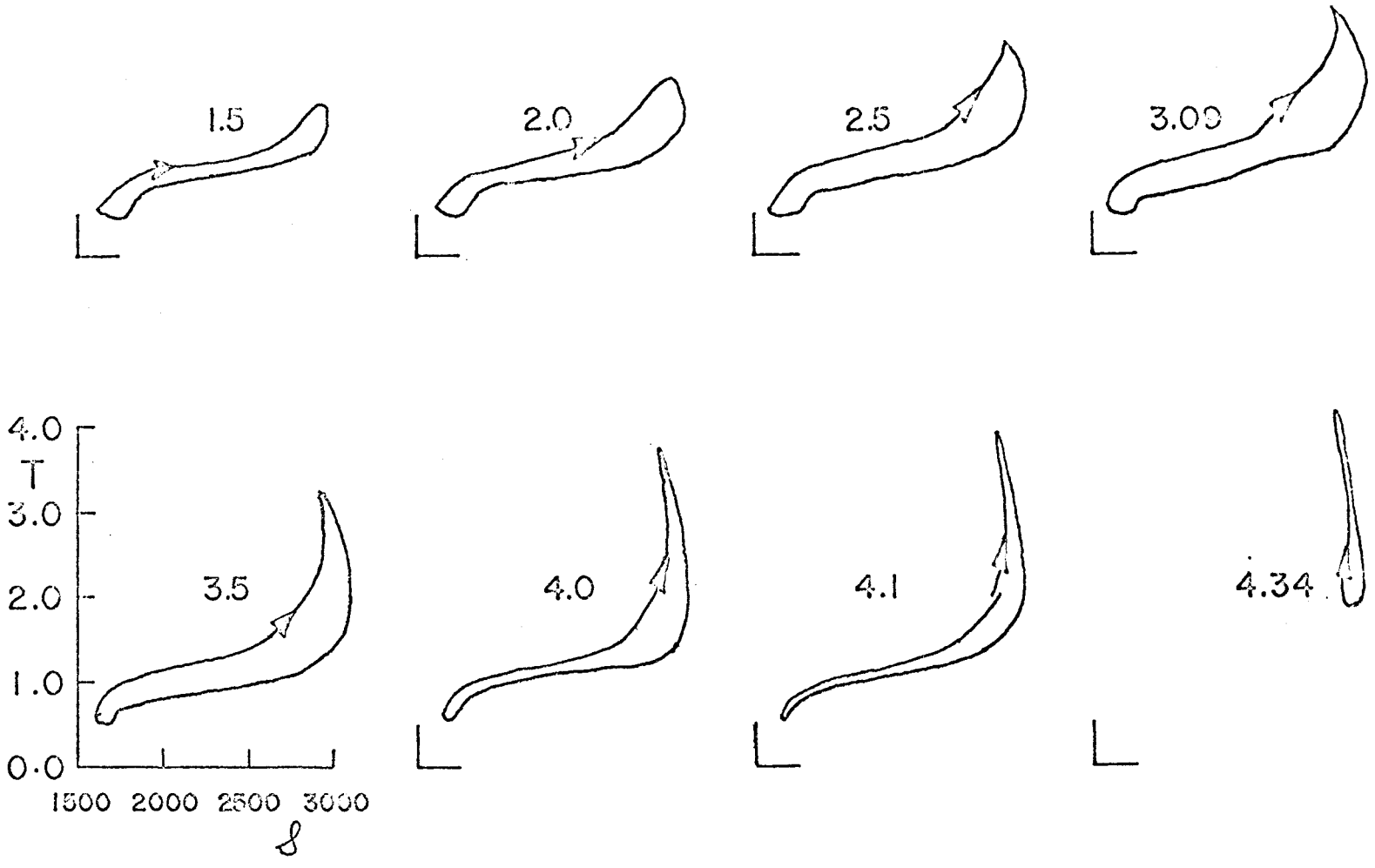

Figure 15. Temperature-entropy loops for mass elements at the indicated $\ln(MT-M_r)$, mostly in the H region

energy required to ionize the entire region above the equilibrium H zone is only 30,000 units, which is less than the total work produced.

For comparison the histogram also shown in Figure 11 indicates the work production of each shell in Christy's calculation, and is directly comparable with the solid curve. The distribution with depth is about the same, although there is still some work produced by his model in the shell extending from 4.2 to 4.6. The total of all the shells outside $M = 4.6$ is 3.90×10^4 units, or 1.55 percent of the pulsation energy per period. This figure is uncertain since it is doubtful whether or not the 4.2 to 4.6 shell should be counted as part of the H region, since the minimum temperature it attained was 12,400 degrees. It does seem, however, that this calculation in general supports the earlier result for H zone work production.

c. The Hydrogen Zone, a Quasi-Linear Theory

Due to the uncertainties expressed about H zone work production, for example in Christy (1966b), it may be of interest to give an approximate treatment, valid when the H zone can be treated as an ionization front and when otherwise the amplitude is small. Recalling the I-front jump conditions, we expect that when the amplitude is small the transition from the ionized to the neutral

state takes place at constant pressure, from a temperature T_o near 8000 degrees to a temperature T_1 near 15000 degrees. The T, $\mathcal{S}$ diagram should look like Figure 16 where the T, $\mathcal{S}$ segments from T_o to T_1 are isobars at pressures P_{out} (T_o to T_1) and P_{in}. Supposing the amplitude to be small, the area of the loop is essentially the area of the section between T_o and T_1. That area is given by

$$\int_{T_o}^{T_1} (P_{IN} - P_{OUT}) \left(\frac{\partial \mathcal{S}}{\partial p}\right)_T dT = \int_{T_o}^{T_1} (P_{IN} - P_{OUT}) \left(-\left(\frac{\partial V}{\partial T}\right)_p\right) dT$$

$$\doteq (P_{out} - P_{in})\left(V(T_1, p) - V(T_o, p)\right)$$

$$= (P_{out} - P_{in})\left(\frac{1}{\rho_1} - \frac{1}{\rho_o}\right).$$

To find the total work done by the H zone this must be integrated over the mass the H zone sweeps over during the cycle with the appropriate P_{out} and P_{in} substituted.

The motion of the H zone is governed by the energy jump condition, which is

$$L_1 - L_o = \chi \dot{M}_H ,$$

χ being the jump in specific enthalpy across the zone. In the linear case we may take $\dot{M}_H$ to be the time derivative of δM, a small displacement of the zone in mass, and let it vary as $e^{i\omega t}$. When the luminosities are linearized as well,

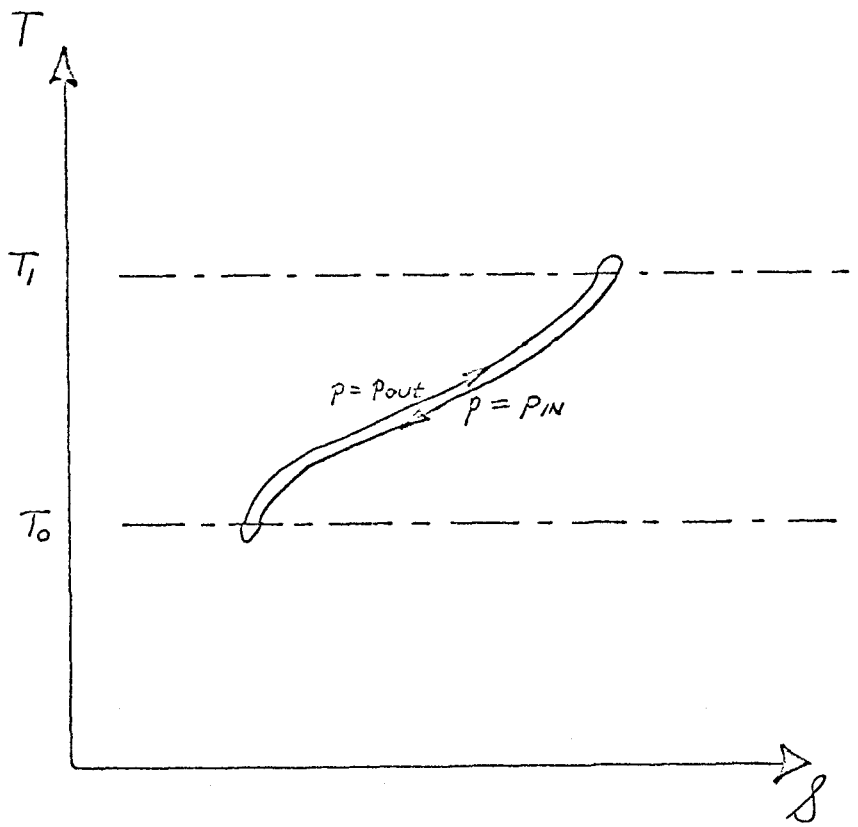

Figure 16. Temperature-entropy loop for a mass element crossed by the H-zone in quasi-linear pulsation

$$L_0 = L_{(0)}(1+\ell_0 e^{i\omega t}),\ L_1 = L_{(0)}(1+\ell_1 e^{i\omega t}),$$

the result is

$$L_{(0)}(\ell_1 - \ell_0) = i\omega\chi\,\delta M\ .$$

The material whose displacement from the equilibrium H zone is $/\delta M/\cos\phi$ passes from outside to inside when the pressure is

$$P = P_{out} = P_0 |p| \cos(\arg(p) - \arg(\delta M) - \phi)$$

where $P = P_0(1+p)$ defines the pressure variation p as in Baker and Kippenhahn (1965, called B&K below) and where p is a complex variable whose phase is $\arg(p)$. Similarly the value of P_{in} is given by

$$P_{in} = P_0 |p| \cos(\arg(p) - \arg(\delta M) + \phi)\ .$$

Therefore the total H zone work is

$$|\delta M| P_0 |p| \left(\frac{1}{\rho_1} - \frac{1}{\rho_0}\right) \int_0^{\pi} \sin\phi\, d\phi \left[\cos(\arg(p) - \arg(\delta M) - \phi) - \cos(\arg(p) - \arg(\delta M) + \phi)\right]$$

$$= 2 |\delta M \cdot p| P_0 \left(\frac{1}{\rho_1} - \frac{1}{\rho_0}\right) \frac{\pi}{2} \sin(\arg(p) - \arg(\delta M))$$

$$= -\pi P_0 \left(\frac{1}{\rho_1} - \frac{1}{\rho_0}\right) \mathrm{Im}(p^* \delta M)\ .$$

Substituting for δM in terms of $l_1 - l_0$, this becomes

$$W = \frac{\pi L(0)}{\omega} \frac{P_0\left(\frac{1}{P_1} - \frac{1}{P_0}\right)}{\chi} Re\left(p^*(l_1 - l_0)\right).$$

The values of l_0 and l_1 which appear here must in principle be obtained from a solution of the nonadiabatic problem as was done by Baker and Kippenhahn, using the appropriate boundary conditions at the center and surface and applying the differential equations through the H zone itself. However as Equations (11) and (12) of B&K show, in the region where $\nabla_{rad} = \frac{d\log T}{d\log p}$ is very large, that is, in the H zone, the nonadiabatic problem becomes very nearly singular. As a consequence the luminosity variations l_0 and l_1, tend to be well determined by conditions in the neutral and ionized regions separately, and do not depend very much on conditions in the H zone itself. The H zone functions only as an inner or outer boundary which moves in accordance with the energy jump condition. These conclusions break down when ∇_{rad} is small enough to allow interactions through the zone, as when convection dominates or when T_e is sufficiently high.

We see that, as we expected, the work is proportional to the amplitude squared, or to the pulsation energy. The work is positive when the excess of flux entering the zone over the flux leaving is in phase with the pressure.

Because of the pressure modulation discussed earlier, it is expected that $Re[p^* \ell_0] < 0$, that is, ℓ_0 is out of phase with the pressure. The expectation is confirmed by the results shown by B&K. However, ℓ_1 refers to a region where Kramers type opacity is valid and so ℓ_1 is in phase with the pressure, at least to the extent that $Re[p^* \ell_1] > 0$. Thus the work is positive, as the w-integral of B&K shows.

To compare the results of the exact linear theory of B&K with this quasi-linear, linear except for the ionization front, treatment, we can identify the linear work in the H zone as the jump in the w-integral:

$$W_{LIN} = 4\pi^2 P_0 R_0^3 \, Im[-p^*(X_1 - X_0)]$$

while

$$W_{QLIN} = \frac{\pi L(0)}{\omega} \frac{P_0 \left(\frac{1}{P_1} - \frac{1}{P_0}\right)}{\chi} Re[p^*(\ell_1 - \ell_0)]$$

so

$$\frac{W_{QLIN}}{W_{LIN}} = \frac{L(0)\left(\frac{1}{P_1} - \frac{1}{P_0}\right)}{4\pi R_0^3 \omega \chi} \cdot \frac{Re[p^*(\ell_1 - \ell_0)]}{Im[-p^*(X_1 - X_0)]}$$

and inserting values obtained for model #7 of B&K gives

$$\frac{W_{QLIN}}{W_{LIN}} = 0.69 .$$

Thus is seems that the H zone is somewhat less efficient in the finite-but-small amplitude case than in the

infinitesimal case.

Since the H zone work is not sensitive to the width of the zone, as it might be affected by convection, but is affected (proportionally) by changes in the pressure amplitude in the zone, the earlier result of B&K (1962) in which they omitted convection but required p to vanish at the surface and found the H zone work to be small is explained by the latter condition rather than the former.

Returning to the first expression for the H zone work,

$$W = -\pi P_0 \left(\frac{1}{\rho_1} - \frac{1}{\rho_0}\right) \mathcal{I}m(p^* \delta M)$$

and inserting ρ_0 and ρ_1 in terms of P_0, C_0, C_1, we have

$$W = -\left(300(km/sec)^2\right) \mathcal{I}m(p^* \delta M).$$

When the amplitude increases this expression is no longer proportional to the pulsation energy. First, p is likely to increase faster than the velocity amplitude due to the shorter duration of the compression phase and to the formation of weak R fronts which lower P_{in} (effectively). And as δM approaches and surpasses the amount of mass exterior to the H zone it tends not to vary with the velocity amplitude. But δM is still determined by ℓ_1,

ing all the mass which the flux excess $\ell_1 L_{(0)}$

can ionize during the compression phase. But ℓ_1 itself is likely to be proportional to the pressure amplitude. Finally, then, we can understand why the H zone work production increases more rapidly than the pulsation energy for large amplitudes. The thing most likely to alter this trend at very large amplitudes is the formation of shock-type ionization fronts, strong R or D type, such as appeared in the second compression phase of the present calculation.

Part III

Relationship of Dynamical Models to Observations

A. Non-equilibrium Model Atmospheres

At this point it is well to recall the objective of the calculations: to make a dynamical model from which it would be possible to infer some of the observable atmospheric properties. The model which was discussed in the preceding part is the basis for attaining this objective, but the atmospheric description in these envelopes is not refined enough for the purpose of making the desired predictions. Instead the deviations from equilibrium were extracted from the envelope models and imposed on detailed atmosphere models.

These deviations were specified by PNO, the lagrangian variation of ln(p), given as a function of tau, and

$$\frac{4}{3}\frac{T^4(\tau)}{T_e^4(\tau+q(\tau))}$$

which gives the temperature distribution in terms of the equilibrium temperature distribution for the same effective temperature. The PNO values were converted to gravities by

$$p(\tau) = m(\tau)\left[e^{PNO}\cdot\frac{GM_n r^2}{r_o^4}\right]_\tau = m(\tau)g(\tau)$$

where m(τ) is the mass per unit area overlying the depth

τ, r is the radius in the dynamical model at that depth, r_o is the equilibrium radius for that mass shell. The state of the atmosphere at a given time, then, was specified using the results of the dynamical calculation by giving T_e and the runs of

$$\frac{\frac{4}{3}T^4(\tau)}{T_e^4(\tau+q(\tau))} \quad \text{and} \quad q(\tau)$$

To illustrate the deviations of the "source function" $\frac{4}{3}\frac{T^4(\tau)}{T_e^4}$ from the equilibrium function the ratio of these as given by the dynamical calculation is shown for various times during the period in Figure 17. The parameter is the time t. It can be seen immediately that the range $.1 \leq \tau \leq 10$ is more nearly in equilibrium than either $\tau > 10$, which is in the H zone, or $\tau < 0.1$ which is too thin to relax quickly. The deep region shown a rise in the source-function ratio when the zone is moving outward and a decline when it is moving inward. The outer region, $\tau < 0.1$, shows temperature deviations due to incomplete relaxation of the work input to this material.

The degree of deviation to be expected can be estimated as follows. Since the relaxation time of the optically thin material is

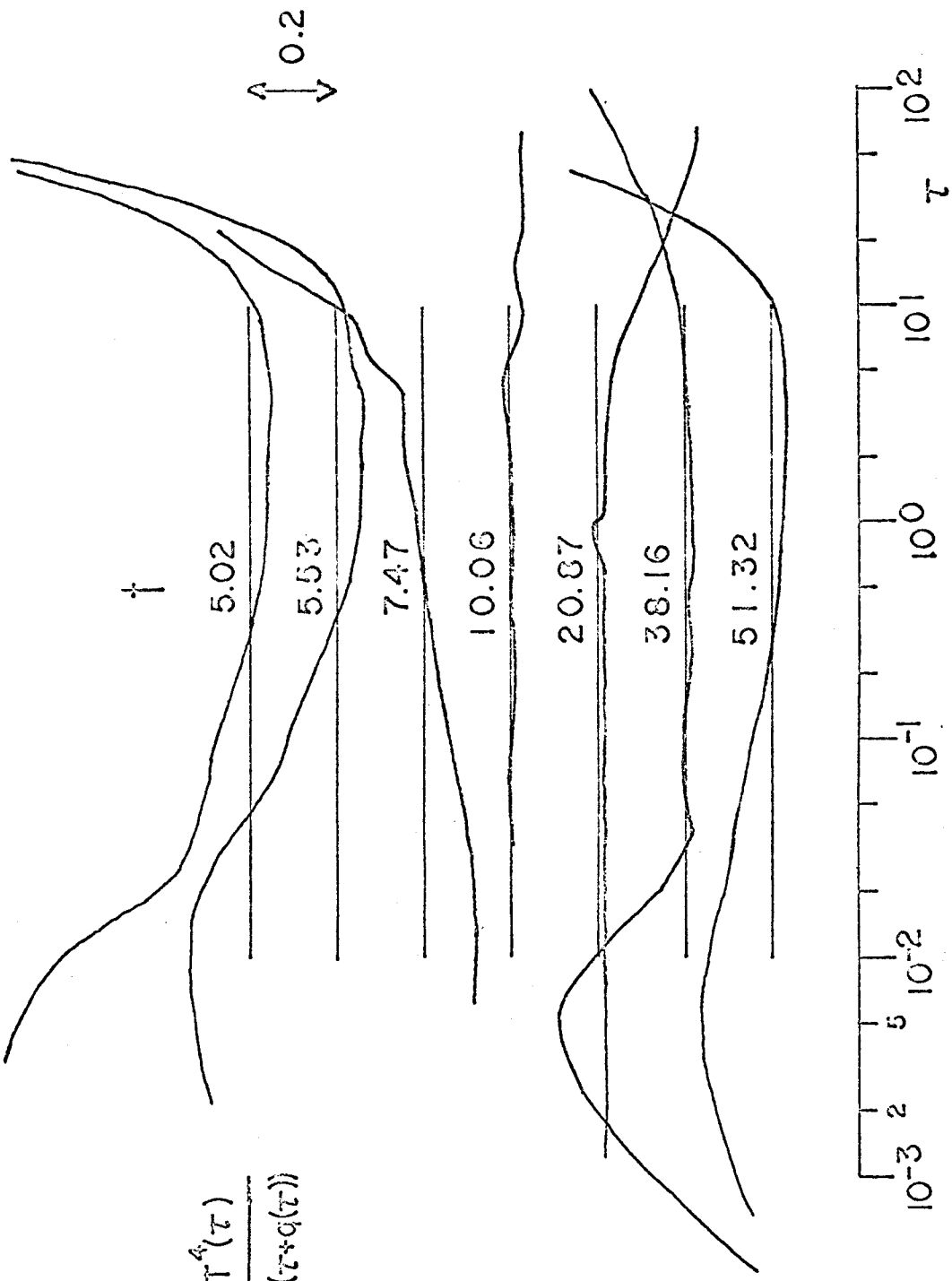

Figure 17. Temperature distributions in terms of the equilibrium for selected phases. The horizontal lines indicate unity.

$$t_R = \frac{C_V T_0}{4\pi \kappa \frac{\sigma}{\pi} T_0^4} = \frac{C_V}{\kappa a c T_0^3}$$

and if work is being done on the material at a rate, per unit mass,

$$C_V \frac{T_0}{t_W} \quad , \quad t_W \sim \frac{C_S}{g} \quad ,$$

the temperature excess is given by

$$\frac{\Delta T}{T} \sim \frac{t_R}{t_W} \sim \frac{g}{C_S} \frac{C_V}{4\kappa\sigma T_0^3} \quad .$$

Near the isothermal surface we can put

$$\kappa \sim p^{1/2} \quad \text{so} \quad \tau = \frac{2}{3} \frac{\kappa p}{g} \quad \text{and} \quad \kappa = \frac{3}{2} \frac{\tau g}{p}$$

so

$$\frac{\Delta T}{T} \sim \frac{1}{6} \quad \frac{P/C_S \cdot C_V T_0}{\tau \cdot \sigma T_0^4} \sim \frac{\gamma}{3\tau} \frac{\rho C_S C_V T_0}{2\sigma T_0^4} \sim \frac{\gamma}{3\tau} \frac{\rho C_S C_V T_0}{\sigma T_e^4} .$$

The second factor in the last expression is a measure of the possible local convective flux compared to the total flux. Thus the assumption that convection is negligible in the photosphere is equivalent to the neglect of nonequilibrium effects on the temperature distribution. For the models at $t = 7.47$ and 20.87 the run of $\Delta T/T$ is as follows:

7.47		20.87	
τ	$\Delta T/T$	τ	$\Delta T/T$
.001	3.7	.001	.4
.01	2.4	.01	.2
.05	1.2	.05	.12
.1	.8	.1	.09
.2	.5	.2	.06
.5	.2	.5	.03
1.0	.1	1.0	.06

The difference between the relaxation rates of the two atmospheres is obvious. This difference is quite apparent in Figure 16 where the high gravity models 5.02, 5.53, 7.47, 38.16 and 51.32 show much more deviation from equilibrium than the low gravity models at 10.06 and 20.87. The source of the disturbance in models 5.02 and 5.53 is the pre-rise compression wave which, in Christy's model, produces the bump seen then in the velocity curve. The same effect is present a period later at 38.16, but, as we discussed, it comes earlier in the cycle.

The calculation of detailed model atmospheres given the temperature and pressure distributions implied by the dynamical model was done using basically the model atmosphere program written by Mihalas, which is described quite fully in Mihalas (1963) and (1965a). The program as it presently exists at Caltech has been slightly modified, in accordance with Mihalas' suggestions, and it has been translated from FORTRAN II into FORTRAN IV.

The procedure for the most part was identical with Mihalas' and will not be discussed here, but some modifications were necessary. While Mihalas used χ_{5000} to define the standard optical depth, it was necessary for compatibility with the dynamical model to use the Rosseland mean opacity. Mihalas' monochromatic opacity routines were used to compute a table of log (χ_{Ross}) and tabular interpolation in log p_e and θ was used in the program to give the standard opacity. The equation of hydrostatic equilibrium,

$$\frac{dp_g}{d\tau} = \frac{g}{\chi} - \frac{dp_r}{d\tau}$$

was replaced with

$$p_g = m(\tau)g(\tau) - \frac{1}{3}aT^4, \text{ where } \quad \frac{dm}{d\tau} = \frac{1}{\chi} .$$

The integration of the latter equation was initiated by finding m at tau = .0005 from the equation

$$\frac{d\tau}{d\log p_g} = \frac{p_g}{\frac{g(0)}{\chi(p_g, \theta(0))} - \left(\frac{dp_r}{d\tau}\right)_0}$$

and

$$p_g(.0005) = m(.0005)g(0) - \frac{1}{3}aT^4(0)$$

assuming $p_g = 0$ at tau = 0. With T(tau), hence $\theta(\tau)$, given from the dynamical model, the equation for $m(\tau)$,

hence p_g (tau) was integrated as in Mihalas' procedure. In these models convection was ignored. Once the run of physical variables had been obtained the equation of transfer was integrated to give the monochromatic fluxes and intensities. In this Mihalas' procedures were used intact, assuming the blackbody function $B_\nu(T)$ for the source function S_ν(tau).

In order to assess the effects of the deviations from equilibrium on the model atmospheres, 9 models were constructed, with temperature distributions given by the exact gray-body formula and pressure distributions in hydrostatic equilibrium, which form a 3x3 grid in temperature and gravity, including the equilibrium values for the chosen RR Lyrae model, and spanning the range of conditions encountered in the dynamical calculation. The procedure followed was the same as outlined above for the non-equilibrium case to make comparison meaningful. Then 13 non-equilibrium models corresponding to selected phases in the first pulsation period of the dynamical calculation were made.

The results of the calculation for the equilibrium model which corresponds to the static RR Lyrae star are given in Table IV. The independent variable is the Rosseland mean optical depth and the other quantities are mostly self-explanatory. The radiation pressure is computed

Table IV

RESULTS OF MODEL ATMOSPHERE INTEGRATIONS

LOG GRAVITY= 2.820
EFFECTIVE TEMPERATURE=5.504E 03 EFFECTIVE THETA=0.775 FLUX=1.014E 11
SURFACE TEMPERATURE=5.276E 03 SURFACE THETA=0.9554
FIRST GUESS AT LOG PE WAS -0.894 LOG PE AT TAU =.0005 IS-1.025 LOG PG AT TAU=.0005 IS 2.147

TAU	THETA	TEMPERATURE	LOG PG	LOG PE	LOG PR	DENSITY	KAPPA(4444)	KAPPA BAR	DEPTH(KM)
0.	0.955	5.276E 03	2.147	-1.025	0.291	4.264E-10	3.443E-03	3.442E-03	0.
0.001	0.954	5.282E 03	2.355	-0.912	0.293	6.868E-10	4.150E-03	4.153E-03	2.393E 03
0.002	0.953	5.287E 03	2.467	-0.798	0.295	1.121E-09	5.084E-03	5.088E-03	4.826E 03
0.003	0.952	5.292E 03	2.691	-0.729	0.296	1.488E-09	5.780E-03	5.777E-03	6.242E 03
0.004	0.952	5.297E 03	2.778	-0.679	0.298	1.816E-09	6.353E-03	6.357E-03	7.242E 03
0.006	0.950	5.306E 03	2.899	-0.606	0.301	2.398E-09	7.309E-03	7.311E-03	8.640E 03
0.008	0.948	5.315E 03	2.984	-0.551	0.303	2.911E-09	8.120E-03	8.118E-03	9.618E 03
0.010	0.947	5.323E 03	3.049	-0.508	0.306	3.377E-09	8.839E-03	8.837E-03	1.037E 04
0.015	0.943	5.342E 03	3.169	-0.424	0.313	4.394E-09	1.041E-02	1.041E-02	1.172E 04
0.020	0.940	5.361E 03	3.246	-0.360	0.318	5.272E-09	1.179E-02	1.179E-02	1.265E 04
0.025	0.937	5.378E 03	3.307	-0.307	0.324	6.050E-09	1.307E-02	1.307E-02	1.336E 04
0.030	0.934	5.395E 03	3.356	-0.261	0.330	6.750E-09	1.429E-02	1.429E-02	1.393E 04
0.035	0.932	5.411E 03	3.396	-0.220	0.335	7.386E-09	1.546E-02	1.546E-02	1.441E 04
0.040	0.929	5.427E 03	3.431	-0.183	0.340	7.971E-09	1.661E-02	1.661E-02	1.481E 04
0.060	0.919	5.486E 03	3.531	-0.060	0.359	9.945E-09	2.103E-02	2.103E-02	1.601E 04
0.080	0.910	5.540E 03	3.599	0.040	0.376	1.151E-08	2.541E-02	2.541E-02	1.682E 04
0.100	0.902	5.591E 03	3.648	0.125	0.391	1.278E-08	2.963E-02	2.984E-02	1.741E 04
0.125	0.892	5.646E 03	3.695	0.218	0.410	1.406E-08	3.552E-02	3.552E-02	1.798E 04
0.150	0.883	5.700E 03	3.732	0.302	0.427	1.514E-08	4.146E-02	4.148E-02	1.844E 04
0.200	0.867	5.811E 03	3.785	0.445	0.459	1.683E-08	5.413E-02	5.412E-02	1.910E 04
0.250	0.853	5.907E 03	3.822	0.567	0.487	1.803E-08	6.793E-02	6.793E-02	1.957E 04
0.300	0.841	5.996E 03	3.850	0.675	0.513	1.893E-08	8.303E-02	8.302E-02	1.995E 04
0.350	0.829	6.080E 03	3.872	0.772	0.537	1.963E-08	9.944E-02	9.945E-02	2.022E 04
0.400	0.818	6.160E 03	3.889	0.860	0.560	2.017E-08	1.173E-01	1.172E-01	2.045E 04
0.500	0.799	6.308E 03	3.915	1.017	0.601	2.092E-08	1.572E-01	1.572E-01	2.081E 04
0.600	0.782	6.445E 03	3.935	1.152	0.638	2.139E-08	2.032E-01	2.033E-01	2.107E 04
0.700	0.767	6.572E 03	3.949	1.272	0.672	2.167E-08	2.550E-01	2.550E-01	2.125E 04
0.800	0.753	6.691E 03	3.960	1.380	0.704	2.183E-08	3.151E-01	3.151E-01	2.144E 04
1.000	0.729	6.910E 03	3.976	1.567	0.759	2.192E-08	4.559E-01	4.559E-01	2.160E 04
1.200	0.709	7.108E 03	3.988	1.725	0.809	2.183E-08	6.284E-01	6.286E-01	2.165E 04
1.400	0.691	7.290E 03	3.996	1.862	0.852	2.164E-08	8.365E-01	8.364E-01	2.198E 04
1.600	0.676	7.459E 03	4.002	1.982	0.892	2.140E-08	1.083E 00	1.083E 00	2.207E 04
1.800	0.662	7.616E 03	4.006	2.090	0.928	2.115E-08	1.371E 00	1.372E 00	2.215E 04
2.000	0.649	7.764E 03	4.010	2.187	0.962	2.084E-08	1.706E 00	1.706E 00	2.221E 04
2.500	0.622	8.101E 03	4.016	2.392	1.036	2.009E-08	2.760E 00	2.760E 00	2.233E 04
3.000	0.600	8.400E 03	4.020	2.559	1.099	1.934E-08	4.166E 00	4.165E 00	2.240E 04
3.500	0.581	8.670E 03	4.023	2.698	1.154	1.860E-08	5.957E 00	5.953E 00	2.245E 04
4.000	0.565	8.916E 03	4.025	2.816	1.202	1.789E-08	8.139E 00	8.145E 00	2.249E 04
5.000	0.539	9.356E 03	4.027	3.006	1.286	1.653E-08	1.368E 01	1.370E 01	2.254E 04
6.000	0.517	9.741E 03	4.029	3.150	1.356	1.528E-08	2.055E 01	2.058E 01	2.256E 04
8.000	0.485	1.040E 04	4.030	3.353	1.469	1.308E-08	3.631E 01	3.625E 01	2.262E 04
10.000	0.460	1.095E 04	4.031	3.480	1.559	1.134E-08	5.025E 01	5.022E 01	2.265E 04
14.000	0.425	1.185E 04	4.033	3.609	1.697	9.093E-09	6.166E 01	6.187E 01	2.271E 04
18.000	0.400	1.259E 04	4.034	3.663	1.801	7.921E-09	5.692E 01	5.692E 01	2.277E 04
22.000	0.381	1.321E 04	4.035	3.686	1.886	7.262E-09	4.742E 01	4.747E 01	2.285E 04
26.000	0.366	1.376E 04	4.037	3.698	1.956	6.887E-09	3.902E 01	3.900E 01	2.295E 04
30.000	0.354	1.426E 04	4.040	3.707	2.017	6.610E-09	3.239E 01	3.241E 01	2.310E 04
40.000	0.330	1.529E 04	4.048	3.721	2.139	6.206E-09	2.209E 01	2.212E 01	2.363E 04
50.000	0.312	1.615E 04	4.060	3.738	2.234	5.983E-09	1.690E 01	1.690E 01	2.442E 04
60.000	0.298	1.689E 04	4.075	3.757	2.313	5.870E-09	1.401E 01	1.401E 01	2.546E 04

Table IV (Continued)

RESULTS OF MODEL ATMOSPHERE INTEGRATIONS

TAU	H I	H PLUS	HE 1	HE 2	DPR/DTAU	RADIATIVE GRADIENT	ADIABATIC GRADIENT	C SUB P	CONVECTVE VELOCITY	CONVECTVE FLUX
0.	9.993E-01	7.307E-04	1.000E 00	9.359E-14	4.229E 00	9.495E-04	3.470E-01	1.953E 08	0.	0.
0.001	9.994E-01	5.849E-04	1.000E 00	7.767E-14	4.224E 00	1.554E-03	3.574E-01	1.842E 08	0.	0.
0.002	9.995E-01	4.649E-04	1.000E 00	6.276E-14	4.219E 00	2.763E-03	3.641E-01	1.764E 08	0.	0.
0.003	9.996E-01	4.091E-04	1.000E 00	5.648E-14	4.214E 00	3.939E-03	3.703E-01	1.731E 08	0.	0.
0.004	9.996E-01	3.752E-04	1.000E 00	5.293E-14	4.209E 00	5.033E-03	3.728E-01	1.711E 08	0.	0.
0.006	9.996E-01	3.349E-04	1.000E 00	4.920E-14	4.199E 00	7.265E-03	3.759E-01	1.689E 08	0.	0.
0.008	9.997E-01	3.114E-04	1.000E 00	4.757E-14	4.189E 00	9.354E-03	3.777E-01	1.676E 08	0.	0.
0.010	9.997E-01	2.960E-04	1.000E 00	4.692E-14	4.179E 00	1.127E-02	3.785E-01	1.668E 08	0.	0.
0.015	9.997E-01	2.743E-04	1.000E 00	4.744E-14	4.154E 00	1.631E-02	3.807E-01	1.656E 08	0.	0.
0.020	9.997E-01	2.641E-04	1.000E 00	4.956E-14	4.129E 00	2.097E-02	3.816E-01	1.650E 08	0.	0.
0.025	9.997E-01	2.592E-04	1.000E 00	5.254E-14	4.104E 00	2.551E-02	3.821E-01	1.646E 08	0.	0.
0.030	9.997E-01	2.567E-04	1.000E 00	5.618E-14	4.080E 00	2.996E-02	3.824E-01	1.644E 08	0.	0.
0.035	9.997E-01	2.577E-04	1.000E 00	6.036E-14	4.056E 00	3.432E-02	3.825E-01	1.643E 08	0.	0.
0.040	9.997E-01	2.593E-04	1.000E 00	6.500E-14	4.032E 00	3.796E-02	3.826E-01	1.642E 08	0.	0.
0.050	9.997E-01	2.719E-04	1.000E 00	8.837E-14	3.985E 00	5.577E-02	3.822E-01	1.643E 08	0.	0.
0.080	9.996E-01	2.956E-04	1.000E 00	1.197E-13	3.846E 00	7.233E-02	3.813E-01	1.646E 08	0.	0.
0.100	9.996E-01	3.219E-04	1.000E 00	1.606E-13	3.759E 00	8.844E-02	3.801E-01	1.652E 08	0.	0.
0.125	9.996E-01	3.593E-04	1.000E 00	2.281E-13	3.650E 00	1.092E-01	3.785E-01	1.659E 08	0.	0.
0.150	9.995E-01	4.004E-04	1.000E 00	3.174E-13	3.547E 00	1.287E-01	3.767E-01	1.668E 08	0.	0.
0.200	9.994E-01	4.952E-04	1.000E 00	5.865E-13	3.352E 00	1.722E-01	3.727E-01	1.688E 08	0.	0.
0.250	9.993E-01	6.050E-04	1.000E 00	1.024E-12	3.171E 00	2.144E-01	3.682E-01	1.711E 08	0.	0.
0.300	9.992E-01	7.296E-04	1.000E 00	1.704E-12	3.003E 00	2.576E-01	3.634E-01	1.736E 08	0.	0.
0.350	9.991E-01	8.696E-04	1.000E 00	2.727E-12	2.847E 00	3.019E-01	3.583E-01	1.764E 08	0.	0.
0.400	9.989E-01	1.026E-03	1.000E 00	4.219E-12	2.702E 00	3.486E-01	3.530E-01	1.794E 08	0.	0.
0.500	9.986E-01	1.387E-03	1.000E 00	9.267E-12	2.444E 00	4.425E-01	3.416E-01	1.862E 08	7.112E-01	2.608E 07
0.600	9.982E-01	1.811E-03	1.000E 00	1.868E-11	2.221E 00	5.410E-01	3.297E-01	1.940E 08	1.043E 00	9.364E 07
0.700	9.977E-01	2.322E-03	1.000E 00	3.499E-11	2.030E 00	6.445E-01	3.173E-01	2.027E 08	1.315E 00	1.970E 08
0.800	9.971E-01	2.904E-03	1.000E 00	6.182E-11	1.865E 00	7.430E-01	3.044E-01	2.125E 08	1.541E 00	3.352E 08
1.000	9.957E-01	4.317E-03	1.000E 00	1.679E-10	1.601E 00	9.866E-01	2.800E-01	2.350E 08	2.004E 00	8.024E 08
1.200	9.939E-01	6.065E-03	1.000E 00	3.956E-10	1.405E 00	1.237E 00	2.564E-01	2.615E 08	2.418E 00	1.532E 09
1.400	9.918E-01	8.196E-03	1.000E 00	8.377E-10	1.260E 00	1.509E 00	2.347E-01	2.920E 08	2.823E 00	2.638E 09
1.600	9.893E-01	1.069E-02	1.000E 00	1.628E-09	1.153E 00	1.803E 00	2.153E-01	3.263E 08	3.226E 00	4.245E 09
1.800	9.864E-01	1.356E-02	1.000E 00	2.956E-09	1.073E 00	2.118E 00	1.981E-01	3.643E 08	3.635E 00	6.512E 09
2.000	9.831E-01	1.687E-02	1.000E 00	5.077E-09	1.014E 00	2.412E 00	1.831E-01	4.060E 08	4.014E 00	9.355E 09
2.500	9.731E-01	2.674E-02	10.000E-01	1.619E-08	9.253E-01	3.417E 00	1.535E-01	5.259E 08	5.173E 00	2.299E 10
3.000	9.604E-01	3.964E-02	10.000E-01	4.227E-08	8.634E-01	4.499E 00	1.329E-01	6.658E 08	6.385E 00	4.798E 10
3.500	9.450E-01	5.501E-02	10.000E-01	9.563E-08	8.135E-01	5.708E 00	1.165E-01	8.239E 08	7.717E 00	9.122E 10
4.000	9.271E-01	7.292E-02	10.000E-01	1.941E-07	8.542E-01	6.898E 00	1.082E-01	9.967E 08	9.081E 00	1.560E 11
5.000	8.835E-01	1.169E-01	10.000E-01	6.369E-07	8.476E-01	9.891E 00	9.542E-02	1.379E 09	1.238E 01	4.120E 11
6.000	8.306E-01	1.692E-01	10.000E-01	1.687E-06	8.462E-01	1.250E 01	8.857E-02	1.787E 09	1.567E 01	8.233E 11
8.000	7.053E-01	2.947E-01	10.000E-01	7.906E-06	8.458E-01	1.796E 01	8.346E-02	2.545E 09	2.274E 01	2.239E 12
10.000	5.673E-01	4.326E-01	10.000E-01	2.676E-05	8.458E-01	2.002E 01	8.384E-02	3.026E 09	2.718E 01	3.259E 12
14.000	3.257E-01	6.743E-01	9.998E-01	1.765E-04	8.458E-01	1.894E 01	9.356E-02	2.830E 09	2.830E 01	2.569E 12
18.000	1.778E-01	8.222E-01	9.993E-01	7.364E-04	8.458E-01	1.356E 01	1.133E-01	1.975E 09	2.257E 01	9.510E 11
22.000	1.005E-01	8.995E-01	9.977E-01	2.302E-03	8.458E-01	9.187E 00	1.422E-01	1.313E 09	1.719E 01	3.126E 11
26.000	6.068E-02	9.393E-01	9.942E-01	5.824E-03	8.458E-01	6.371E 00	1.759E-01	9.325E 08	1.352E 01	1.178E 11
30.000	3.915E-02	9.609E-01	9.874E-01	1.260E-02	8.458E-01	4.448E 00	2.068E-01	7.337E 08	1.089E 01	5.081E 10
40.000	1.634E-02	9.836E-01	9.456E-01	5.436E-02	8.458E-01	2.393E 00	2.348E-01	6.104E 08	7.752E 00	1.542E 10
50.000	8.597E-03	9.914E-01	8.532E-01	1.408E-01	8.458E-01	1.493E 00	2.091E-01	7.114E 08	6.240E 00	8.766E 09
60.000	5.236E-03	9.948E-01	7.137E-01	2.863E-01	8.458E-01	1.067E 00	1.864E-01	8.436E 08	5.422E 00	6.359E 09

as $1/3aT^4$. The quantity given as KAPPA (4444) is the interpolated value of χ_{Ross}, and KAPPA BAR is the same thing computed afterwards from the monochromatic opacities. The columns H I, H PLUS, HE 1, HE 2 are the fractions of H and He in the indicated stage of ionization. The radiative and adiabatic gradients refer to

$$\nabla = \frac{d\log T}{d\log P}$$

and the radiative gradient is the actual gradient in this case. The convective velocity and flux are computed from the actual temperature gradient using the mixing length theory without radiative losses. They were ignored in the model calculations.

Table V gives, for all the models, the results for the monochromatic magnitudes defined by

$$M(\nu) = 51.682 - 2.5 \log_{10}(4\pi R^2 F_\nu)$$

where F_ν is the physical flux per unit frequency interval and R is the radius derived from the dynamical model, both in cgs units. The constant has been adjusted so that $M(\nu)$ at 5500 Angstroms will agree with the Johnson V magnitudes, according to Willstrop's calibration (1960).

These quantities are directly comparable with spectrophotometry of actual stars. Figure 18 shows mono-

Table V

M(ν)*

t	λ	3126Å	3646	3647	4019	4475	5049	5792	6790	8203	8204	10503
0		3.249	2.692	2.276	2.056	1.848	1.655	1.488	1.361	1.275	1.268	1.244
5.02		3.417	2.858	2.534	2.294	2.065	1.851	1.663	1.518	1.419	1.415	1.388
6.41		3.164	2.672	2.316	2.112	1.914	1.727	1.565	1.443	1.364	1.358	1.345
7.47		2.534	2.151	1.548	1.432	1.317	1.207	1.118	1.065	1.051	1.032	1.085
8.12		2.158	1.819	0.853	0.804	0.753	0.707	0.680	0.687	0.739	0.680	0.814
8.54		2.041	1.704	0.725	0.682	0.637	0.599	0.580	0.596	0.660	0.594	0.746
10.06		1.888	1.547	0.120	0.141	0.165	0.197	0.245	0.324	0.449	0.291	0.533
17.15		2.399	1.965	0.743	0.699	0.654	0.610	0.578	0.576	0.614	0.525	0.654
20.87		2.568	2.090	1.073	0.989	0.902	0.817	0.746	0.707	0.708	0.651	0.730
28.73		2.835	2.302	1.647	1.472	1.304	1.149	1.027	0.924	0.873	0.854	0.870
38.16		3.076	2.508	2.010	1.805	1.609	1.426	1.267	1.148	1.070	1.060	1.048
42.58		3.148	2.596	2.175	1.955	1.749	1.552	1.382	1.255	1.171	1.163	1.145
51.32		3.296	2.757	2.370	2.149	1.938	1.742	1.571	1.442	1.358	1.351	1.334
θ_e, log g												
.875, 1.60		3.745	2.992	2.369	2.104	1.867	1.657	1.480	1.347	1.257	1.241	1.214
.875, 2.82		3.297	2.722	2.355	2.120	1.899	1.694	1.516	1.378	1.281	1.275	1.240
.875, 3.80		3.088	2.592	2.377	2.147	1.927	1.721	1.539	1.397	1.296	1.294	1.255
.775, 1.60		2.910	2.393	1.198	1.103	1.011	0.926	0.858	0.824	0.832	0.759	0.846
.775, 2.82		2.565	2.130	1.334	1.218	1.103	0.995	0.906	0.854	0.845	0.812	0.874
.775, 3.80		2.359	1.964	1.454	1.313	1.176	1.049	0.945	0.881	0.860	0.845	0.895
.638, 1.60		1.930	1.522	-0.110	-0.083	-0.043	0.011	0.084	0.185	0.332	0.093	0.389
.638, 2.82		1.766	1.416	-0.053	-0.028	0.001	0.038	0.091	0.174	0.305	0.134	0.386
.638, 3.80		1.556	1.255	0.071	0.071	0.072	0.082	0.110	0.173	0.286	0.175	0.390

*$M(\nu) = 50.145 - 2.5\log_{10}(\pi R^2 F_\nu)$; add $0^m.032$ to correspond to Willstrop

chromatic light curves for λ = 5400A, 4475A, 3647A. The horizontal lines mark the magnitudes of the equilibrium model. For comparison Figure 19, which is reproduced from Oke, Giver and Searle (1962), shows monochromatic light curves at λ = 4255A and 3636A for the Bailey a type RR Lyrae star SU Dra. The similarity is apparent, although the amplitudes are not the same. Of some interest is the indentation in the blue curve and the notch in the ultraviolet curve on the ascending branch. The following figure, Figure 20, shows a similar set of light curves for SW And (Oke 1966b), another a type RR Lyrae star but one which has somewhat different properties. In this star the rising branch notch is less conspicuous, as is the bump near minimum light. The model is probably a better fit in these respects to SW And than to SU Dra.

Two definite features of the observed monochromatic light curves which are predicted by the model, in addition to their general shape, are the depression at minimum light and the depression, or notch, or stillstand, at mid-rising light. Both these effects are due to the gravity modulation as we have seen.

The technique used by Oke et al to determine the radii of RR Lyrae stars relies on fitting the spectral distribution, expressed by the blue-visual continuum slope and the Balmer jump, to an equilibrium model atmosphere,

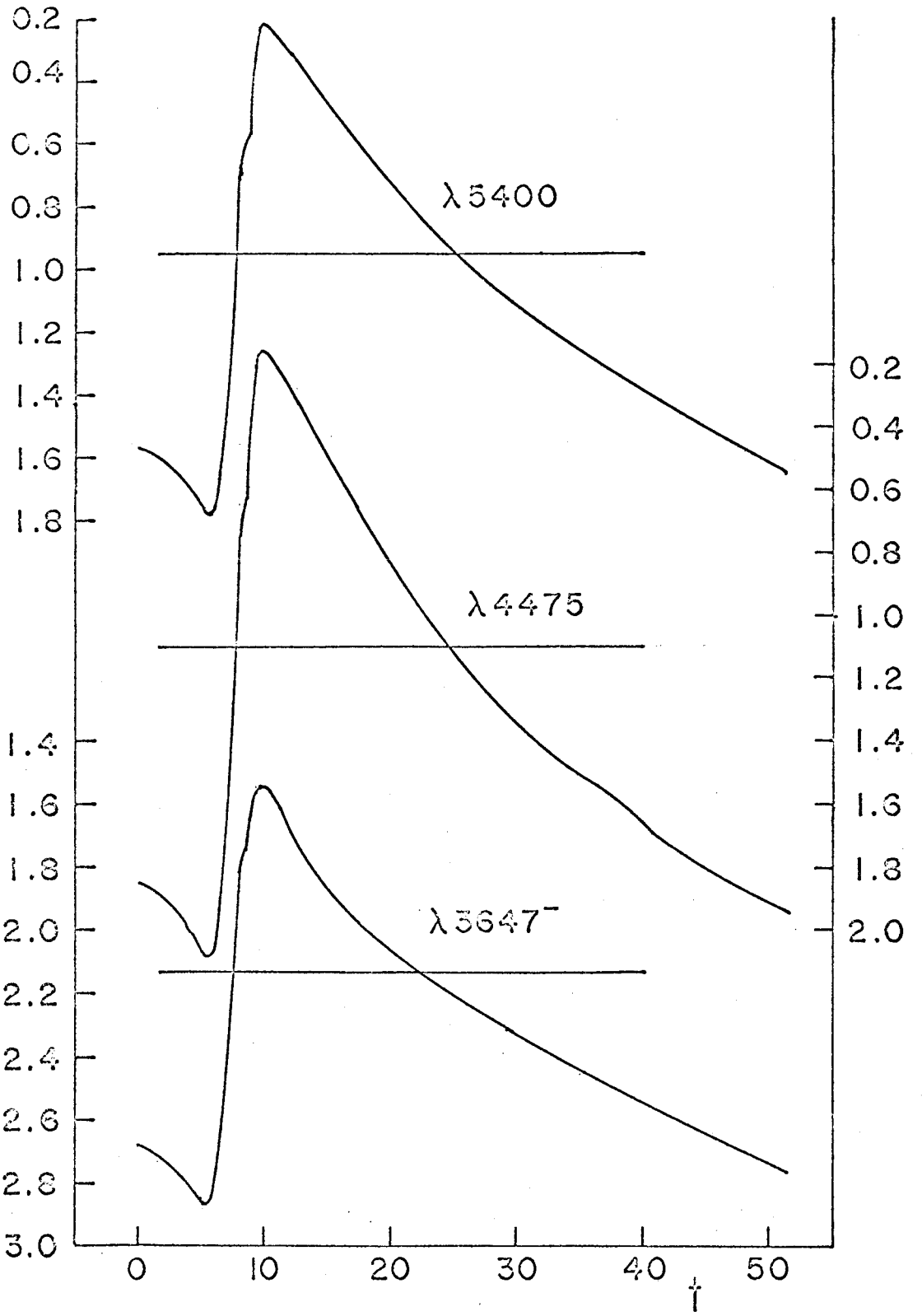

Figure 18. Variation of the absolute monochromatic magnitudes for the model. The horizontal lines indicate equilibrium values.

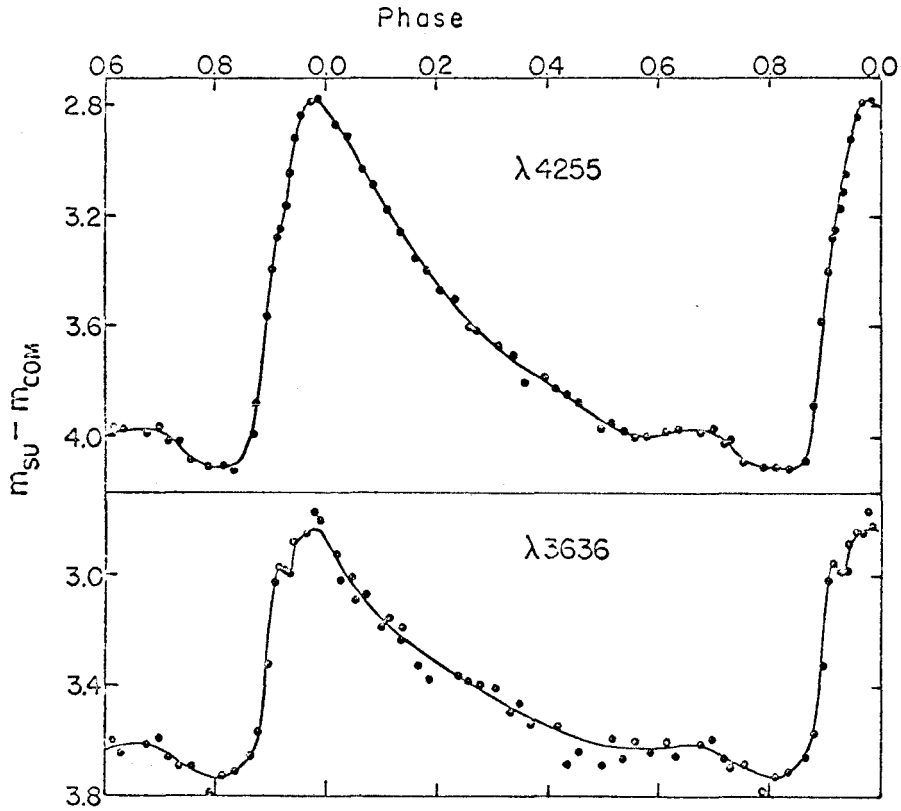

Figure 19. Monochromatic magnitude variation for SU Dra (Oke, Giver, and Searle 1962)

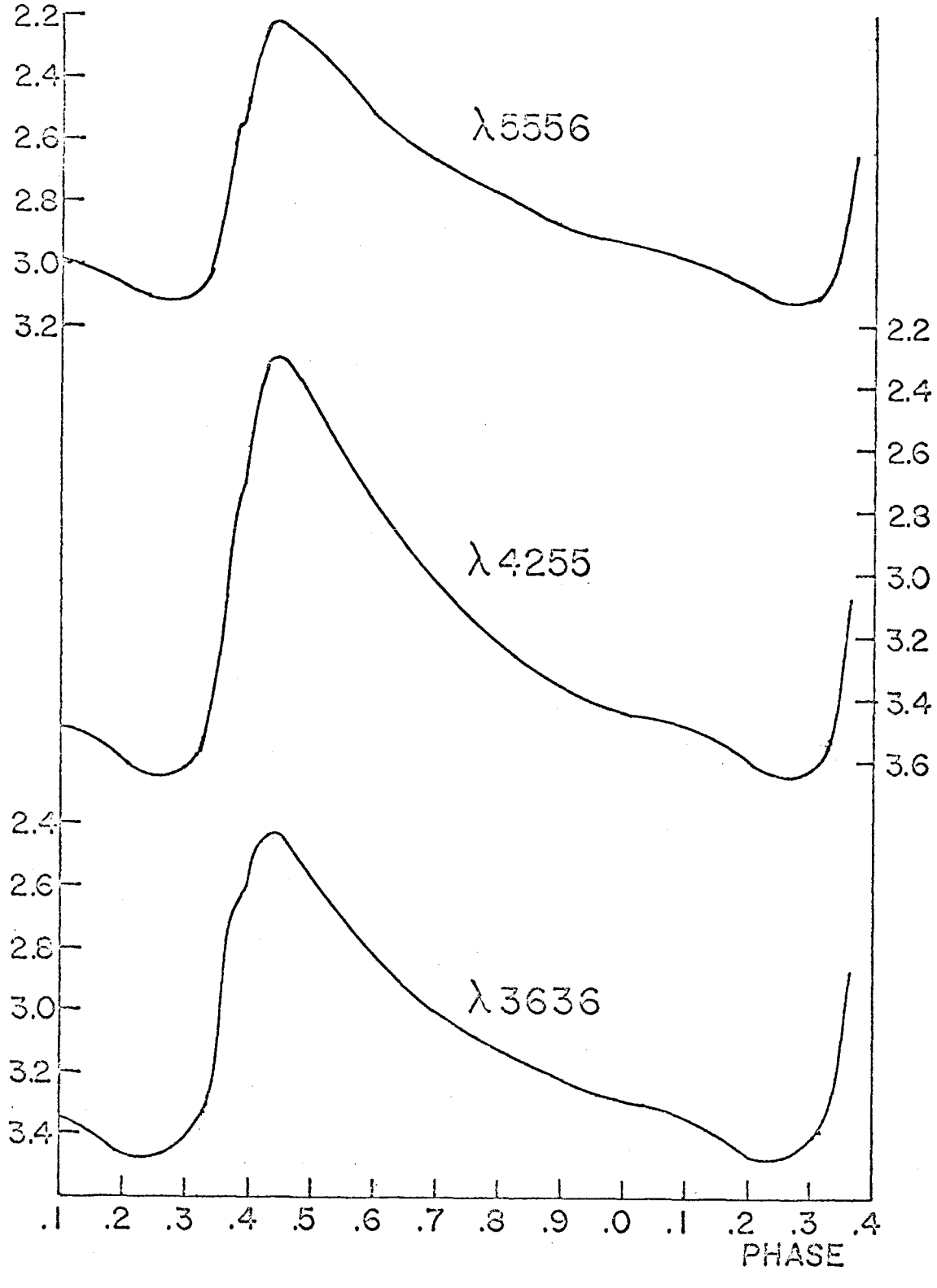

Figure 20. Monochromatic magnitude variation for SW And (Oke 1966b)

hence determining the temperature, gravity, and the flux per unit area of the star. The integrated velocity curve and the apparent light curve then yield the absolute radius curve.

The quantities which we can use to fit the temperature and gravity are C and D defined by

$$C = \frac{M_{5792} - M_{4475}}{\frac{1}{.4475} - \frac{1}{.5792}} \quad , \quad D = M_{3647-} - M_{3647+} .$$

The values of C and D for the grid of equilibrium atmospheres are given in Table VI. These can be used to predict C and D for a given θ_e and log g by quadratic interpolation in θ_e and log g. For a given pair, C and D, θ_e and log g can be iterated until the proper values are obtained. Using this procedure the temperature and gravity were found for all the dynamical atmospheres as if they were in equilibrium. In Table VII are collected the values of C and D, the fitted θ_e and log g (denoted by *), the true values and the differences. By the true gravity is meant g(2/3), with g(tau) as defined earlier; the true θ_e is determined by the actual flux from the dynamical model.

The two largest discrepancies in θ_e occur at 5.02 and 7.47, during the compression phase. The PNO curves for these models (Figure 8) show the atmosphere to be essentially in quasi-hydrostatic equilibrium in each

Table VI

θ_e	log g	C	D
.875	1.60	-.762	.623
.875	2.82	-.754	.367
.875	3.80	-.764	.215
.775	1.60	-.301	1.195
.775	2.82	-.388	.796
.775	3.80	-.455	.510
.638	1.60	.250	1.632
.638	2.82	.177	1.469
.638	3.80	.075	1.184

Table VII

t	C	D	θ_e*	log g*	θ_e	log g	$\Delta\theta$	Δlog g
0.	-.709	.42	.862	2.82	.862	2.78	0	.04
5.02	-.791	.33	.886	2.78	.874	3.02	.012	-.24
6.41	-.687	.35	.852	3.35	.849	3.36	.003	-.01
7.47	-.392	.60	.759	3.71	.769	3.63	-.010	.08
8.12	-.144	.97	.701	3.40	.700	3.54	.001	-.14
8.54	-.112	.98	.689	3.55	.686	3.72	.003	-.17
10.06	.157	1.43	.640	2.94	.640	2.98	0	-.04
17.15	-.150	1.22	.729	2.15	.734	2.40	-.005	-.25
20.87	-.307	1.02	.765	2.26	.771	2.40	-.006	-.14
28.73	-.565	.65	.825	2.54	.823	2.29	.002	.25
38.16	-.673	.50	.853	2.63	.852	2.55	.001	.08
42.58	-.716	.42	.864	2.77	.859	2.79	.005	-.02
51.32	-.722	.39	.866	2.90	.858	2.94	.008	-.04

case, PNO is constant to $\pm$ .02 from tau = .1 to 10. But as we see in Figure 17 these models are noticeably out of radiative equilibrium, both show a temperature gradient with respect to the equilibrium model having the same flux. At 5.02 the gradient was such that the surface was too hot while the region tau = 1 to 4 was too cool. Since it happens that $\tau_\nu(\tau)$ at 4000A is less than at 6000A, this non-equilibrium gradient makes the continuum look cooler, that is relatively less emission appears in the blue than in the red; as a consequence $\theta_e^* - \theta_e$ is +.012. At 7.47 the gradient in the opposite sense exists and $\theta_e^* - \theta_e$ is -.010.

The magnitude of these effects is obviously not very great. A change of .01 in theta, or 1.5 percent, means a change of 6 percent in the total luminosity and a similar change in the visual flux (which is determined mostly by the actual temperature at $\tau = 2/3$, and is not sensitive to the gradient). Since the visual flux determines the radius, a 3 percent change in the radius is possible. This figure is typical of the fluctuations apparent, for example, in the radius curve of SU Dra obtained by Oke, Giver and Searle. As the earlier discussion of equilibrium deviations pointed out, the most likely phase for deviations is the early compression phase when log g is high and T_e is low. Referring to Oke, Giver

and Searle again, we see that the high gravity phase does indeed present anomalies in the radii, of the proper magnitude. It is tempting to identify these with non-equilibrium effects, although there are several other uncertainties, such as inadequacies in the models, convection, photometric calibration, which are also important.

Since a substantial body of RR Lyrae star observations consists of two and three-color broad-band photometry it is of interest to compute the magnitudes on the UBV system from the monochromatic fluxes. In doing this we encounter the well-known difficulty of representing the empirical UBV magnitudes by integrals over the spectral distribution. The method of Matthews and Sandage (1963) was used, employing a program written by J. B. Oke, with the response functions, including two aluminum reflections, and the atmospheric extinction as given by Melbourne (1959). Matthews and Sandage transformed the theoretical u-b and b-v to Johnson U-B and B-V with expressions of the type

$$U-B = a(u-b)_1 + b\ ,\quad B-V = c(b-v)_0 + d\ .$$

The subscript, o or 1, is the number of air-masses of atmospheric extinction used in the calculation. To determine the transformation coefficients the colors were computed for several stars for which observed monochromatic fluxes were available. The results for three stars used

by Matthews and Sandage, α Lyr, HD140283 and 10 Lac, agreed fairly well with those given by Matthews and Sandage. The transformations derived are

$$B - V = 1.02\,(b-v)_o + 0.94$$

$$U - B = 0.97\,(u-b)_1 - 1.34\,.$$

In order to calibrate the V magnitudes to make them correspond with M_V the result, quoted earlier, by Willstrop for a star with B-V = 0.3 was used.

The values derived for M_V, B-V, and U-B of the grid of equilibrium models and for the dynamical models are given in Table VIII. The extrema and amplitudes are summarized in Table IX. Figure 21 shows the M_V, B-V, and U-B curves drawn from this data; Figure 22 is the two-color diagram showing the loop formed by the dynamical models and the main-sequence relation. The diagonal straight lines are rough metal and hydrogen line-blanketing vectors, that is, lines connecting the estimated positions of log g = 4.4 models with the main sequence relation at the same temperature. Most of the difference, at least for bluer models, is due to the omission of the effects of the Balmer line confluence.

With respect to the U-B, B-V loop it should be pointed out that the fact that there is one, while no strong shock occurs to affect the colors, rules out the

Table VIII

t	v_0	$(b-v)_o$	$(u-b)_1$	M_V	B-V	U-B
0	15.857	-.488	1.169	1.598	.44	-.21
5.02	16.035	-.453	1.164	1.776	.48	-.21
6.41	15.928	-.501	1.110	1.669	.43	-.26
7.47	15.456	-.641	1.062	1.197	.29	-.31
8.12	14.992	-.759	1.102	0.733	.16	-.27
8.54	14.888	-.769	1.092	0.629	.15	-.28
10.06	14.523	-.896	1.143	0.264	.03	-.23
17.15	14.892	-.759	1.193	0.633	.17	-.18
20.87	15.078	-.686	1.195	0.819	.24	-.18
28.73	15.371	-.559	1.203	1.112	.37	-.17
38.16	15.633	-.509	1.187	1.374	.42	-.18
42.58	15.748	-.481	1.173	1.489	.45	-.20
51.32	15.937	-.480	1.158	1.678	.45	-.22

θ_e	log g	v_o	$(b-v)_o$	$(u-b)_1$	M_V^*	B-V	U-B
.875	1.60	15.852	-.458	1.345	1.593	.47	-.04
.875	2.82	15.887	-.468	1.175	1.628	.46	-.20
.875	3.80	15.911	-.463	1.078	1.652	.47	-.29
.775	1.60	15.188	-.685	1.270	0.929	.24	-.11
.775	2.82	15.246	-.645	1.152	0.097	.28	-.22
.775	3.80	15.285	-.605	1.058	1.026	.32	-.31
.638	1.60	14.350	-.930	1.182	0.091	-.01	-.19
.638	2.82	14.369	-.906	1.149	0.110	.02	-.23
.638	3.80	14.397	-.856	1.094	0.138	.07	-.28

*Using the equilibrium radius, 3434 units

Table IX

quantity	max	min	med	ampl	equil.
M_V	.25	1.77	1.01	1.52	.98
B-V	.03	.48	.26	.45	.28
U-B	-.31	-.17	-.24	.14	-.22

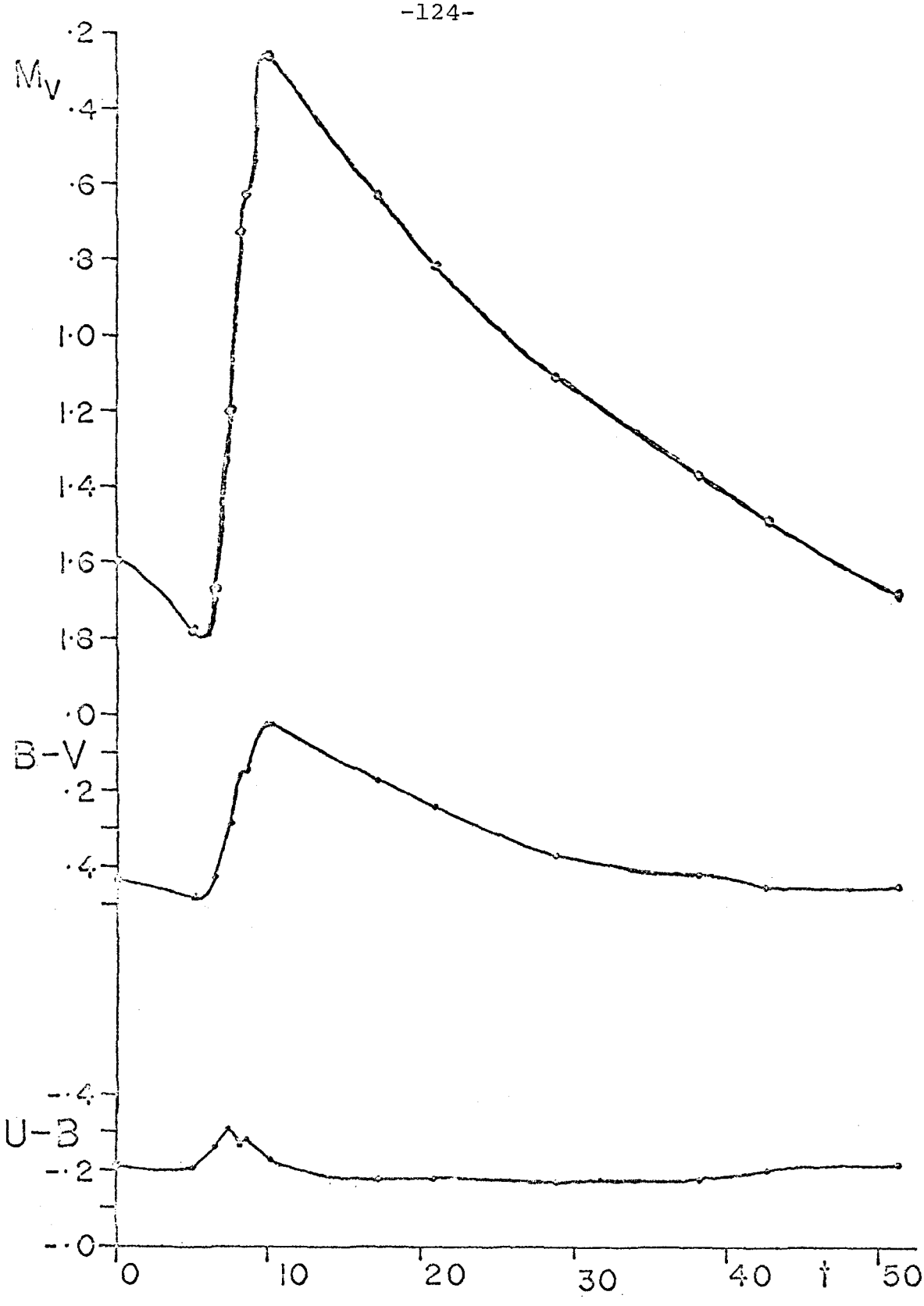

Figure 21. Computed three-color photometry for the model

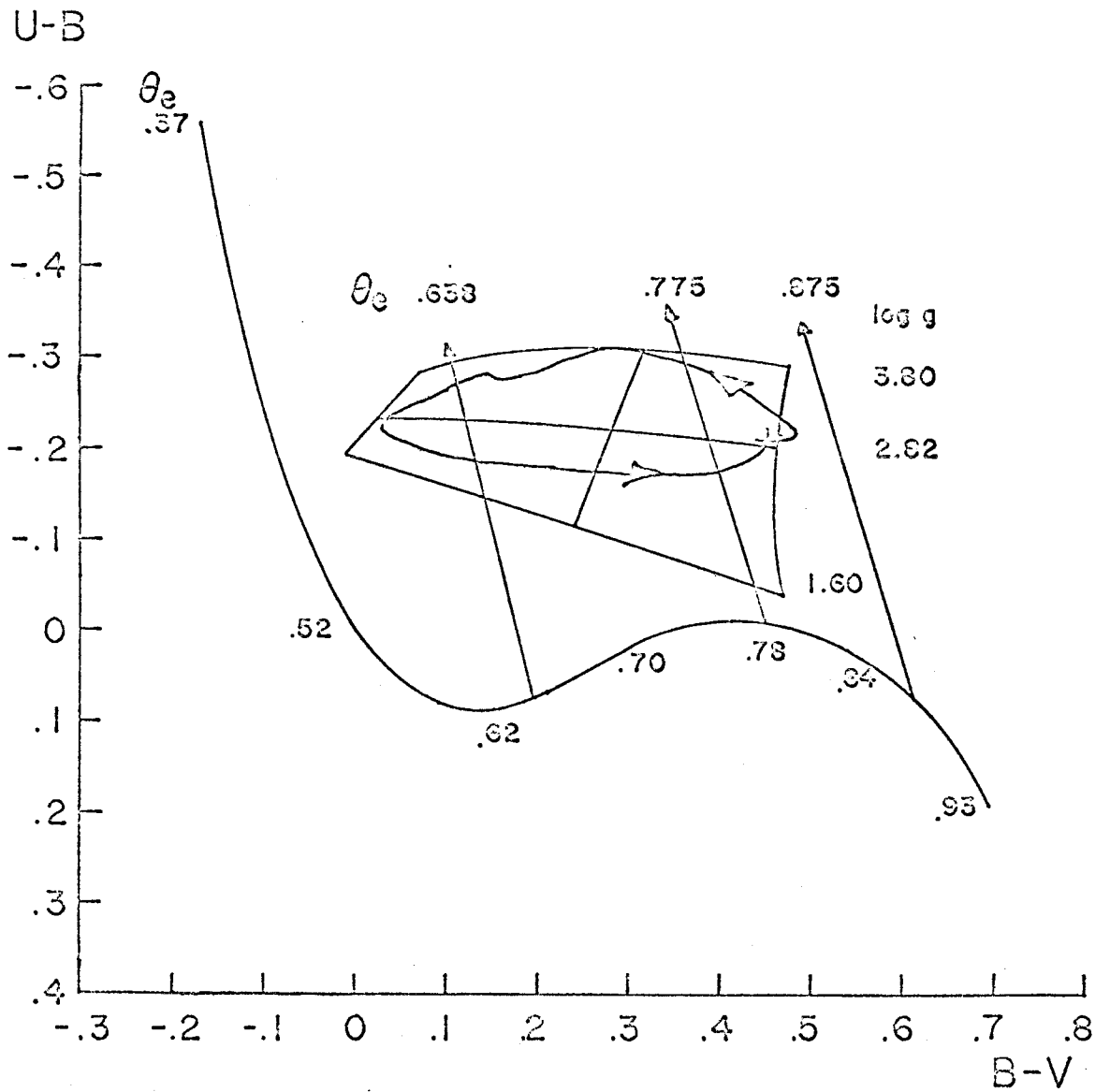

Figure 22. Two-color diagram showing the main-sequence relation, the grid of equilibrium model colors and the locus of the dynamical model. The arrows indicate how a main-sequence star would move if all lines were removed.

suggestion of Abt (1959) that shock-induced continuum emission is responsible for the presence of the loop. The dynamical calculations bear out the alternate hypothesis that all the continuum features are predictable from equilibrium models of appropriate temperature and gravity.

If not very much is said about phenomena in the line spectrum in this discussion, it is not because the subject would not be fruitful, on the contrary; but because first the information which can actually be obtained about lines from the model is rather qualitative, since the optical depth scale doesn't extend low enough with adequate resolution to give quantitative results; second, the behavior of very high layers in the atmosphere is extremely sensitive to the high frequency content of the pulsation, that is, that only a very well relaxed model could be used to describe these layers with any certainty.

If a shock did occur, raising material behind it to a temperature of 40,000 degrees or so, the opacity in $H\gamma$ would be so great that $H\gamma$ could be optically thick through less than 10^{-4} of the surface shell of the present model (Whitney and Skalafuris 1963), in other words the shock could occur many scale heights beyond the last mass shell considered in this calculation and still affect the Balmer lines. On the other hand,

because the velocity rise time is considerably more than the atmospheric resonance time C/g it is difficult to form a shock wave (barring the assistance of critical phenomena in the H zone) without allowing it to develop through several scale heights. Consequently H γ emission might or might not occur in this model, but it would require adding many more mass shells on the outside to actually find out.

B. Comparison with Properties of Actual Stars

Turning to a direct comparison of the model with actual RR Lyrae stars, Table X contains some parameters which can be reasonably be inferred from the observational data for the three well observed stars SU Dra, X Ari, and SW And[1], in addition to the equivalent data for the model. It is a misfortune of the disposition of RR Lyrae stars in the sky that all the stars brighter than 9^m at maximum have nearly the same amplitude, about 1^m. The data given here for the stars have been drawn from Preston (1964) and from the publications of Oke et al.

Using the observed periods and Christy's period gravity relation with a mass of $1.0 \times 10^9 = 0.5\ M_\odot$ the

1 RR Lyrae might have been included in this list except for the large 41 day period effects.

Table X

Star	SU Dra	X Ari	SW And	Model
Property				
Period	$^{d}.660$	.651	.442	.536
ΔV	$^{m}.98$	.98	.94	1.52
$\Delta(B-V)$	.31	.26	.34	.45
ΔU[1]	81 km/sec	71	83	91
g[2]	5.4 units	5.4	8.4	6.5
R	3600 units	3360	2250	3434
mass[3]	$1.04.10^{9}$ "	.93	.64	1.15
$\Delta R/R$	.16	.15	.18	.15
$\langle T_e \rangle$	6425°K	6550	(6600)	6500
$\Delta \phi$ rise[4]	.069	.070	.053	.059
g_{eff}[5]	20 units	18	41	40
$I(H\gamma_{em})/I_c$	.8:	1.1	.2:	?

[1] using $\langle \mu \rangle = 3/4$ as derived in Appendix E.

[2] from Christy's period-gravity relation.

[3] from the radius and the gravity.

[4] the period times the velocity amplitude divided by g_{eff}.

[5] the maximum slope of the velocity curve on the rising branch.

gravities are obtained as given. The values of the radii, obtained from Oke, yield the masses given. The integrations of the velocity curves together with the radii give the relative radius amplitudes. In view of the small mass and large radius amplitude obtained for SW And perhaps a larger radius ought to have been used, although clearly it should be less than that of the other stars as indicated by the larger gravity. All three stars have similar effective temperatures, within the error of the determinations, reflecting the similar amplitudes, and the temperature of the model is also the same. Judging by the temperature and radius, the model is quite like SU Dra or X Ari, except for having a larger mass, giving it a gravity intermediate between these stars and SW And.

Turning to the various amplitudes, the model obviously exceeds all these stars in visual and color amplitude. The velocity amplitude, however, is only slightly excessive, and the relative radius amplitude is comparable to the stars'. As a consequence the velocity to visual amplitude ratio is only 42 km/sec/mag instead of 61 as determined by Preston and Paczynski. Another parameter of interest is the rise time $\Delta\phi_{\text{rise}}$ of the velocity curve, defined as the velocity amplitude divided by the slope of the steepest part of the outward-acceleration section of the velocity curve, in terms of the period.

This is correlated with the gravity, so that the lower gravity stars have the longer rise times. Here the model resembles SW And more than the other stars. A closely related quantity is the intensity of emission, if any, in the H γ line during the rising branch. SU Dra and X Ari show strong emission and SW And very weak emission, according to Preston and Paczynski. As for the model, as far as the present calculations are able to predict the model would not show H γ emission. If this is true, the model would resemble SW And in this respect also.

As was commented before the surface gravity seems to be a sensitive parameter controlling the presence or absence of H γ emission. The best explanation for this is probably to be found in the I-front theory: If the gravity is too low, then the atmospheric density is low at the beginning of compression and there is likely to be a shock generated in order to compress the neutral material enough for D-front conditions to prevail. However, this theory will require constructing relaxed models with fine H zone structure before it can be verified.

In view of the apparent contradiction between the model results and the discussion of Preston, Smak and Paczynski (1965) regarding shock-produced Balmer continuum emission in RR Lyrae stars perhaps some comment on these authors' result is desirable. They find a correlation

between the amplitude Δ(U-B) of the U-B curve, as measured from its minimum to the value at minimum light, and corrected for the gravity effect by

$$\delta_{grav} = 0.7\,(\log g_{max} - 3.20)$$

and for differential blanketing, and the H γ emission strength. It is not clear why they chose the value 3.20, which seems excessive if it is supposed to be the gravity at minimum light. The effect is that δ_{grav} is too small by a factor 3, if a more reasonable value, 2.7 were used instead for the minimum light gravity. We can see from their Table 7 that, quite apart from δ(U-B), $\log g_{eff}$ is well correlated with $I(H\gamma)/I_c$ so that incorrect compensation for the gravity effect produces a correlation of Δ(U-B) with $I(H\gamma)/I_c$. The $\log g_{eff}$ correlation confirms what was said before: the star with the higher (mean) gravity has the shorter rise time and hence the higher $\log g_{eff}$, and this star has the smaller H γ emission. It seems fair to say that the existence of Balmer continuum emission has still not been proven in RR Lyrae stars.

If the curve of U-B versus time in Figure 21 is compared with Preston's and Paczynski's results for the singly periodic type a variables, it is seen that the agreement is qualitatively satisfactory, a substantial

peak in U-B being present at mid-rising light, which is not due to either differential blanketing or to Balmer continuum emission from a shock but merely to the high gravities which exist at that time.

Part IV. Convection and the Model Deficiencies

A. Discussion of the Amplitudes

The principal discrepancy with the observations is simply that the light amplitude is too large. Some of the other discrepancies, such as the shortness of the luminosity rise compared to the velocity rise, are in fact also related to this. It would seem that the hydrogen zone in the model is actually too efficient at retaining the flux during compression to allow favorable comparison with the stars. To see whether this might not be due to having chosen poor parameters for the model it is necessary to muster the systematic properties of RR Lyrae star amplitudes and compare them with the model grid of Christy.

The most useful observational data bearing on this point are the period-amplitude and color-amplitude relations for cluster RR Lyraes. Referring to Figure 4b, the color-magnitude diagram, of Roberts' and Sandage's study of M3 variables (1955), we see that they fall into two more-or-less distinct luminosity groups, each group having a dispersion of about $^{m}.05$. If the stars of each luminosity group are identified in the period-amplitude diagram, Figure 6, they are seen to form two parallel relations, the more luminous stars being shifted to higher periods. In the color-amplitude relation the

difference is largely removed, and the relation which exists can be considered to be the amplitude-temperature relation, since each luminosity group is probably homogeneous in mass and composition, in addition to luminosity.

If the maximum and minimum mean CI for the ab stars are converted to effective temperatures using the relations

$$B-V = CI + .19$$

$$\theta_e = .62 + .51(B-V)$$

the first given by Sandage (1959), and the second derived by Oke for SU Dra, the T_e range for ab stars is found to be 5970 to 6740 degrees, while c stars extend to 7130 degrees.

Figure 23 shows a comparison of the approximate locus in ΔM_{bol} and T_e of the ab stars in M3 with the Christy models in sequences 4, 5, 8, 9, which all have $M_{bol} = .76$ (close to the determinations for M3) and masses and helium contents as shown. Of all the sequences, number 5 gives the worst agreement with the M3 stars, and its lower mass equivalent, sequence 4, is also poor in this respect. The higher helium sequences 8 and 9 are much superior. These are ruled out, however, by the reasoning Christy employed in his discussion (1966a). If the abundance were 45 percent then the c's should extend to 7400 degrees. With a maximum T_e of 6750

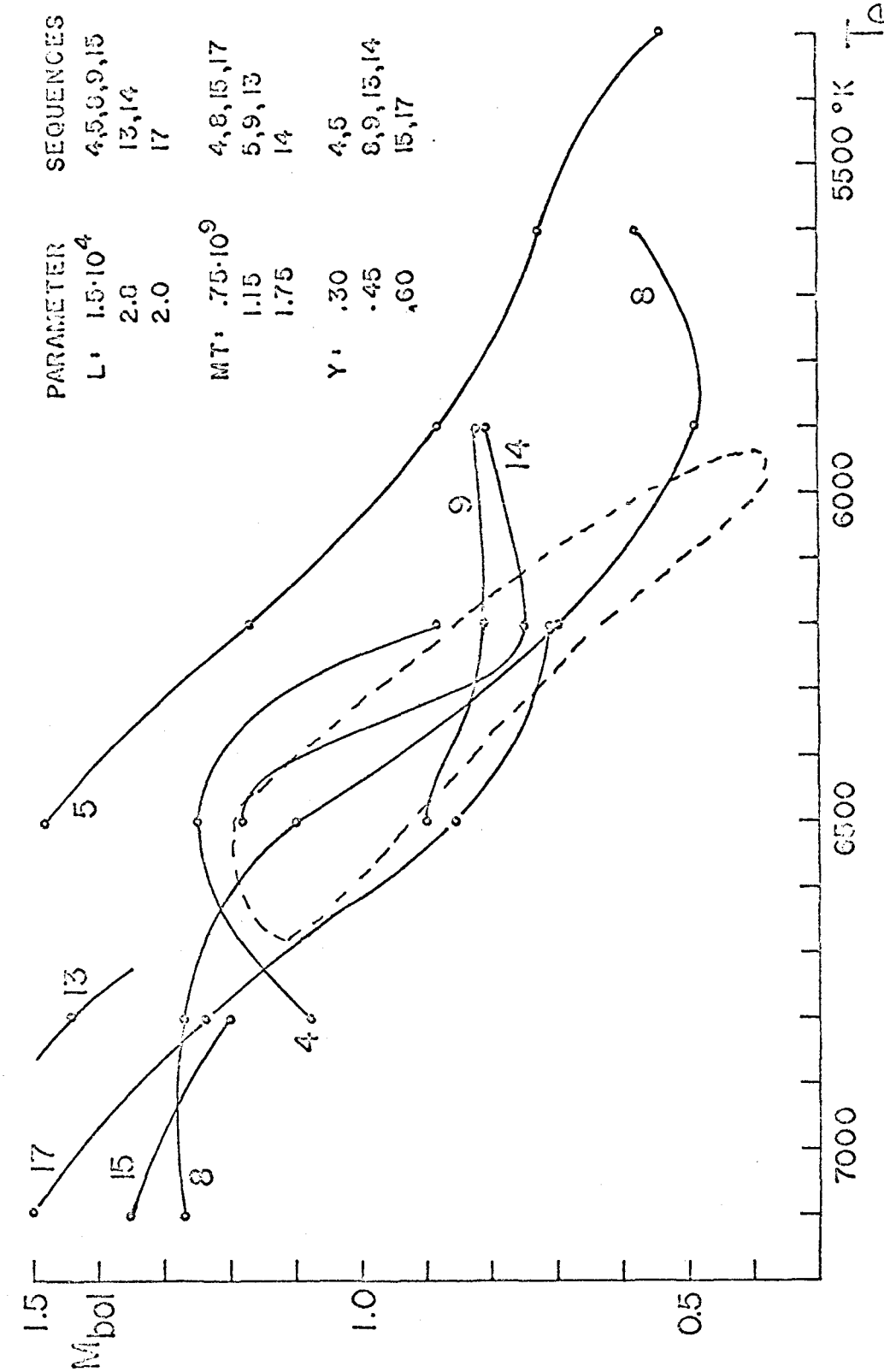

Figure 23. Bolometric amplitude - temperature relation. The area within the dashed line is occupied by M3 variables. The points are Christy models with the indicated parameters.

for the ab's the mass would be $.50M_{\odot}$. Since the c's do not appear to be hotter than 7100 degrees the helium abundance must be less. With 30 percent a reasonable representation of the temperatures of the c's and the ab's is found for $M = .58M_{\odot}$. This identification depends somewhat on whether the stars pulsate as c's or ab's in the crossover region. Thus this argument again leaves us with sequence 5. It should be noted that the exclusion of 45 percent is not altered if there is a range of masses, and that the convection uncertainties and the problems in finding the mean color are least important for the c's on which the argument rests. Also, if the temperature scale were shifted upward by 300°K then sequence 8 would no longer represent the M3 variables at all, and even more helium would be indicated.

Let's proceed then on the assumption that sequence 5 has the proper parameters to represent the M3 variables and try to understand why the amplitude is $^{m}.5$ too great, and why the models are unstable for temperatures which are far less than those of the observed stars. Compare in Christy's Table 3 the characteristics of models 5g and 9f , which differ only in helium content. The pulsation energy is the same, the radius and velocity amplitudes are 11 percent and 20 percent higher, respectively, for 5g, but both are similar to the observed values. The bolometric magnitude amplitude is 1.48 for

5g compared to .90 for 9f, however. Finally, we see that the He zone work is similar (.020 for 5g to .022 for 9f) while the H zone work is 3 to 1 in favor of 5g (.015 to .0058). The inference from this is that the increase in ΔM_{bol}, at least, in 5g is the result of the greater work production in the H zone. Extrapolating this conclusion to lower T_e's we expect that a surplus of H zone work production is responsible for the instability of sequence 5 where the observations indicate stability. The most likely factor to limit hydrogen zone work production, especially at low temperatures, is convection.

B. Convection in the RR Lyrae Models

The rate of energy transfer through a sphere by convection can be written as

$$4\pi r^2 \langle \rho v_r h \rangle$$

where v_r is the radial component of the turbulent velocity and h is the specific enthalpy, assuming that the kinetic energy and the pressure fluctuations are negligible. In a linear theory an upper bound to the flux per unit area is

$$\frac{1}{2} \rho v_r \delta h$$

where v_r and δh are semi-amplitudes. If as upper bounds to v_r and δh we use $1/2 c_s$ and $1/2\ \chi$, where c_s is the sound speed and χ is the ionization energy, we have

$$F \leq 1.6 \cdot 10^{-5} \text{ units}$$

while the total flux is 1.0×10^{-4} units. Thus convection would represent 16 percent of the total flux in the equilibrium model in the H zone, a figure comparable to that which Christy gives in Table 2 of (1966a).

The next question is the behavior of convection during pulsation. The characteristic time of the convection cells is one scale height divided by the sound speed, or equivalently the sound speed divided by the gravity. In the equilibrium model the convection time to the period is as the sound time across one scale height to the sound time from center to surface, that is, much less than 1. Specifically the time for model 5g at equilibrium is

$$t_c = \frac{c_s}{g} = \frac{10}{6.5} = 1.5 \text{ units}$$

while the period is 46.35 units. During the expansion phase g is as small as 2 making t_c as large as 5 time units. However due to the low densities, convection is not likely to be important then. During the compression phase g is essentially dU/dt where U is the photosphere velocity, so t_c is the time required for U to change by c_s. Since in general U changes by 7 to 10 times c_s, the duration of the compression phase is that many times the convection time. The conclusion is that

convection should be able to adjust to the higher density existing during compression. This density exceeds the equilibrium density by a factor of 5 or more, making convection very competitive with radiation, perhaps dominant.

We see then that in perhaps most of the Bailey ab stars convection operates effectively as a mechanism for transporting heat during compression, when radiative transfer is much impeded, and ineffectively during expansion, when radiation is efficient. Thus it just counteracts the effectiveness of the H zone driving mechanism, which is the necessary conclusion to explain the excessive amplitudes and the instability at low temperatures which contradict the observations.

Other than to reduce work production in the hydrogen zone it is not really possible to tell what effect convection will have on the pulsation without actually making models including it. One effect would probably be to make the luminosity rise more gradual, in accordance with the observations. Whether it would also produce the more pronounced stillstand on the rising branch is impossible to tell.

Parenthetically, if the scale height were not small compared to the radius as is the case in RR Lyrae stars, and if on the rising branch the atmosphere did not respond quasi-hydrostatically to compression, which

follows from the first condition, then convection might not adjust to the pulsation, and much cooler models could be unstable because of the H zone mechanism. As Baker and Kippenhahn have found, convection which does not interact with the pulsation does not prevent hydrogen zone driving. The stars which are in mind in this connection are the red giant and K supergiant variables in which instability in fact seems to be very common. But for the higher gravity RR Lyrae stars it would appear that convection does exist and does interact with pulsation and does limit the amplitude and establish the low T_e boundary of instability.

In order to see how convection would change the determinations of temperature and gravity, three equilibrium models including the effects of convection were constructed, using the values of θ_e and log g which applied in the models at t = 7.47, 9.56 and 38.16. These models represent maximum compression, maximum temperature and a typical phase on the lower descending branch. An additional model might have been constructed for 20.87 but convection would be actually negligible in it due to the very low pressure in the H zone.

The method used to construct the models is the same as described by Mihalas (1966b) for the first

approximation used by him in obtaining constant flux models. As before the Rosseland mean was used as the standard opacity, rather than $\mathcal{K}_{5000}$. These models assume the gray temperature distribution until convection begins, then find the temperature distribution by keeping the sum of radiative and convective flux constant, where the diffusion equation is used for the radiative flux and the mixing length theory with $\ell/H = 1$ including radiative losses is used for the convective flux. Under certain circumstances the convective flux may exceed the upper bound given earlier, but the radiative losses prevent the excess from being ridiculous; in any event the models indicate what convective effects can be expected.

The results are given in Table XI. The maximum amount of convective flux and the maximum convective velocity are given, together with the details of the slope and Balmer jump fit as before. We see that the errors made in assuming that the models are radiative are of the same order of magnitude as the radiative equilibrium deviations found before, but here they are always toward lower temperatures and higher gravities, which is what is expected from a reduction in the temperature gradient. These effects should be largest during compression and disappear just after maximum light, so that they introduce

Table XI

t	7.47	9.56	38.16
θ_e	.769	.640	.850
log g	3.69	3.12	2.55
C	-.457	.120	-.689
D	.499	1.358	.453
θ_e*	.775	.645	.857
log g*	3.84	3.12	2.77
$\Delta\theta$	.006	.005	.007
Δlog g	.16	0	.22
$(F_c/F_o)_{max}$	.95:	.22	.97:
$(v_t)_{max}$	3.4 km/sec	6.7	4.2
∇_{max}	2.36	3.45	3.75

systematic errors as a function of phase in the radius determinations, if these are based on radiative models.

C. Other Limitations and Inaccuracies

The most serious limitations on the usefulness of the model that was made in this study are those which have already been discussed: lack of relaxation and omission of convection. There are other problems, some of which are probably not important for this type of star, which in any case must be examined and rectified if possible in future work.

One of these, which was actually troublesome here, is the availability (or lack thereof) of opacities for both the interior and the atmosphere which are accurate and consistent. For the envelope dynamical calculation Christy's analytical approximation to the Cox opacity tables was used, whereas for the atmospheres the Mihalas monochromatic opacity routines were used. These are not consistent, in fact, and in addition neither agrees exceptionally well with the published Cox values, which are to be preferred.

Table XII shows a comparison of some of the available opacities at several sample points. In the first part of the table the Cox, Stewart and Eilers (1965) opacities for the Aller mixture are compared with Mihalas-

Table XII

log χ_{Ross}:

Source		Cox		Mihalas	Mihalas	Vardya	Vardya
Y		.384		.354	.300	.326	.333
Z		.020		.044	.002	.022	.002
θ,	log p_e	lines					
1.0	-1.	-2.538	20%		-2.450	-2.481	-2.470
1.0	0.	-1.591	10		-1.538	-1.573	-1.554
1.0	1.	-0.558	16	-0.639	-0.601	-0.600	-0.612
1.0	2.	0.468	15	0.307	0.082	0.314	0.064
0.8	-1.	-1.372	3		-1.309	-1.328	-1.321
0.8	0.	-1.591	8		-1.510	-1.535	-1.527
0.8	1.	-0.854	13	-0.879	-0.817	-0.852	-0.842
0.8	2.	0.209	20	0.004	0.079	0.028	0.041
0.4	4.	2.212	17		2.012	1.992	2.000

for Y = .384, Z = .020

θ	log p_e	log V	log χ_{Cox}	log χ_{form}	Δlog χ
1.	0	7.27	-1.591	-1.612	-.021
.6	3.	6.80	0.908	1.004	.096
.2	4.	8.16	0.836	0.876	.040
.101	5.494	6.00	2.487	2.308	-.179

program-generated Rosseland mean opacities for the Kippenhahn I mixture (which is about the same) and for the composition used here, and with Vardya (1964) values for a composition similar to the Aller mix and one similar to the mixture used here. The percentage effect of lines on the Cox opacities is also indicated. The consensus is that Mihalas agrees with Vardya to $\pm$ 3 percent. Vardya agrees with Cox to 5 to 10 percent except where lines are most important, the errors there rising to 50 percent. The second part compares Cox opacities for the Aller mix with opacities calculated with Christy's formula at four selected points. The electron pressures used in the formula were derived from Cox's tables. It would seem that overall the formula agrees with the table to 10-20 percent, although at the highest temperature the difference is larger. At $\theta_e = .4$ and $\log p_e = 4$, where the line effects are large, the formula gives $\log \chi = 2.014$, which lies midway between Mihalas and Vardya on the one hand and Cox and Stewart on the other, differing by 25 percent from each.

Rather than using a formula it would probably be better to interpolate more or less directly in the table. It would be desirable, of course, if accurate values could by obtained for low Z, high Y compositions which are lacking at this time. Since it is inaccurate

to use low order interpolation in the course grid of temperature and density given by Cox and Stewart, it would be desirable to first refine the grid with high order interpolation, then obtain opacities as required with linear interpolation in the denser grid.

Another problem to consider is the deviation from planarity of the atmosphere. If a measure of that deviation is the ratio of the atmospheric scale height to the radius, we can see that this parameter is identical to the convection time compared to the period, and we have already seen that that is small for RR Lyrae stars, although it is probably not small for the cool variables. In the present model at maximum expansion the extent of the atmosphere from $\tau = 10^{-3}$ to $\tau = 1$ is 34 units while the radius is 3728 units, so the ratio is 0.91 percent, which is obviously negligible.

It should be pointed out that the approximation to sphericity that was incorporated in the integral expression for $\partial L / \partial M$ leads to an incorrect equilibrium temperature distribution at small optical depth in a very extended atmosphere. The argument of Chapman (1966) using moments of the transfer equation leads to the asymptotic source-function

$$J \sim H(1+\tau) = \frac{L}{16\pi^2 R^2}(1+\tau)$$

The formula used here leads to

$$J = \int_0^\tau 3 H d(\tau + q(\tau))$$

Taking the case $\kappa\rho \sim 1/r^3$ the correct expression for small tau is

$$J \sim \frac{1}{r^2}(1+\tau) = O(\tau)$$

while the other formula would have approximately

$$J = O(\tau \log \tau).$$

It is clear that the approximation becomes erroneous in a very extended atmosphere. The problem of extended atmospheres is one which must be solved before atmospheric phenomena in the cool variables can be investigated.

The question of including frequency dependence in handling radiative transfer has an importance limited to atmospheric problems, since the Rosseland mean treatment is accurate in optically thick material. Even in the atmospheres non-gray effects are not severe in cool stars, due to the importance of H^- in the opacity. The most likely circumstance requiring a non-gray treatment in pulsation is a strong photospheric shock, as indicated by Whitney and Skalafuris (1963). Since the cost of calculation is proportional to the number of independent frequency intervals, this improvement is not likely to be

made soon.

Finally some thought should be given to the truncation error of the difference system. As far as the equation of motion and the diffusion equation are concerned there is little to be added to what was said by Christy (1964). In the present calculations $\Delta \ln(MT-M_r)$ was 0.5 which is worse than the value 0.34 used by Christy. The large spatial steps do not affect the energy balance because of the way the difference equations were set up, but do mask short wavelength phenomena such as shocks (or ionization fronts). Furthermore near the center where the step in radius becomes large the variation of velocity from point to point can be substantial, no doubt causing errors. Because the amplitude is small in this region, however, the effect on the pulsation should be slight. The same reasoning applies to the location of the rigid inner boundary in the present case at 25 percent of the exterior radius. The sound travel time from the center to the surface would lengthen by about 4 percent if the inner boundary were much closer to the center. This could very well change the harmonic composition of the pulsation.

Regarding the accuracy of the quadrature formula for the optically thin region, a test case was calculated in which the flux was found as a function of optical depth, using a similar formula and perhaps 20 percent more points,

for the exact gray body solution. The answers were correct to about 0.5 percent in the mean.

Two other error sources are the adiabatic pressure extrapolation and the interpolation when changing the mass division. The latter caused errors of only a few percent in any variable, while the former might make the H zone pressures 10 percent in error locally.

Conclusion

To what extent do the results achieve the objectives of this enterprise? To begin with, a relaxed model containing the full physical treatment outlined in the introduction could not be obtained, for economic reasons. The hope that aperiodicities present in the one or two cycles which could be calculated could be minimized by using a well relaxed diffusion model for initial conditions was not well realized either. The inference is that the additional accuracy of the physical description used in this model did have significant consequences, and it was of some interest to investigate these. However, due to the transient reaction to the difference the actual results of the model calculation must be considered preliminary in that agreement or disagreement of the calculations with the overall behavior of a star may not be significant. What the calculations do provide is a model of the possible behavior of an RR Lyrae star. Specific features of the calculations which agree with observations can be used in the regular way to give insight into the mechanisms operating in the stars.

In my opinion the most interesting phenomena which appeared in the calculations are those connected with the motion of the H-zone. It has become my impression

after analyzing the results that many surface features are caused by H-zone dynamics. I have already discussed the connection of the H-zone with rising-branch shocks through the reaction to M-front conditions and through the dependence of the pre-rise atmospheric state on the H-zone-connected behavior on the descending branch. It is also possible to see a connection between the shape of the descending (i.e. inward acceleration) branch of the velocity curve, and the existence of the R-front, which disappears at the midpoint of the branch, and the subsequent compression waves in the atmosphere. The description of these events is not reliable in the absence of fine H-zone resolution in the model. More extensive calculation of this type will surely be helpful in interpreting and calibrating the observed velocity (and luminosity) curves.

The results of the calculation which could be compared with Christy's model in all cases compared favorably. In particular the hydrogen zone work production was the same as Christy found it to be.

The deviations from radiative equilibrium in the optically thin layers, which the transfer formulation was used to describe, are quite sensitive to the fluctuations in dynamical quantities and therefore were severely affected by the lack of relaxation. The extent of the dev-

iations which occurred indicated that while they are not a dominant effect they are significant and probably will help explain some anomalies in the radius-curve determinations.

The energy distributions calculated with the models are qualitatively the same as the observed distributions but quantitatively they indicate, by large amplitudes and shorter rise times, excessive efficiency of heat retention by the H-zone.

These differences cannot be ascribed to lack of relaxation or to errors in the parameters chosen for the model, and must rather be due to some lacking or erroneous ingredient in the models. The indications are that this ingredient is convection.

I think this calculation has been productive in indicating directions in which to proceed in achieving better explanation of the features of RR Lyrae stars. The most important thing which should be done next is the calculation of relaxed models including fine H-zone detail and convection; these need not include transfer effects which are likely to become significant only after the amplitudes and general appearance of the observations are reproduced by the models. The form which convection should take in the models is of secondary importance; more important is the calculation of a sufficient number of models including

a plausible representation of it to see what can be expected from more careful work.

Appendix A. Symbols

Symbol	Interpretation
A_i	$8\pi^2 \partial\tau/\partial M_r$
C or C_s	adiabatic sound speed
C_i	source function gradient less gray value
C_Q	pseudo-viscosity constant
C_V	specific heat at constant volume
DLGDM1	normal increment in M1
DM1	mass of a shell
DM2	mass associated with a sphere
DTAU	optical depth increment between shell centers
DTAU1	optical depth increment across a shell
E or e	internal energy
f_{ij}	kernel in sum for $\partial L/\partial M$
F	energy flux per unit area
G	gravitational constant
h(x)	x + q(x), the gray body source function
$I(\mu)$	specific intensity of radiation
K	diffusion constant
L_r or L	luminosity at radius r
LT or L_o	luminosity of static model
M_r or M or MO_i	mass interior to radius r
M_i	$\log_e$ of mass exterior to the midpoint of a shell
$M1_i$	$\log_e$ of mass exterior to a sphere

Symbol	Interpretation
MT or M	total mass of the star
N	total number of shells
N(x)	function used to choose optical depth scale, $= 5.78\ln(1+5.78\ln(1+.5x))$
p	pressure
q	pseudo-viscous pressure
q(x)	function appearing in gray body source function
r or R	radius variable
R or RT	photospheric radius
RR	$r^2 S(\tau)/h(\tau)$ at $\tau = 0$
$\mathcal{S}$	specific entropy
S	source function (blackbody function), $= \frac{\sigma}{\pi} T^4$
t	time
T	temperature
TAU or τ	optical depth at the midpoint of a shell
TAU1 or $\tau 1$	optical depth at a sphere
U	velocity
V	specific volume, $= 1/\rho$
χ	opacity
μ	direction cosine of radiation to line of sight
ρ	density
σ	Stephen-Boltzmann constant
χ	ionization energy
$\chi(x)$	$\int_{-\infty}^{x} E_3(\lvert x \rvert)dx$

Appendix B.

Exponential Integral Approximations

The flux formulae require values of $E_2(x)$, $E_3(x)$, and $E_4(x)$. Since many evaluations of these are required, rational approximations had to be found. From the definition,

$$E_n(x) = \int_1^\infty \frac{e^{-xt}\,dt}{t^n}$$

the asymptotic expansion

$$e^x E_n(x) \sim \frac{1}{x}\left(1 - \frac{n}{x} + \frac{n(n+1)}{x^2} - \frac{n(n+1)(n+2)}{x^3} + \cdots\right)$$

can be derived (Abramowitz and Stegun 1964), which suggests a rational approximation of the form

$$e^x E_n(x) \doteq \frac{P_r(x)}{Q_{r+1}(x)}$$

where P_r is a polynomial of order r, Q_{r+1} a polynomial of order r+1. The coefficients were determined according to the method of Hastings (1955) to minimize the absolute error in $e^x E_n(x)$. The results for E_3 and E_4 are

$$e^x E_3(x) = \frac{a_0 + a_1 x + a_2 x^2}{b + b_1 x + b_2 x^2 + b_3 x^3} \pm 6.66 \times 10^{-5}$$

$$a_o = .49993344 \qquad b_1 = 6.0160198$$
$$a_1 = 2.5278369 \qquad b_2 = 5.9324547$$
$$a_2 = 1.1897942 \qquad b_3 = 1.1969649$$

$$e^x E_4(x) = \frac{a_o+a_1x+a_2x^2}{1+b_1x+b_2x^2+b_3x^3} \pm 3.66 \times 10^{-5}$$

$$a_o = .33331891 \qquad b_1 = 2.5767983$$
$$a_1 = .69333060 \qquad b_2 = 1.4134852$$
$$a_2 = .18408381 \qquad b_3 = .18466785.$$

In addition to E_3 and E_4, E_2 and E_3 must be computed at the same time, respectively. The expressions used for these are

$$\frac{E_2(x)}{E_3(x)} = \frac{1+1.3455964x}{.51368752+1.2469102x} \pm 0.014$$

and

$$\frac{E_3(x)}{E_4(x)} = \frac{1+.67682642x}{.67085261+.64670958x} \pm .0042$$

All these rational fractions are expressed as finite continued fractions for computational efficiency when they are actually evaluated.

The gray body source function $h(x) = x+q(x)$ was approximated in the same way, with the result

$$h(x) = x + .70998880 - \frac{.13263853 + 2.534451 1x - .60569702x^2}{1 + 28.269877 + 69.458442x^2 + 75.459271x^3}$$

$$\pm 4.6 \times 10^{-4}$$

and $$h'(x) = 1 + \frac{1.189}{1+36.84x} \quad .$$

Appendix C. Equation of State

Assembled below are the formulae used to define the thermodynamic state of the stellar material. If N(I,J) is the number density of element I in ionization stage J, the Saha equation gives

$$\frac{N(I,J)}{N(I,J-1)} = \frac{1}{N_e} T^{3/2} e^{-\chi_{I,J-1}/kT} \left[2\left(\frac{k m_e}{2\pi \hbar^2}\right)^{3/2}\right] \frac{g(I,J)}{g(I,J-1)}$$

where the symbols have their standard meanings, g(I,J) being the partition function replaced by the ground state statistical weight. With the definitions

$$C = 2\left(\frac{k m_e}{2\pi \hbar^2}\right)^{3/2}, \qquad C_1 = \frac{C T^{3/2}}{N_e}$$

$$CHI(I,J) = \frac{1}{k} \sum_{K=1}^{J-1} \chi_{I,K}$$

then

$$GN(I,J) = \frac{N(I,J)}{\sum_J N(I,J)} = \frac{C_1^{J-1} g(I,J) e^{-CHI(I,J)/T}}{\sum_J C_1^{J-1} g(I,J) e^{-CHI(I,J)/T}}.$$

The entropy per unit volume of species (I,J) is

$$N(I,J)k\left[2.5 + \log g(I,J) + 1.5 \log T - \log N(I,J) + GLC(I)\right]$$

where

$$GLC(I) = \frac{3}{2} \log\left(\frac{k m(I)}{2\pi \hbar^2}\right)$$

and m(I) is the atomic mass of element I. If X(I) is the number abundance fraction of element I, the mean

molecular weight of the neutral mixture is

$$\mu_N = \sum_I A(I)\, X(I)$$

where A(I) is the atomic weight of element I in amu. So that the number per unit mass of (I,J) is

$$\frac{N_o}{\mu_N} X(I)\, GN(I,J)$$

where N_o is Avogadro's number; therefore the number per unit volume is

$$N(I,J) = \frac{\rho N_o}{\mu_N} X(I)\, GN(I,J)$$

and furthermore the electron density is

$$N_e = \frac{\rho N_o}{\mu_N} \sum_I X(I) \sum_J C(I,J)\, GN(I,J) = \frac{\rho N_o}{\mu_N} \cdot A$$

where C(I,J) is the charge of ion (I,J). The total entropy per unit mass, then, including the electrons is

$$S = \frac{N_o k}{\mu_N} \left\{ \sum_I X(I) \left[GLC(I) + \sum_J GN(I,J) \cdot \right.\right.$$

$$\left. \cdot (\log g(I,J) - \log N(I,J)) \right] + 2.5 + 1.5 \log T$$

$$\left. + A \cdot (2.5 + \log C_1) \right\}$$

where $N_o k$ is the same as the gas constant R. The pressure and internal energy per unit mass are

$$p = \frac{\rho k T}{\mu_N} (1 + A)$$

and

$$E = \frac{kT}{\mu_N}\left\{1.5(1+A) + \frac{1}{T}\sum_I{}' X(I)\sum_J{}' CHI(I,J)GN(I,J)\right\}.$$

If we define F and G by the following expressions

$$F = \sum_I{}' X(I)\left\{\sum_J{}' C^2(I,J)GN(I,J) - \left(\sum_J{}' C(I,J)GN(I,J)\right)^2\right\}$$

$$= \left\langle \left\langle C^2(I,J)\right\rangle_J - \left\langle C(I,J)\right\rangle_J^2 \right\rangle_I$$

$$G = \left\langle \left\langle C(I,J)CHI(I,J)\right\rangle_J - \left\langle C(I,J)\right\rangle_J \left\langle CHI(I,J)\right\rangle_J \right\rangle_I$$

then

$$\left(\frac{\partial \log N_a}{\partial \log T}\right)_\rho = \frac{1.5F + G/T}{1+A}$$

$$\left(\frac{\partial \log N_e}{\partial \log \rho}\right)_T = \frac{A}{F+A}$$

$$\left(\frac{\partial \log P}{\partial \log T}\right)_\rho = 1 + \frac{A}{1+A}\left(\frac{\partial \log N_e}{\partial \log T}\right)_\rho$$

$$\left(\frac{\partial \log P}{\partial \log \rho}\right)_T = 1 - \frac{A}{1+A}\frac{F}{F+A}$$

and if we define

$$DLNFAC = 1.5 - \left(\frac{\partial \log N_e}{\partial \log T}\right)_\rho$$

then

$$\left(\frac{\partial \log N(I,J)}{\partial \log T}\right)_\rho = DLNFAC \cdot C(I,J) + CHI(I,J)/T$$

$$- \sum_J{}' \left(DLNFAC \cdot C(I,J) + CHI(I,J)/T\right) GN(I,J) = DN(I,J).$$

Therefore the specific heat per unit mass at constant volume is

$$C_V = \frac{k}{\mu_N}\left\{1.5\left[1+A\left(1+\left(\frac{\partial \log N_e}{\partial \log T}\right)_\rho\right)\right] + \frac{1}{T}\left\langle\left\langle CHI(I,J)\,DN(I,J)\right\rangle_J\right\rangle_I\right\}.$$

The other common thermodynamic quantities all follow from these:

$$C_p = C_V + \frac{p}{\rho T}\,\frac{\left(\frac{\partial \log p}{\partial \log T}\right)_\rho^2}{\left(\frac{\partial \log p}{\partial \log \rho}\right)_T}$$

$$\Gamma_1 = \left(\frac{\partial \log p}{\partial \log \rho}\right)_S = \frac{C_p}{C_V}\left(\frac{\partial \log p}{\partial \log \rho}\right)_T$$

$$C_S = \sqrt{\frac{\Gamma_1 p}{\rho}}\,.$$

When radiation pressure is included (it was, in the present calculations) the following corrections are made:

to	add
p	$\frac{1}{3}aT^4$
s	$\frac{4}{3}\frac{aT^3}{\rho}$
E	$\frac{aT^4}{\rho}$
C_V	$\frac{4}{3}\frac{aT^3}{\rho}$

and the other corrections may be inferred.

In these calculations the given arguments were usually T and ρ and N_e was adjusted by iteration to

satisfy the equation for ρ. The relative abundances of the heavy elements used are given in Table C.I as adopted from Mihalas (1965a). For each of these three ionization stages were treated explicitly and the remainder were handled statistically.

After the electron pressure had been found for the given temperature and density Christy's formula was used to give the opacity (1966a).

This procedure was used to construct a table giving $\ln(\chi)$, $\ln(p)$, ρ, (C_s^2/T) with $\ln(T)$ and $\ln(V)$ as arguments. The region of $\ln(T)$ and $\ln(V)$ covered by the table was diagonal in shape, the range in $\log_{10}V$ being 3.0 at each T but with the upper and lower limits varying with T, so that roughly $V \sim 1/T^3$. The table spacing in $\log_{10}V$ was 0.3 and in $\log_{10}T$: .02 for $-.3 \leqslant \log_{10}(T/10^4 \cdot K) \leqslant 1.0$, .05 outside that range.

In the dynamical calculations (including the equilibrium model) χ, p, ρ, and C_s were obtained by interpolation in the corresponding table linearly versus lnT and lnV. Where lnp and lnT were the given arguments inverse interpolation was used to obtain lnV, and then the other interpolations proceeded as in the other case. Whenever derivatives were required they were obtained by differencing in the tables. Linear extrapolation was used whenever the arguments fell outside the table.

Table C.1

Z	Element	Relative Abundance (by number)
6	C	.3266
7	N	.05923
8	O	.56086
11	Na	.00123
12	Mg	.01541
13	Al	.00098
14	Si	.01972
16	S	.01233
20	Ca	.00086
26	Fe	.00228
28	Ni	.0005

Appendix D. The System of Units

Following Christy the system of units used in the calculations and which has been found quite useful for general computation in RR Lyrae stars is the cgs system modified by powers of 10 to make certain quantities take on convenient values. The following table summarizes the relation to the cgs system.

Quantity	cgs unit	unit in modified system
length	1 centimeter	10^8 cm
mass	1 gram	10^{24} gm
time	1 second	10^3 sec
velocity	1 cm/sec	10^5 cm/sec
density	1 gm/cm^3	1 gm/cm^3
pressure	1 erg/cm^3	10^{10} erg/cm^3
energy	1 erg	10^{34} erg
power	1 erg/sec	10^{31} erg/sec
gravitational constant	1 cm^3/gmsec^2 (G=6.70x 10^{-8})	10^{-6}cm^3/gmsec^2 (G=.067)
flux	1 erg/cm^2 sec	10^{15} erg/cm^{2}sec
temperature	1°Kelvin	10^4 °K
specific heat, entropy	1 erg/gm°K	10^6erg/gm°K
Stephan-Boltzmann Constant	1 erg/cm^{2}sec(°K)^4 (σ=5.6692x10^{-5})	10^{-1}erg/cm^{2}sec(°K)^4 (σ=5.6692x10^{-4})
specific energy	1 erg/gm	10^{10} erg/gm

1 day is 86.4 time units, 1 km/sec is 1 velocity unit, the specific energy to ionize hydrogen is 1302.54 (km/sec)^2.

Appendix E. The Velocity Projection Factor

If a spectral line is formed in an atmosphere expanding radially with a velocity U, and if in the absence of expansion the observed profile can be represented by

$$e^{-\frac{1}{2}\left(\frac{\Delta\lambda}{\Delta\lambda_D}\right)^2}, \quad \Delta\lambda_D = \frac{\lambda U_D}{c}$$

then if the continuum limb darkening and the center-limb variation of the line strength are known, the profile that one would expect to observe from the expanding atmosphere can be computed. This profile will have a maximum at a displacement corresponding to a velocity $-\mu_{max}U$, and this velocity is close to what a person measuring the spectrum would call the radial velocity. A slightly better approximation would be the velocity at the midpoint of the chord drawn through the profile at 80 percent of maximum, for example, but this makes very little difference.

With a limb-darkening law

$$\frac{I(\mu)}{I(1)} = 1 - k(1-\mu)$$

and a center-limb variation law

$$\frac{W(\mu)}{W(1)} = 1 - a(1-\mu)$$

profiles and values of μ_{max} were computed corresponding to

$$k+a = 0.2,\ 0.6,\ 1.0$$

$$ka = \pm 0.1$$

and for

$$\eta = 0.5,\ 1.0,\ 2.5,\ 3.5,\ 5.0,\ 10.0\ ,$$

where

$$\eta = \frac{u}{v_D}\ .$$

The results are given in the following table.

Table E.I

μ_{max}

η	$k+a$ / ka	.2 / -.1	.2 / .1	.6 / -.1	.6 / .1	1.0 / -.1	1.0 / .1
0.5		.685	.675	.716	.703	.760	.742
1.0		.688	.678	.719	.706	.762	.745
2.5		.707	.698	.738	.726	.774	.762
3.5		.728	.719	.756	.747	.787	.778
5.		.762	.755	.785	.779	.808	.803
10.		.839	.836	.851	.849	.863	.861

To determine the limb darkening, values of $I(\mu)$ were calculated for each dynamical model atmosphere which was constructed as described in Part III. The results for k at 4475Å , were, for example,

equilibrium	.78
t = 5.02	.78
10.06	.70
38.16	.83 .

The values of a to be expected could be positive or negative and perhaps .25 in magnitude, but for the purpose here it is probably best to merely use 0. So for k = .78 and a = 0 we find the following table by interpolation

η	μ_{max}
.5	.728
1.0	.730
2.5	.748
3.5	.766
5.	.792
10.	.855 .

The contributors to v_d, the line width expressed as a velocity, are the thermal velocity, which is only about 1 or 2 km/sec for metal lines, the micro-turbulent and rotation velocities, which are typically 10 km/sec, and the resolution of the spectrograph expressed as a velocity, which is about 1.4 d where d is the dispersion in A/mm. Consequently, v_d is about 10 km/sec for 5 A/mm or less, about 17 km/sec for 10 A/mm, and 28 km/sec for 20 A/mm. With a value of U of 40 km/sec, which is representative of RR Lyrae stars, the values of η are 4, 2.3, and 1.4. The corresponding values of μ_{max} are .77, .75, and .73.

From this it would seem that the best (and simplest) projection factor to use is 3/4, although uncertainties of 2 percent or so seem to be inevitable because of the number of variable determining factors. For comparison the value usually used, which refers to the centroid of the profile for $k = 0.6$, $a = 0$, and is independent of line width, is $17/24 = .708$.

List of References

Abramowitz, M. and Stegun, I. A. ed. 1964, Handbook of Mathematical Functions (Washington: National Bureau of Standards).

Abt, H. 1959, Ap. J., 130, 824.

Baker, N. and Kippenhahn, R. 1962, Zs.f.Ap., 54, 114.

_____. 1965, Ap. J., 142, 868.

Chapman, R. D. 1966, Ap. J., 143, 61.

Christy, R. F. 1964, Rev. Mod. Phys., 36, 555.

_____. 1966a, Ap. J., 144, 108.

_____. 1966b, Ann. Rev. Astr. and Ap., 4, (in press).

Courant, R. and Friedrichs, K. O. 1948, Supersonic Flow and Shock Waves (New York: Interscience).

Cox, A. N. and Stewart, J. N. 1965, Ap. J. Suppl. 9, 22.

_____ and Eilers, D. D. 1965, Ap. J. Suppl. 9, 1.

Cox, J. P. 1955, Ap. J., 122, 286.

_____. 1963, Ap. J., 138, 487.

_____ et al 1966, Ap. J., 144, 1038.

Eddington, A. S. 1930, Internal Constitution of the Stars (Cambridge: The University Press; Reprinted Dover 1959).

Epstein, I. 1950, Ap. J., 112, 6.

Hastings, C. 1955, Approximations for Digital Computers (Princeton: Princeton University Press).

Heller, J. et al ed. 1965, Suppl. Amer. Math. Mon., 72.

List of References, Continued

Henyey, L. G. et al 1959, Ap. J., 129, 628.

Kahn, F. D. 1954, B.A.N., 12, 187.

King, D. S., Cox, J. P. and Eilers, D. D. 1966, Ap. J., 144, 1069.

Matthews, T. A. and Sandage, A. R. 1963, Ap. J., 138, 30.

Melbourne, W. G. 1959, Ph.D. Thesis, California Institute of Technology.

Mihalas, D. M. 1963, Ph.D. Thesis, California Institute of Technology.

_____. 1965a, Ap. J. Suppl., 9, 321.

_____. 1965b, Ap. J., 141, 564.

Oke, J. B., 1966a, Ap. J., (in press).

_____. 1966b (in preparation).

_____ and Bonsack, S. J. 1960, Ap. J., 132, 417.

_____, Giver, L. P. and Searle, L. 1962, Ap. J., 136, 393.

Preston, G. W. 1964, Ann. Rev. Astr. and Ap., 2, 23.

_____. 1965, Ap. J., 142, 1262.

_____ and Paczynski B., 1965, Ap. J., 140, 181.

_____, Smak, J. and Paczynski, B. 1965, Ap. J. Suppl., 12, 99.

Richtmyer, R. D. 1957, Difference Methods for Initial Value Problems (New York: Interscience).

Roberts, M. and Sandage, A. R. 1955, A. J., 60, 185.

Rosseland, S. 1949, Pulsation Theory of Variable Stars (Oxford: Clarendon Press; reprinted Dover 1964).

List of References, Continued

Sandage, A. R. 1959, Ap. J., 129, 596

Unno, W. 1965, Pub. Astr. Soc. Jap., 17, 205.

Vardya, M. S. 1964, Ap. J. Suppl., 8, 277.

Whitney, C. A. and Skalafuris, A. J. 1963, Ap. J., 138, 200.

Willstrop, R. V. 1960, M.N., 121, 17.

Zhevakin, S. A. 1953, Russ. A. J., 30, 161.